Microstructure evolution and stress corrosion cracking behavior in short-term thermomechanically processed Al-Cu-Li alloys

Vom Promotionsausschuss der
Technischen Universität Hamburg

zur Erlangung des akademischen Grades

Doktor-Ingenieur (Dr.-Ing.)

genehmigte Dissertation

von
Jannik Entringer

aus
Mühltal

2019

Gutachter:	Prof. Dr.-Ing. habil. Norbert Huber
	Prof. Dr. Mikhail Zheludkevich
Vorsitzender des Prüfungsausschusses:	Prof. Dr.-Ing. habil. Bodo Fiedler
Tag der mündlichen Prüfung:	13.08.2019

Abstract

Increasing access to space leaves human footprints in orbits closer to the Earth. Today, space debris poses a major risk for in-service missions and on-ground casualties. Reducing the amount of debris is the only way to preserve key orbits. One strategy to avoid future debris is to maneuver spacecraft after mission into the atmosphere where the structure burns up. This strategy is taken into account at early design stages of modern spacecraft. Therefore, material choices must be made to ensure high structural demisability. Titanium, currently used in propellant tanks, is often a large portion, by mass, of the total structure and does not completely ablate during re-entry.

Aluminum-copper-lithium alloys are being considered as a substitute for titanium in propellant tanks because they deliver comparable specific material properties at a higher demisability rate. Because the technology of aluminum-copper-lithium alloys in space structures is not as mature as that of titanium, new joining methods must be developed. Friction stir welding features the unique characteristic of joining in the solid state; thus, it is especially attractive for hard-to-weld alloys such as aluminum-copper-lithium. The development of space structures requires a fundamental knowledge of the material behavior, both during processing and during the subsequent exposure to the environment. In recent years, aluminum-copper-lithium alloys have rarely been welded by bobbin tool friction stir welding. The underlying microstructure evolution has been described as complex, certain aspects are not fully understood and contradictory results have been reported. Current knowledge on the behavior of welded joints on this specific alloy under stress and exposed to corrosive environments is limited.

Therefore, for the possible use in spacecraft structures, a scientific analysis of the stress corrosion behavior of welded joints is necessary. As part of the present work, two modern aluminum-copper-lithium alloys were successfully joined by semi-stationary bobbin tool friction stir welding. Identical parameters allowed a detailed comparison of the process response. The welding process imposes a short-time, thermomechanical exposure in the base material that leads to severe microstructure modification. Based on the chemical composition of the two alloys, the microstructural evolution is explained, and a precipitation sequence is proposed. Overaged strengthening precipitates and equilibrium phases of several types were identified to form during welding. These modifications led to a reduced mechanical performance of 78 % of the ultimate tensile strength. Stress corrosion analyses were performed on pre-, as- and post-welded samples and were correlated with the modified microstructure. Stress corrosion cracking phenomena were found to result from the short-time, thermomechanical effect induced by the welding process. The mechanism leading to stress corrosion lies in the modified microstructure, where coarse, precipitates accumulate at the grain boundaries. These particles are observed to promote local galvanic reactions, which promote dissolution and the consequent development of a cracking network under stress.

Zusammenfassung

Der stetig wachsende Zugang in den Weltraum hinterlässt menschliche Spuren in erdnahen Umlaufbahnen. Weltraumschrott stellt heute ein erhebliches Risiko für aktive Missionen dar. Die Reduzierung des Weltraumschrotts ist die einzige Möglichkeit den Weltraumzugang nachhaltig zu erhalten. Eine Strategie zur Vermeidung zukünftigen Weltraummülls besteht darin, ausgediente Raumfahrzeuge zum kontrollierten Verglühen in die Atmosphäre zu manövrieren. Diese Strategie wird ab der frühen Entwurfsphase für neue Raumfahrzeuge verfolgt und wird sich auf Materialentscheidungen auswirken. Titan, welches derzeit als Material in Treibstofftanks verwendet wird und einen großen Massenanteil der Gesamtstruktur ausmacht, verglüht beim atmosphärischem Wiedereintritt nur unzureichend.

Aluminium-Kupfer-Lithium Legierungen werden als Ersatz für Titan in Treibstofftanks betrachtet, da sie vergleichbare spezifische Materialeigenschaften bei einer niedrigeren Schmelztemperatur bieten. Da Aluminium-Kupfer-Lithium Legierungen in Weltraumanwendungen weniger ausgereift sind als Titan, müssen neue Fügeverfahren eingesetzt werden. Das Reibrührschweißverfahren zeichnet sich durch seine einzigartige Eigenschaft des Fügens im festen Zustand aus. Daher ist es besonders für schwer zu schweißende Legierungen wie Aluminium-Kupfer-Lithium geeignet. Die Entwicklung von Raumstrukturen erfordert ein grundlegendes Wissen über das Materialverhalten, sowohl während der Verarbeitung als auch während des nachfolgenden Einsatzes. In den letzten Jahren wurden Aluminium-Kupfer-Lithium Legierungen selten mittels Reibrührschweißen geschweißt. Zudem wurde die zugrundeliegende Entwicklung der Mikrostruktur als komplex beschrieben, sodass bestimmte Aspekte nicht vollständig verstanden und widersprüchlich berichtet wurden. Daher ist das Wissen über geschweißte Konstruktionen unter Belastung und in korrosiver Umgebungen begrenzt.

Wenn Aluminium-Kupfer-Lithium Legierungen für den Einsatz in Raumfahrzeugen in Betracht gezogen werden, ist eine grundlegende wissenschaftliche Charakterisierung des Spannungsrisskorrosions-verhaltens erforderlich, die sich aus den durch den Schweißprozess hervorgerufenen Mikrostrukturänderungen ergibt. Im Rahmen der vorliegenden Arbeit wurden zwei moderne Aluminium-Kupfer-Lithium Legierungen mittels eines teilstationären Zweischulter-Reibrührwerkzeuges erfolgreich geschweißt. Der Schweißprozess besteht aus einer kurzzeitigen Hochtemperaturphase, welche zu einer starken Veränderung der Mikrostruktur führt. Anhand der chemischen Zusammensetzungseigenschaften der beiden Legierungen wurde die mikrostrukturelle Entwicklung erläutert. So konnte eine Vergröberung der hauptfestigenden Phasen sowie die Bildung von Gleichgewichtsphasen beobachtet werden, welche zu Festigkeitsverlusten der Schweißnaht führten. Zudem wurde eine Spannungsrisskorrosionsanalyse an geschweißten und ungeschweißten Proben durchgeführt und mit der Mikrostrukturtransformation korreliert. Während das Grundmaterial keine

kritische Korrosion unter Spannung zeigte, konnte in den Schweißproben eine Beeinträchtigung festgestellt werden. Daher resultieren die Spannungsrisskorrosionserscheinungen aus der kurzzeitigen Hochtemperaturphase, die durch das Reibrührschweißen hervorgerufen wurde. Der zur Spannungsrisskorrosion führende Mechanismus beruht auf Auslagerungen grober Gleichgewichtsphasen an den Korngrenzen. Diese fördern lokale, galvanische Reaktionen, welche zur Auflösung und der anschließenden Entwicklung eines Rissnetzwerks unter Belastung führen.

Contents

Symbols and abbreviations

AA	Aluminum alloy
AI	Alternate immersion
Al	Aluminum
Al-Li	Aluminum-Lithium
Al-Cu-Li	Aluminum-Copper-Lithium
AS	Advancing side
BM	Base metal
BT-FSW	Bobbin tool friction stir welding
CCD	Charge-coupled device
CE	Constant extension testing
CL	Constant load testing
CPE	Constant phase element
Cu	Copper
DSC	Differential scanning calorimetry
EDM	Electrical discharge machining
EDS	Energy dispersive X-ray spectroscopy
EIS	Electrochemical impedance spectroscopy
FIB	Focused ion beam
FSW	Friction stir welding
GB	Grain boundary
GBP	Grain boundary precipitation

GP	Guinier-Preston
HAZ	Heat-affected zone
HEXRD	High energy X-ray diffraction
HV	Vickers hardness
IGC	Intergranular corrosion
LEO	Low Earth orbit
Li	Lithium
NA	Natural aging
OCP	Open circuit potential
PFZ	Precipitation-free zone
Pt	Platinum
R_{ox}	Resistance of the oxide layer
RPM	Tool rotational speed [rotations per minute]
R_s	Resistance of the solution
RS	Retreating side
SCC	Stress corrosion cracking
SEM	Scanning electron microscope
SSSS	Supersaturated solid solution
SSuBT-FSW	Semi–stationary shoulder bobbin tool friction stir welding with a stationary upper shoulder
STEM	Scanning transmission electron microscope
SZ	Stirred zone
TEM	Transmission electron microscopy
TMAZ	Thermomechanically affected zone

UTS	Ultimate tensile strength
wt%	Weight percent
YS	Yield strength

1 Introduction

The continuing growth of space activities increases the risk of collision both in orbit and on Earth [1]. In 2018, over 6000 satellites and up to 29000 particles with a critical diameter have been orbiting our planet [2] in the low Earth orbit. The low Earth orbit is the most-used orbit for various space missions such as Earth observation, communication and human spaceflight. In the context of sustainable space use, leading space agencies are investigating key strategies to diminish orbit pollution. Following this approach, hardware design criteria have been set up to ensure the capability of complete ablation during controlled or uncontrolled re-entry at any stage of a mission, including after a mission is completed [3], maintaining an on-ground risk of human casualty under 1:10000 for a single re-entry event [4]. The so-called design for demise approach is implied in the early stages of mission design, challenging the currently used materials and processes and providing an opportunity to employ modern materials and manufacturing solutions [3].

Propellant tanks in long-term missions significantly contribute to the mass and are typically manufactured from high-strength, low-density materials, such as titanium. Titanium melts at temperatures above 1600 °C; therefore, high-mass titanium structures do not ablate during atmospheric re-entry. This lack of ablation has been observed several times, as demonstrated by manmade titanium debris found on Earth repeatedly [5]. Among others, titanium is considered a material to be avoided if possible, especially in high mass portions, such as in propellant tanks.

A promising material to replace titanium in propellant tanks is the latest generation of aluminum-copper-lithium (Al-Cu-Li) alloys. These alloys are known for their high strength and stiffness, and they have demonstrated their serviceability since they are currently used by the aircraft industry [6]. The melting temperature of Al-Cu-Li alloys is approximately 650 °C, which would result in total ablation during atmospheric re-entry, even from larger structures. Al-Cu-Li alloys are therefore under investigation to replace titanium in propellant tanks because of their compatible specific properties. To date, Al-Cu-Li alloys have not been used in the production of propellant tanks for long-term space applications. Considering the current standard propellant tank material Ti6Al4V with a UTS of 1102 MPa, a YS of 999 MPa, and Young's modulus of 110 GPa with a density of 4.43 g/cm^3, a typical Al-Cu-Li alloy in T8 temper state will meet the specific stiffness values but also has a 20 % reduction in specific yield strength (YS), which could be compensated by design. Following an overall estimation in a recent study by Airbus [7], the change from titanium to Al-Cu-Li could result in a total of 10-15 % cost reduction. For the use of Al-Cu-Li, a preliminary tank thickness of 3 mm was estimated for a service pressure of 25 bar with a common safety factor on the YS for proof stress [8]. The Al-Cu-Li alloy AA 2060 has been

considered as a potential alloy to fulfill the requirements and was recommended for further investigation [7].

Apart from the implementation of a new material that meets the qualifications of space industry, maintaining the desired properties during the manufacturing process is also challenging. Joining technologies are closely connected to the material and pose a major challenge in every production plan. Welding of the Ti6Al4V was originally conducted by automated-tungsten-inert-gas and electron-beam techniques; however, these techniques have been less applied to Al-Cu-Li alloys. Welding defects are expected to occur in high-strength aluminum alloys using common fusion techniques [9]. For precipitation-strengthened Al-Cu-Li alloys, fusion welding techniques were not able to produce structurally viable joints [10]; therefore, new methods and procedures are required, e.g., friction-based welding processes. Additionally, new structural materials and joining techniques must provide a high level of resistance to environmental influences, especially to stress corrosion because propellant tanks are permanently under stress (pressure) while in service. Stress corrosion compatibility is important because the tank interior might be under permanent exposure to corrosive liquids; stress corrosion initiations are known to be difficult to detect by standard techniques, having led to failures in the past [11].

Friction stir welding (FSW) has been used to join high-strength aluminum alloys with excellent weld quality [12]. By joining in the solid-state phase, the heat input is kept under the critical temperature which allows the successful joining of aluminum. Additionally, the known welding defects from fusion processes, such as segregation, formation of dendritic structures, hot cracking and porosity formation, can be avoided [9]. Bobbin tool friction stir welding (BT-FSW) is a variant of FSW that produces high strength joints by intermixing plasticized material. The significant advantage of BT-FSW is a second shoulder connected to the probe, which eliminates the need for the backing support required in comparable FSW welds. Because no backing bar is required, the bobbin tool is particularly suitable for closed structures, such as pipes or hollow extrusions. In recent years, a stationary shoulder approach has been developed for use in the BT-FSW process to reduce the total heat input further. While a fully stationary BT-FSW process is challenging in terms of tool material and design, the use of a one-sided stationary shoulder, referred to as a semi-stationary BT-FSW, is a proven concept [13,14].

Most investigations on BT-FSW have focused on aluminum alloys of the 6xxx and 2xxx series. For Al-Cu-Li alloys, Skinner et al. demonstrated the general weldability of AA 2195 in 2003 [15]. In 2010, Schneider et al. [16] investigated the correlation of the bulging, the grain-refinement and the strength of AA 2195 T8 welded using BT-FSW. Recently, Wang et al. [17] welded AA 2198 T851 using BT-FSW. The influence of the process parameters on the mechanical properties has shown high mechanical efficiencies, up to 80 % of the ultimate tensile strength. Shen et al. [18] later revealed the local texture of different weld regions for BT-FSW using the same material. Four subzones were identified, formed vertically in the center of the weld and holding different textural patterns. In 2015, the concept of the

stationary shoulder was adapted to BT-FSW [14], and successfully applied to AA 2198 T851 by Goebel et al. [19], employing the semi-stationary shoulder variant holding the upper shoulder stationary (SSuBT-FSW). Welded coupons of SSuBT-FSW were compared to conventional BT-FSW welds in terms of mechanical properties; illustrating that the stationary variant could prove useful in terms of processibility and the resulting mechanical properties.

Judged by the publication numbers, the bobbin tool process variant has regained scientific interest and industrial popularity in recent years; however, the resistance to stress corrosion cracking (SCC) in friction-welded structures is rarely investigated. Dhondt et al. [20] found intergranular corrosion in friction stir welded AA 2050 T8 stirred zone materials when stressed. Additionally, a general difference between the welding zones was observed for AA 2024 T3 FSW samples by Bousquet et al. [21], who found that the heat affected zone is the most sensitive region with regards to corrosion.

Only a small number of studies exist dealing with friction stir welding of the recently developed Al-Cu-Li alloy AA 2060 [22,23]. The literature lacks studies on the weldability process and the properties of the alloys when subjected to BT-FSW.

The Cu/Li ratio has been shown to play a key role with regard to the microstructure evolution [24], and the microstructure state is the dominant factor regarding the corrosion properties [25]; therefore, understanding of the microstructure evolution during the welding process is fundamental. To explore the precipitation evolution, AA 2196 T8 extrusion material was the second alloy to be analyzed. This alloy possesses a significantly different Cu/Li ratio content in comparison to AA 2060; therefore, a correlation of the chemical composition to the microstructure evolution can be developed. Consequently, systematic SCC studies of friction-welded Al-Cu-Li alloys are lacking, especially at extended exposure times. When Al-Cu-Li is considered as a substitute material joined by BT-FSW in future space structures, a fundamental and extensive knowledge on the process, the resulting microstructure and the behavior when exposed to environmental influences is needed.

In this work, SSuBT-FSW was applied to AA 2060 T8 and AA 2196 T8. Identical welding parameters were achieved to allow a valid comparison of the influence of the Cu/Li ratio on the material behavior during welding. The resulting heterogeneous distribution of mechanical properties was analyzed by tensile testing and microhardness mapping. Employing various techniques, the microstructure evolution following the thermal impact of the welding was determined. It was shown that different Cu/Li ratio contents resulted in a different precipitation sequence. Finally, SCC testing led to a detailed overview of the phenomena when friction-stir-welded samples are exposed to corrosive media under stress. Process affected samples showed a reduced susceptibility to intergranular stress corrosion. The mechanism was found in the microstructure, where coarse phases accumulate at the grain boundaries and promote a micro-galvanic coupling with the matrix.

2 Objectives and structure

2.1 Objectives

The recent demands for advanced materials and technologies for air- and spacecraft structures indicate a need for further developments in both areas, as discussed in Chapter 1. Because today's technology structure is highly cross-linked and interdisciplinary, modifications of processes or materials results in consequent changes in the process chain. Using BT-FSW for joining of modern Al-Cu-Li alloys in space structures raises the need for in-depth analyses regarding the performance of the welded joints. This work contributes with fundamental analyses of the underlining microstructure evolution and an analysis of the resulting joint properties, in particular its corrosion behavior. The objectives are thus as follows:

- Process development and the application of SSuBT-FSW to two Al-Cu-Li alloys featuring different Cu/Li ratios.
- Process analysis with a focus on the characteristics of the SSuBT-FSW process leading to defect-free joints.
- Detailed characterization of microstructure evolution during the welding process.
- Analysis of the general corrosion behavior as well as the stress corrosion behavior of both welded alloys.
- Understanding of the correlation of the microstructural changes in the weld region caused by the thermal impact and the SCC properties in Al-Cu-Li alloys.

2.2 Structure

To achieve the objectives, the work is presented using the following structure. In Chapters 1 and 2, the topic, the goal of the work and the methodology are introduced.

In Chapter 3, an overview of the state-of-the-art with regards to the relevant subjects is given. The Al-Cu-Li alloys are presented, bobbin tool friction stir welding is introduced and the relevant SCC phenomena are highlighted. In Subchapter 3.4, the introduced topics are put into perspective of the application purpose and requirements.

In Chapter 4, the materials and experimental methods employed for testing and analyses are briefly described.

In Chapter 5, the semi-stationary bobbin tool friction stir welding process is described. Further, a detailed process analysis is given, where process forces, torque and thermal cycle are discussed to explain the weld condition in all process steps.

In Chapter 6, the microstructures of the two investigated alloys are explored in detail. Beginning with the determination of the base metal state (T8 temper), a number of analysis techniques are employed to discover the pre, as and post-weld conditions and the microstructure evolution during the actual welding process. The influence of the different Cu/Li ratios in the alloys on the microstructure evolution is discussed. The effects of both the modified microstructure and the different Cu/Li ratios on the mechanical performance are analyzed in detail.

In Chapter 7, the influences of the welding process regarding the corrosion behavior of the welds are shown. The base metal and the individual welding zones are investigated with respect to the general corrosion behavior before stress corrosion is taken into account. SCC phenomena was then analyzed for the individual microstructure modified welding zones and the complete welded structure to evaluate the effect of the process on the stress corrosion behavior based on the knowledge presented in Chapter 6.

In Chapter 8, the primary findings of the previous chapters are discussed, with particular focus on the microstructure evolution during the welding thermal impact and the stress corrosion mechanisms in short-timed thermally impacted microstructures.

In Chapter 9, a summary of the primary conclusions from this work is presented. These conclusions are set into perspective regarding possible applications in the aerospace industry.

3 State-of-the-art

In this chapter, a brief overview of the state-of-the-art regarding the topics treated in this work is given. Al–Li alloys are introduced as the materials, friction stir welding as the employed process and SCC as the investigated phenomenon. In the last section of the chapter, a brief overview of the challenges driving the application of friction stir welded aluminum-copper-lithium alloys in spacecraft propellant tanks is presented.

3.1 Aluminum-copper-lithium alloys

The effect of adding lithium to aluminum alloys has been explored for more than 100 years. While the first lithium-containing alloy was patented in 1945 by LeBaron [26], significant contributions have been made by Hardy and Silcock from approximately 1954 [27], leading to a first scientific understanding of this new alloying system. Lithium was especially attractive because it increases the strength-to-weight ratio, while reducing the density. As lithium is the lightest metallic element, every weight percent contribution increase with respect to the aluminum drops the density of the alloy approximately 3 %, still it was found to raise the Young's modulus approximately 6 % [28]. Although high levels of precipitation-based strengthening were achieved, the first generations of alloys suffered several drawbacks, such as high anisotropy, insufficient damage tolerance, low thermal stability and high production cost [29]. The newest, third-generation alloy, was introduced in 1990 and improved the microstructure control with the help of multistage heat treatments leading to more balanced properties. The history and the property evolution of Al-Li alloys, has been reviewed in detail in the literature [6,29,30]. Al-Li alloys are of special interest when materials with high specific strength and modulus are required. Consequently, these alloys can be found in many aeronautical and space applications. Prominent representatives are AA 2195, which led to massive weight savings on the external tank of the space shuttle [31], AA 2050, which was used in the modern Airbus fleet [32], and AA 2198, which was used in the manufacturing of the first stage of the Falcon 9 rockets [33].

Many research studies have shown that, for Al-Cu-Li alloys, the Cu/Li ratio is a key parameter with respect to their properties and therefore often the focus of research. The development throughout the Al-Cu-Li generations led to a consequent reduction of the Li content, holding it under 2 wt% for most of the third-generation alloys. The development of the Cu/Li content is shown in Figure 3-1 for several third-generation alloys. The alloy composition development shows that either high or low ratios are preferred. As the precipitation sequence features aspects of both binary Al-Cu and Al-Li systems [24], it appears that alloys are designed to take advantage of one of those systems (which, in the case of low Cu/Li contents, is Al-Li and for high Cu/Li contents, is Al-Cu). This was confirmed by two recent studies investigating the role of Cu/Li in Al-Cu-Li [24,34].

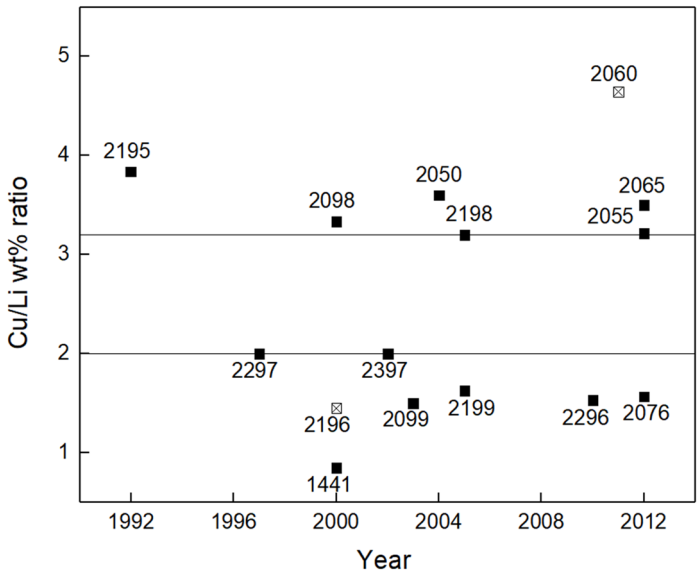

Figure 3-1 Development of the Cu/Li ratio in third-generation Al-Cu-Li alloys. The alloys used in this study are marked with an "x". Reprinted from [35], with permission of Elsevier.

Because the roles of the different alloying elements were identified as the key to the complex microstructure evolution in Al-Cu-Li alloys, several studies have been conducted on the microstructure evolution [36,37]. These studies show that the ternary T1 (Al_2CuLi) is the primary strengthening phase, while binary phases such as δ' (Al_3Li) and θ' (Al_2Cu) contribute less to the strengthening. The precipitation sequence found for Al-Cu-Li alloys depends on the Cu/Li ratio, as shown by Jo and Hirano [38]. Therefore, different precipitation sequences were proposed, depending on the Cu/Li ratio. In more recent studies, several other phases are frequently observed when detailed microstructure analysis is conducted, such as T_2, T_B, S' or Ω [22,39] which are not included in previously proposed precipitation sequences. Furthermore, modern third-generation Al-Cu-Li alloys are becoming more complex by extending the functional microstructure with elements from Al-Cu-Li, Al-Li-Mg, Al-Li-Zr, Al-Cu-Mg or quaternary Al-Cu-Li-Mg-(Ag) systems. Minor elements can have a great influence on the precipitation sequence, as seen for small amounts of Ag and Mg that stimulate the nucleation of a fine, uniform dispersion of the T1 phase [40]. In 2012, Decreus et al. [24] investigated the role of the Cu/Li ratio in Al-Cu-Li-x alloys by analyzing the microstructures of AA 2196 and AA 2198 in different heat treatments. The findings showed a different precipitation sequence with more Cu containing precipitates, such as Cu-rich clusters and θ' for the high Cu/Li alloy, and more Li-rich clusters and δ' for the low Cu/Li alloy. The T1 phase was found in both alloys but showed later incubation in the case of the low Cu/Li ratio alloy. A general precipitation sequence for Al-Cu-Li alloys is still not available in current literature because the role of certain observed phases is unclear.

3.2 Bobbin tool friction stir welding

Friction stir welding (FSW) is based on the principle of joining materials in the solid state. This is achieved by intermixing the joining partners under a thermal input until a solid joint has formed. FSW has been proven effective, primarily for metals where in the first step, the rotating probe is plunged into the material. In the second step, a rotating shoulder is pressed against the substrate, plasticizing the material and generating frictional heat. When sufficient softening has occurred, the welding tool translates into the welding direction leaving an intermixed, solid joint. A typical FSW tool is illustrated in Figure 3-2 a).

FSW was patented by Thomas et al. [41] in the year 1991 and is believed to be a game-changer in metal joining. Initially, developed to facilitate the joining of hard-to-weld materials, such as the high-strength aluminum alloys in the 7xxx and 2xxx series, the technology rapidly demonstrated diversity by joining a number of other materials, including Al, Pb, Mg, Ti, Cu, Zn and steels in similar and dissimilar configurations [42–44]. Comprehensive reviews on FSW have been published by Mishra and Ma [9], Nandan et al. [42], Threadgill et al. [45] and Cam et al. [46] as well as for specific metal groups such as aluminum by Cam et al. [46] or titanium by Russell et al. [47].

The rapid success of FSW, confirmed by a high research interest, is not only related to its multimaterial application but also to other unique benefits. These benefits were divided into three groups by Mishra and Ma [9], i.e., metallurgical, environmental and energy benefits. Compared to other welding techniques, the lower heat input avoids bulk melting, hot cracking and similar defects. Distortion and residual stresses generated by constrained thermal expansion are reduced [48], while good stability and reproducibility is maintained [49]. Superior welding efficiencies were achieved because the short and low heat input limits the impact on a sensible microstructure, which is known from high-strength aluminum alloys. The environmental benefits are related to the absence of evaporation. Additionally, shielding gases or surface pretreatment are not required. The energy consumption is minor compared to comparable fusion-welding techniques. A high energy efficiency of up to 97 % and environmental friendliness are the reasons that FSW is considered to be a green technology [9].

Bobbin tool friction stir welding (BT-FSW) is a variant of FSW that was described in the original patent by Thomas et al. [41], as shown in Figure 3-2 b). In this study, the lower shoulder replaces the rigid backing bar used in conventional FSW, as shown by comparing Figure 3-2 a) and b). In this application, the lower shoulder works as a moving anvil and the pressure required to consolidate the joint is provided between the shoulders. The primary advantage of this setup is the extended use to hollow structures, such as extrusions, pipes or tanks, because the tool is self-supporting and reduces the total force on the substrate to a minimum. Additionally, typical FSW flaws, such as weld root defects, are avoided by complete penetration by the probe. While the first tools employed a fixed gap between the shoulder or were sometimes constructed from a single piece of material, Ding and Oelgoetz [50] found that

controlling the force between the shoulders could stabilize the process. The overall patent situation is complex as mutual claims exist in several international patents [13].

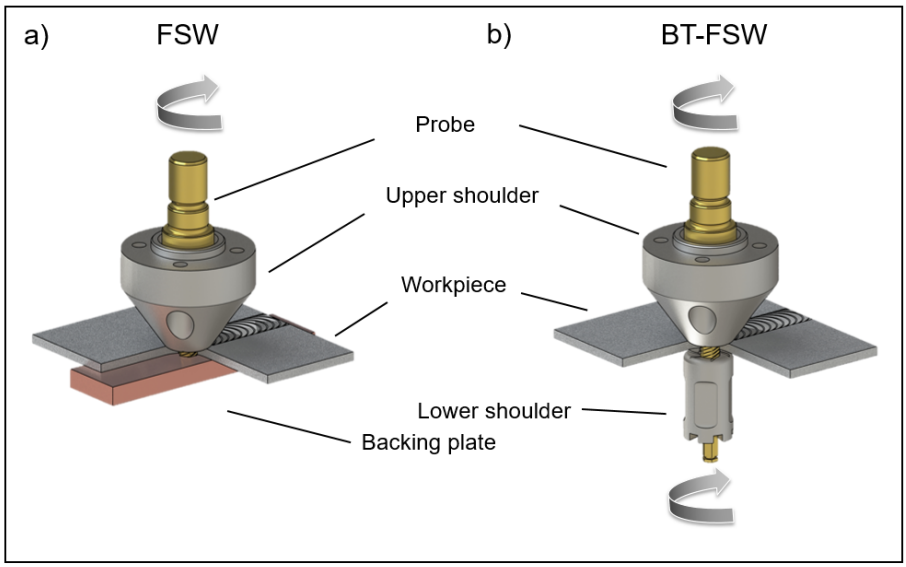

Figure 3-2 Illustration of the FSW tool a) and the BT-FSW tool b).

For the first 20 years after its introduction, only a few studies investigated BT-FSW, and those were primarily with respect to welding feasibility [15,51–54]. Most of the research published after 2010 investigates the process, the microstructure and modeling approaches. Even though BT-FSW has been applied to other materials, such as magnesium [55,56] and steel [57], the vast majority of studies concentrate on wrought aluminum alloys. Among these, the 7xxx series [58,59], the 6xxx series [51,54,60,61] and the 2xxx series [15,16,52,53] are found to be welded most frequently using BT-FSW. Because of the growing interest in high technological, industrial niche sectors, such as the space industry, Al-Cu-Li alloys were likely candidates for BT-FSW welding. In this respect, welding efficiencies have been achieved similar to FSW joints, i.e., between 70-80 % for Al-Cu-Li alloys in T8 temper. AA 2195 was investigated by Skinner et al. [15] and Schneider et. al [16] with respect to the influence of tool form and welding parameters on the resulting mechanical properties. More recently, AA 2198 T851 was studied by Wang et al. [17], who revealed the mechanical properties under changing rotational speed, and by Shen et al. [18] who reported on the texture evolution occurring in the BT-FSW process.

BT-FSW tool design is diverse and up-to-date; no standard tool design has been determined. Various probe and shoulder diameters, probe styles (smooth or featured), and shoulder designs are found in the literature, which complicates a valid comparison between the studies. After the stationary shoulder was

first presented for standard FSW by Widener et al. in 2006 [62], the concept of a stationary shoulder was also adopted to BT-FSW and patented by dos Santos and Hilgert in 2012 [63]. In 2014, Scupin [14] evaluated different stationary tool concepts; the semi-stationary shoulder variant proved most promising and was further employed by the author to AA 2198 T8 [19], AA 2060 T8 and AA 2196 T8 [64].

3.3 Stress corrosion cracking in Al-Cu-Li alloys

Corrosion describes the chemical degradation of materials in a corrosive environment. Although this is common phenomena, observed since man started using materials, corrosion science developed to a well-defined discipline a mere seven decades ago [65]. Studies calculate the corrosion-related (damage) costs for industrialized countries to be 3.5 - 4.5 % of the national gross domestic product and estimate a savings of approximately 35 % by employing appropriate corrosion control [65]. Corrosion always starts on the surface of the affected material, forming a local corrosion cell that consists of an anode connected to a cathode in an electrolyte. The driving force of every chemical reaction is the increase of free energy that is achieved by electron flow in corrosion cells.

While surface corrosion depends on the corroding substrate and the surrounding environment, a special case of corrosion has been found when the substrate is additionally exposed to stress, where a combination of material, environment and stress lead to a special corrosion phenomenon, referred to as SCC. SCC is a critical failure phenomenon and has been studied for many years. A significant amount of work has been carried out to understand the SCC behavior of Al alloys [66–70]. It can be stated that SCC generally correlates to the chemistry and morphology of grain boundary precipitations (GBP) [25]. Among all proposed mechanisms in aluminum alloys, the most-cited are the two following: anodic dissolution initiated cracking and hydrogen induced cracking [66,68,71]. The anodic dissolution mechanism is illustrated in Figure 3-3 a) and describes an intergranular failure mode. Anodic dissolution always proceeds along the grain boundaries or in grain-adjacent regions that dissolve because of their anodic potential with respect to the surrounding microstructure. The hydrogen induced cracking mechanism is illustrated in Figure 3-3 b). Hydrogen atoms can diffuse into the metal lattice and induce cracking when reacting in the gaseous state. Hydrogen reduction is often proposed as the cathodic reaction in aqueous environments, thus increasing the hydrogen density at the surface.

While most hydrogen atoms react and migrate to the gaseous phase, some remain close to the surface and are further absorbed into the lattice from their high partial pressure, which causes intergranular failure. Burleigh [71] related the latter mechanism (hydrogen induced cracking) to the effect on the 7xxx series, while anodic dissolution was predominantly observed in 2xxx series alloys. Kannan et al. [66] later showed that for aluminum alloys, although anodic dissolution is the primary mechanism, hydrogen induced cracking also plays a role. Holroyd et al. [72] then concluded that experimental evidence leads to the assumption that different mechanisms control crack initiation and propagation. While the initiation

is anodic dissolution-dominated, the propagation can be either or a combination of anodic dissolution and hydrogen induced cracking mechanism [73].

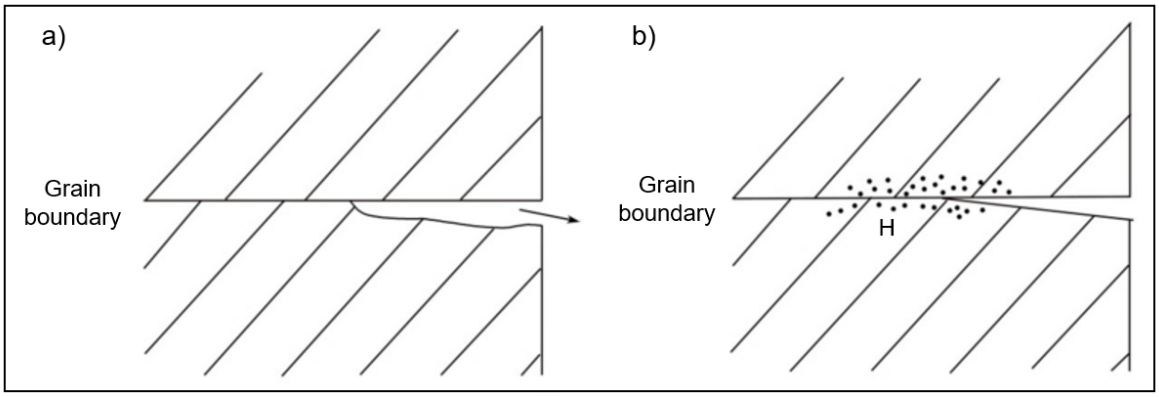

Figure 3-3 SCC mechanisms in Al alloys initiated by anodic dissolution a) and hydrogen induced cracking b).

Similar to high-strength aluminum alloys of the 7xxx and the 2xxx series, Al-Cu-Li alloys undergo intergranular SCC when exposed to chloride environments [66]. Grain boundaries have been reported to hold strengthening precipitates in Al-Cu-Li alloys that tend to dissolve in solution forming depleted regions surrounding the grain boundaries and promoting an intergranular anodic dissolution mechanism [66,74]. Hu and Meletis [75] compared the corrosion and SCC resistance in the Al-Cu alloy AA 2219 and in the Al-Cu-Li alloy AA 2195. The samples were subjected to a slow strain rate and constant load testing, wherein AA 2219 showed a higher susceptibility to environmental cracking. According to the authors, SCC was indicated by hydrogen absorption from localized pits. No information about the heat treatment of the alloys was given. A higher copper level, leading to higher SCC susceptibility, was also found by Moshier et al. [76] when testing different copper levels on the base of Weldalite 049. More recently, Wang et al [77] investigated the behavior of AA 2195 aged at different temperatures between 135-200 °C. Lower susceptibility to intergranular corrosion was found for the samples aged at lower temperatures. The resistance to SCC was evaluated employing low-strain testing. It was concluded that susceptibility is determined by the exposure time rather than the aging temperature. Because of the short exposure times using slow strain rate testing, the exposure might have been too short for SCC initiation. This was confirmed by Holroyd et al. [72], where historical data indicated that SCC initiation is more difficult under constant immersion than under alternate immersion. The testing method, orientation and environmental conditions appear to be of major importance when investigating SCC behavior in Al-Cu-Li alloys. However, SCC initiation and intergranular corrosion is regularly

observed on smooth surfaces of copper containing Al-Cu-Li alloys tested under alternate immersion and in more aggressive environments [77,78].

The available information on SCC behavior of aluminum weldments suggests that the resulting SCC properties depend highly on the transformation that occurs during the welding in different zones of the weld and on the resulting stress, rather than on the environmental exposure itself. While most studies focus on weldable alloys of the 5xxx and 6xxx series, little is published regarding the 2xxx series. In general, the research is divided between fusion-welded structures commonly using filler materials resulting in a chemically modified cast microstructure, and friction-welded structures where only the microstructural state is modified.

With regards to 2xxx series alloys, advanced welding techniques, such as friction, laser or electron-beam welding are preferably employed. Several studies have reported that friction welds of AA 2219 T87 were not more susceptible to SCC than the unwelded material in 3.5 % NaCl solution employing slow strain rate testing [79–81]. Friction-stir-welded samples of AA 2195 T8 were investigated by Hatamleh et al. [82], showing no SCC susceptibility in peened and unpeened (laser shock) conditions using slow strain rate testing. Employing slow strain rate testing in constant immersion, the total exposure time was not sufficient to provoke initiation at rates of 10^{-5} s^{-1} to 10^{-7} s^{-1}, which are typically used. To the author's knowledge, there are no SCC studies of welded Al-Cu-Li alloys employing constant loads coupled with alternate immersion available. The investigation of AA 2050 T8 friction-welded stirred-zone material, conducted by Dhondt et al. [20], indicated a higher susceptibility to intergranular cracking when stressed. For AA 2024 T3 FSW samples, Bousquet et al. [21] showed that the welding zones differ in terms of the suffered corrosion attack; the heat-affected zone is the most sensitive region.

Often related to aqueous environments, it is less-known that SCC is also an insidious failure mechanism in aircraft structures [11,68]. Water condensation, either atmospheric or in inhabited modules, exposure to coastal environments, typically at launch sites, and the presence of aggressive chemical substances, such as cleaning solvents, hydraulic fluids or rocket propellants, can promote SCC on space hardware. Therefore, SCC testing is a critical part of material and process evaluation and essential in most hardware design studies.

3.4 Application of Al-Cu-Li spacecraft propellant tanks

When assessing spacecraft design with regards to the design-for-demise approach, propellant tanks appear regularly as primary targets to be optimized. Because of their high contribution to the total mass and their strict overall requirements (mechanical, chemical and thermal), high melting metals such as stainless steel or titanium are predominantly used. Standard propellant tanks for a one-ton low-Earth orbit mission cause a risk on the ground of up to 20 % [83] and are therefore ideal candidates to be

replaced by a demisable alternative. Several studies are investigating the use of aluminum or composite tanks with no clear conclusions to date [83,84]. Laboratory arc-jet heaters, arc wind-tunnels or laser facilities [83,84] are used to simulate re-entry conditions between 80 km and 55 km above ground, where structures typically experience the highest drag. Additionally, numerical models have been used to assess demisability as a new physical material property. A recent review on performed empirical and numerical testing on carbon-fiber overwrapped metallic liners has shown that composite tanks do not ablate to the required satisfaction, contrary to the initial findings [83]. Aluminum alloys have been tested on the coupon level and show remarkably high demisability in comparison to high-melting metals such as steel or titanium. The lower melting point contributes to a quick and complete melting of the coupon, even though the specific heat capacity is higher, which means that the aluminum requires more energy to heat an equivalent mass to a given temperature.

3.4.1 Spacecraft propellant tanks

Historically, spacecraft propellant tanks have been manufactured from titanium (Ti6Al4V) in solution-treated and annealed, or mill-annealed, conditions [8]. Ti6Al4V performed well in terms of stiffness, strength to density and compatibility to the space propellant media used during operation. Leading propellant tank suppliers have been producing propellant tank series since the early 1980s. These tanks are typically manufactured from Ti6Al4V in a thickness of 0.8 mm to 2.1 mm to withstand the maximum expected operating pressure, which is in the range of 17 to 36 bar [8]. According to NASA's standard [85], these components are usually set with a safety factor of 1.25 with regards to the YS (proof factor) and a safety factor of 1.4 with regards to the ultimate strength (burst factor) when the tank is pressurized in pressure regulated mode. This indicates that the final pressure is achieved in orbit [86]. Because the internal pressure is the primary design criteria, and considering low total mass as another important factor, high specific strength as well as high specific stiffness are key drivers in the material choice. Therefore, in the frame of the design-for-demise approach, titanium has been identified to be replaced wherever possible because of its low demisability performance.

Because of the continuing difficulties in the manufacturing and processing of Al-Cu-Li alloys during the first and second generations, the early generations of Al-Cu-Li alloys were always attractive but never brought to application in space hardware for long-term missions, e.g., in satellites. The third and current generation shows balanced properties at the required levels. Among others, two famous applications of Al-Cu-Li alloys are commonly known. The first is within the space shuttle program, where the Al-Cu-Li alloy 2195 was used in the third generation external tank. The substitution of AA 2219 by AA 2195 led to a massive weight reduction of approximately 7 % [31,87]. This super-lightweight external tank was first launched in 1998 on the STS-91 mission [88]. Second, SpaceX used Al-Cu-Li alloy 2198 for manufacturing the first-stage Falcon 9 launch vehicle [33]. Similar to the external tank program, weight-

and stiffness-driven optimization reasons led to the choice of this alloy over the heritage alloy 2219. Recently, AA 2198 was replaced by AA 2195 on the Falcon 9 launcher [89].

While the first usage has been proven on launchers, the use in long-term missions, e.g., satellites or upper stages, has not yet been targeted. Present research activities are investigating these areas, which requires much higher standards. NASA is considering using AA 2050 as thick plate material for the manufacturing first stage SLS launcher as well as AA 2195 for the thin wall structures in the upper stages. Additionally, the next NASA manned module, ORION, will also employ AA 2050; this alloy has passed the pressure testing of the capsule [90]. For the next European launcher, Ariane 6, scheduled for its maiden flight in 2020, AA 2195 has been selected as a structural material [91].

4 Materials and the experimental procedure

This chapter provides an overview of the hardware, procedure and techniques used in this study.

4.1 Materials

A recent activity, led by ESA, conducted an intense literature research on current Al-Cu-Li alloys and their applicability to spacecraft propellant tanks [7]. A number of available Al-Cu-Li alloys were compared with regard to mechanical, chemical and physical properties as well as in terms of processability and alloy heritage (i.e., strength, stiffness, fracture toughness, formability, welding, corrosion, and availability). Considering all factors, the most promising candidates were identified as AA 2060 and AA 2050, followed by AA 2195 and AA 2099. Because of the current lack of scientific knowledge, AA 2196 were additionally chosen to investigate the influence of the Cu/Li ratio for this study.

Both candidates are modern alloys, introduced in the years 2011 (AA 2060) and 2000 (AA 2196) [28]. The composition was determined by X-ray fluorescence spectroscopy, with additional inductively coupled plasma optical emission spectrometry for the elements lithium and silver, as shown in Table 4-1. Both materials were received at the peak aged T8 temper, which means they were solution heat treated, quenched, cold worked and artificially aged. Because of the novelty of these alloys, no further details of the heat treatment, e.g., the degree of cold working, are known. Sheets of AA 2060 T8 were machined to 300 mm x 100 mm x 3 mm, and extrusions of AA 2196 T8 were machined to 200 mm x 100 mm x 3 mm. Prior to welding, the joining surfaces were flat-milled and cleaned with ethanol. The mechanical properties of the base metal were determined and are shown in Table 4-1.

Table 4-1 Chemical composition and mechanical properties of the base metal

Alloy	Cu/Li ratio	Cu wt%	Li wt%	Zn wt%	Mg wt%	Mn wt%	Ag wt%	Al	UTS MPa	YS MPa	Hardness HV0.2
2060 T8	4.67	4.2	0.9	0.36	0.85	0.32	0.36	bal	516	447	169
2196 T8	1.45	2.9	2.0	0.05	0.38	0.32	0.28	bal	549	513	169

4.2 Process

4.2.1 Experimental procedure

All welds were produced on a five-axis parallel kinematic robotic system (Loxin PKM T805), equipped with a custom-designed weld head, as shown in Figure 4-1 a). The machine was upgraded in 2014 with a customized weld head design. Different variants of the bobbin tool process were considered during the weld head design. In addition to the weld head, the hardware is equipped with an axial actuator to allow normal movement of the lower shoulder during the process. Controlling this axis, the process can be run in constant-force or constant-gap mode. In this study, all welds were produced using the force-controlled process (self-reacting) because this variant proved more stable. The robot was controlled via a predefined path, and the movement of the weld head was programmed accordingly.

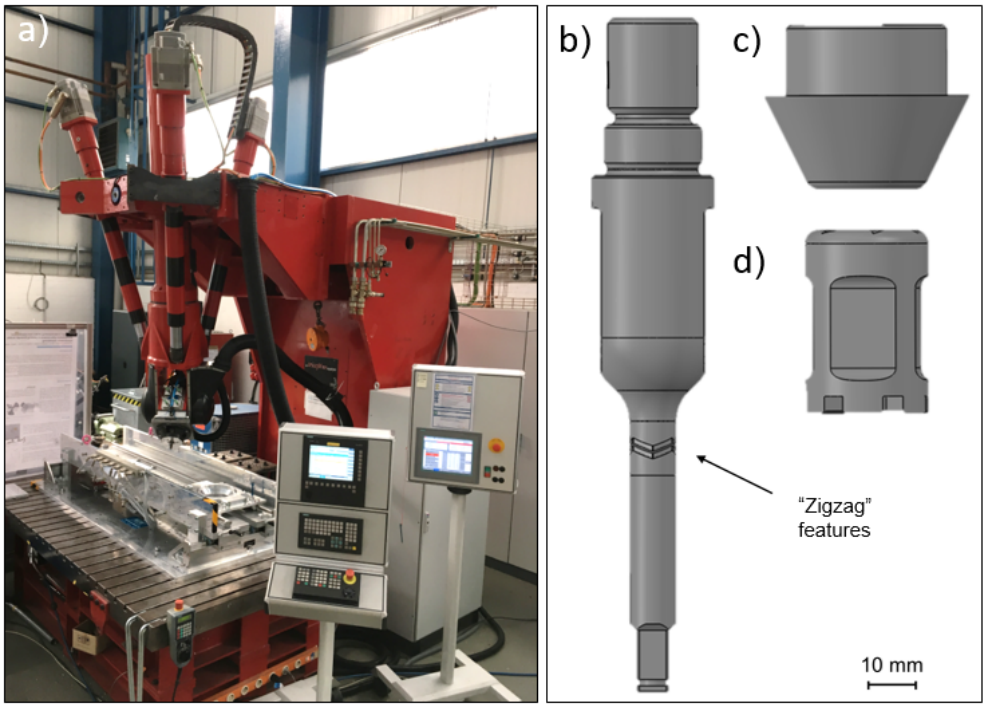

Figure 4-1 Left: PKM T805 robot equipped with a customized weld head. Right: SSuBT-FSW welding tool consisting of a) probe, b) upper shoulder and c) lower shoulder.

The tools for the SSuBT process were the 7-mm featured probe and two 15-mm diameter shoulders, as shown in Figure 4-1 b)-d). The probe shown in Figure 4-1 b) was manufactured from the nickel-cobalt alloy MP159 and included zigzag features. The shoulders (c and d) were made from a molybdenum-vanadium hot work tool steel (X38CrMoV5-1). The lower, rotating shoulder d) had symmetrically scrolled features, whereas the upper, stationary shoulder c) was featureless.

4.2.2 Process parameters

With respect to the process parameters, the welding speed, the spindle rotation and the force between the two tool shoulders contributed the most and were therefore systematically investigated. After working parameters leading to visually sound welds have been determined by trial and error, welding parameters were statistically investigated to find one single parameter set representing the optimum mechanical performance within the given hardware limits.

The parameters were adjusted to 150 RPM at a transverse speed of 150 mm/min. The process was run in a self-reacting mode at 5500 N, allowing the gap width to vary. This parameter set represents a welding condition where defect-free welds can be produced in a reproducible manner for both alloys of interest.

4.2.3 Mechanical and thermal cycle analysis

After the welding process and prior to any testing, the specimens remained at room temperature for two months, allowing the natural aging processes to stabilize. For mechanical testing, samples were machined by electrical discharge machining (EDM) to a modified dogbone shape with a parallel gauge length of 75 mm and a width of 12.5 mm following ASTM E8 [92], as shown in Figure 4-2. The samples were extracted perpendicular to the rolling and welding direction.

The weld thermal cycle was recorded using K-type thermocouples of 0.5 mm diameter, which were placed at mid-thickness in drilled holes and sealed using a silver conductive paste. The positions were 3.5, 6, 9 and 20 mm away from the weld center towards the advancing side (AS), compare Figure 4-2. Additionally, one thermocouple was placed in the center of the weld. This measurement was performed only once, as the thermocouple is destroyed by the rotating probe. Cross-sections were analyzed using a light microscope after process to evaluate the actual thermocouple position with respect to the stirred zone border.

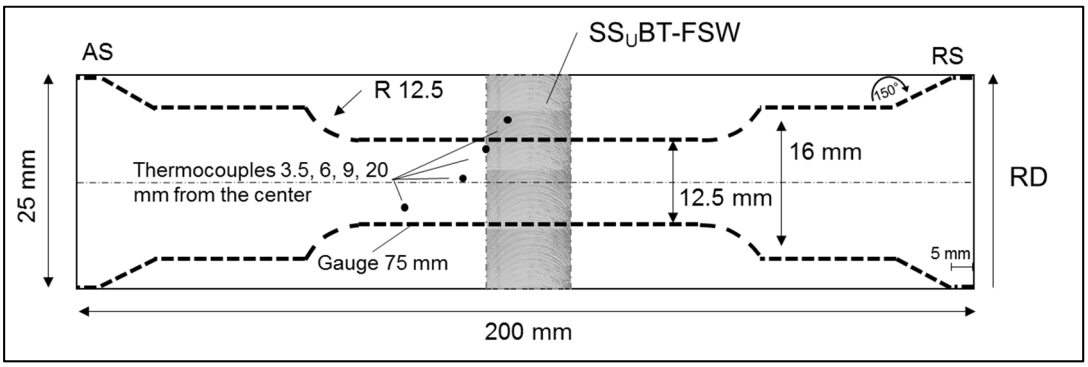

Figure 4-2 Geometry of the specimen for mechanical and corrosion testing, including thermocouple positions.

Tensile tests were carried out on a Zwick & Roell Z100 tensile machine equipped with a 100-kN load cell. The tests were performed at a speed of 1 mm/min, following ISO 6892-1:2009. The hardness measurements were conducted on a Zwick Roell Indentec ZHV 2 hardness tester, in accordance with ISO 6507-1:2005, by applying a weight of 200 grams for 10 s. If not mentioned otherwise, measurements were taken at mid-thickness with an indentation distance of 300 μm.

4.3 Microstructural analysis

All microstructure analyses have been focused on three distinct weld locations, which were determined by the findings in the mechanical characterization. The three locations for sample extraction are the base metal (BM), the heat affected zone (HAZ) and the stirred zone (SZ). The HAZ location was chosen at the position of lowest strength, as shown in Figure 4-3.

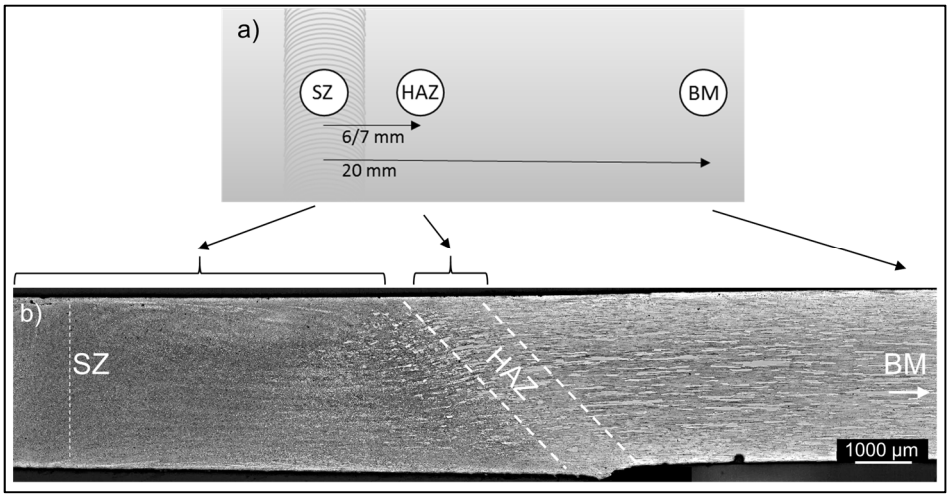

Figure 4-3 Location of sample extraction for microstructure analysis, top view a) and side view b).

4.3.1 Metallographic procedure

For microstructural analysis, samples were sectioned perpendicular to the welding direction. They were prepared employing a standard metallographic specimen preparation procedure, i.e., flat grinding with SiC paper and finish polishing using a diamond suspension. Samples subjected to polarized light microscopy were anodized using a 1 vol % solution of HBF_4, known as BARKER solution, at 22 V for 90 seconds. Chemical etching was used where polarized light was not appropriate, employing Kroll's reagent (2 vol% HF, 6 vol% HNO_3) for 10-20 seconds.

4.3.2 Microscopy

Optical microscopy was conducted on a Leica DM microscope. Further, the scanning electron microscope (SEM) Fei QuantaTM 650 FEG, equipped with an EDS detector, was used for high magnification microscopy. The grain size was measured following ASTM standard E112-13.

4.3.3 Differential Scanning Calorimetry

Differential scanning calorimetry (DSC) measurements were conducted using a Netzsch DSC 200 F3 Maia®. The tested sample shapes and dimensions are given in Figure 4-4. The BM and SZ samples were prepared as 5-mm diameter disks weighing 70 mg each. To extract homogeneous substrate material, the HAZ samples were adjusted to a customized shape and 40 mg. The reference sample was 99.5 % pure aluminum. Pure aluminum crucibles with unsealed lids were used for all specimens. The temperature cycle was set to an isothermal step at 25 °C before heating at a rate of 10 °C/minute (0.167 K/s) from 25 °C to 590 °C in a nitrogen atmosphere. The sample and baseline measurements were recorded sequentially to avoid baseline drift. At least two DSC runs were performed for each measurement. Samples were corrected via baseline subtraction and normalized by the sample mass. Data processing was performed similar to the methodology proposed by Osten et al. [93]. Although the heating and cooling rates recorded from the process are much higher (by a factor of 200) and therefore not to be compared with the heating rates achieved by DSC, this method allows an insight into the microstructure evolution during heating.

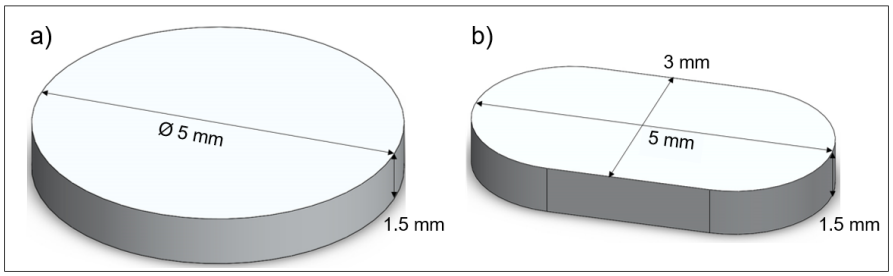

Figure 4-4 a) DSC sample shape for BM and SZ, b) DSC sample shape for HAZ.

4.3.4 X-ray diffraction

High-energy X-ray diffraction (HEXRD) was performed using the beamline at Deutsches Elektronen-Synchrotron (DESY) in Hamburg, Germany. Samples with a thickness of 3.0 mm were measured in transmission with a beam cross-section of 0.175 mm x 0.2 mm. The specimens were exposed to high-energy X-rays with a photon energy of 100 keV, which correlates to a wavelength of 0.124 Å.

Debye-Scherrer diffraction rings were recorded on a two-dimensional Perkin Elmer XRD 1622 detector with an exposure time of 10 seconds taken by the addition of 20 frames. Subsequently, diffractograms were generated by integration and compared to simulated phase diffraction patterns for a qualitative phase analysis.

4.3.5 Transmission electron microscopy

Transmission electron microscopy (TEM) sample preparation was performed in three different locations, as shown in Figure 4-3, which is a top-view orientation, via in situ lift-out using an FEI Helios NanoLab™ 600 DualBeam (FIB/SEM) instrument. The extracted lamella was Pt-welded to an Omniprobe Cu support grid and finally thinned to a thickness less than 100 nm for electron transparency. TEM analysis was performed using a JEOL JEM-2100 LaB6 instrument operating at 200 kV and 102 µA comprising a CCD camera, a STEM detector and an Oxford Instruments Xmax80 EDS detector. To align with preferred crystallographic orientations, the specimens were loaded on a double-tilt sample holder. Images of the loaded sample holder, the actual samples and the resulting fluorescent screen are shown in Figure 4-5.

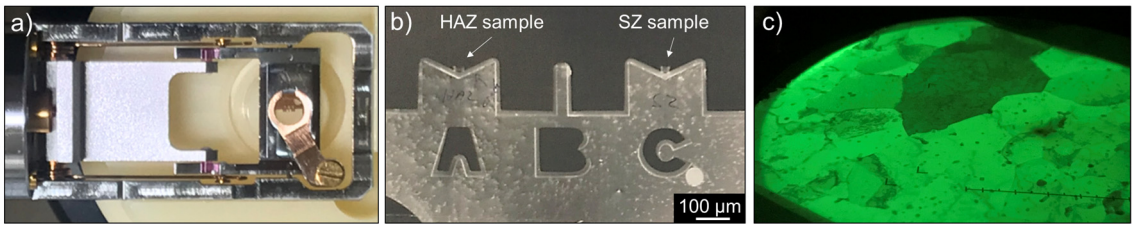

Figure 4-5 TEM sample holder a), specimen overview seen by SEM b) and TEM image on fluorescent screen c).

4.4 Corrosion

The evaluation of the corrosion behavior was conducted through immersion testing, electrochemical testing and SCC testing. While the electrochemical and immersion testing was performed to determine the general corrosion response of the base and welded material, the SCC testing aimed to investigate the special case of the corrosion mechanism occurring under applied stress.

If not stated otherwise, the samples were cut into the desired dimensions by EDM, ground by SiC paper (P1200) to a flat surface finish and rinsed with ethanol followed by deionized water.

4.4.1 Immersion testing

Immersion testing was performed in naturally aerated 0.62 mol/L NaCl solution (corresponding to 3.5 % NaCl solution) at room temperature. A 1-cm² sample area was exposed to intervals of 30, 60 and 120 minutes of immersion and then rinsed by deionized water and dried in an air stream. Subsequently, the exposed surfaces were analyzed using optical and scanning electron microscopes, as described in the previous chapter. Analyses were performed for a multiple of samples extracted at the BM, HAZ and SZ locations indicated in 4.3 for of both alloys.

4.4.2 Dynamic polarization

Dynamic polarization testing was performed in naturally aerated 0.62 mol/L NaCl solution (corresponding to 3.5 % NaCl solution) at room temperature using a GillAC potentiostat by ACM instruments. A conventional three-electrode cell configuration was implemented by exposing 0.5 cm² of the specimen as the working electrode to the electrolyte. Further, an Ag/AgCl electrode (containing saturated KCl solution with a potential of 0.199 V w.r.t. the standard hydrogen electrode) was used, employing a Pt mesh as the auxiliary electrode. The potentiodynamic measurements began with a 60 minutes recording of the open circuit potential (OCP), followed by a potential scan from −200 mV to + 400 mV relative to the OCP, with a scan rate of 0.2 mV/s. From the cathodic branch of the polarization curve, the corrosion rate was determined using the current density at the intersection of the Tafel slope and a vertical line through the corrosion potential. All sample runs were performed thrice.

4.4.3 Electrochemical impedance spectroscopy

Electrochemical impedance spectroscopy at the free corrosion potential was carried out on a GillAC, by ACM instruments, over a frequency range from 10 kHz to 0.05 Hz, in naturally aerated 3.5 % NaCl solution (corresponding to 0.62 mol/L NaCl solution) at room temperature. A conventional three-electrode cell configuration was used, exposing 0.5 cm² of the specimen as the working electrode to the electrolyte. Further, an Ag/AgCl electrode (containing a saturated KCl solution with a potential of 0.199 V w.r.t. the standard hydrogen electrode) was used with a Pt mesh as an auxiliary electrode. The amplitude of the sinusoidal signals was 10 mV. The first measurement began 300 seconds after exposure and was repeated after 1, 4, 27 and 48 hours to follow the degradation of the surface. Further EIS spectra were taken in a range of 10 kHz to 1 Hz to evaluate the behavior over time of the resistance at 1 Hz. Samples were duplicated for each testing parameter set.

4.4.4 Stress corrosion cracking testing

SCC testing was performed following the ASTM G44 standard [94]. In this study, the specimens were exposed to an alternate immersion cycle, which consists of a 10 minutes immersion in 3.5 % NaCl solution (corresponding to 0.62 mol/L NaCl solution) followed by a 50 minutes drying routine at room temperature. The pH value was maintained between 6.4 and 7.2. The solution was renewed every seven days. Total exposure of the specimens was 30 days. Complete welds were tested with the constant load technique. Individual zones were tested using the constant extension technique. Welded samples were tested 4-6 months after welding, when the natural aging processes had stabilized.

Constant load testing

In the first setup shown in Figure 4-6, the samples were stressed by applying a weight load equal to 75 % of the YS before testing; the load was determined beforehand via tensile testing. The testing cycle was applied to the loaded samples and to the unloaded control samples.

This setup was used for welded and base metal samples using the sample geometry described in Figure 4-2. Base metal data points were run in duplicate; welded samples were run in triplicate.

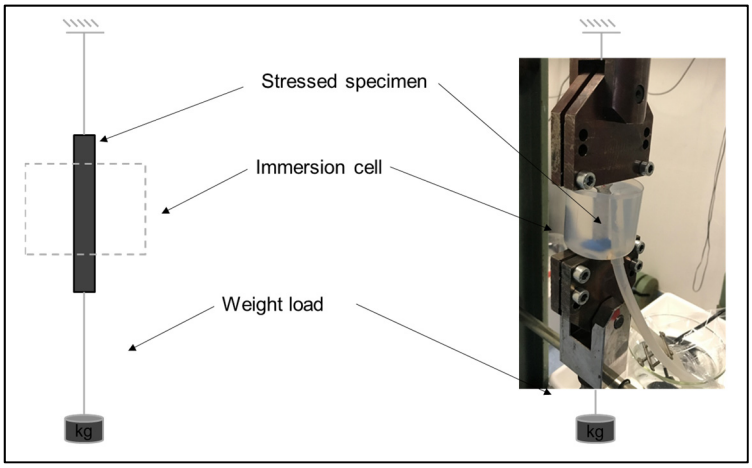

Figure 4-6 Principle of constant loading machine for SCC testing.

Following the 30-day exposure, the surviving samples were subjected to either microscopic investigation or destructive testing, as described in Chapter 4.2.3. Finally, all samples were investigated with respect to the fracture surface, employing SEM analysis.

Constant extension testing

In the second setup, shown in Figure 4-7, the samples were stressed by applying a constant extension, which was calculated using Equation (1) to equal 75 % of the tensile stress. Because this method was used for corrosion testing of the individual zones, the local YS was determined beforehand, via microtensile testing of the locations of interest, as shown in Appendix A. The corrosion samples for the three-point fixture have been cut parallel to the welding direction with dimensions of 70 x 10 mm, where the long side was orientated parallel to the welding direction. The SZ sample was extracted from the center of the weld and the HAZ sample was extracted with a centerline distance of 10 mm from the weld center. The testing cycle was exposed to the loaded samples and the unloaded control samples. All tested zones were tested in replicates of four.

The required deflection was calculated as follows:

$$\sigma = Ety \,/\, 2L \tag{1}$$

where σ = surface stress in MPa, y = deflection in mm, t = thickness in mm, E = Young's modulus in MPa and L = distance of the support span in mm.

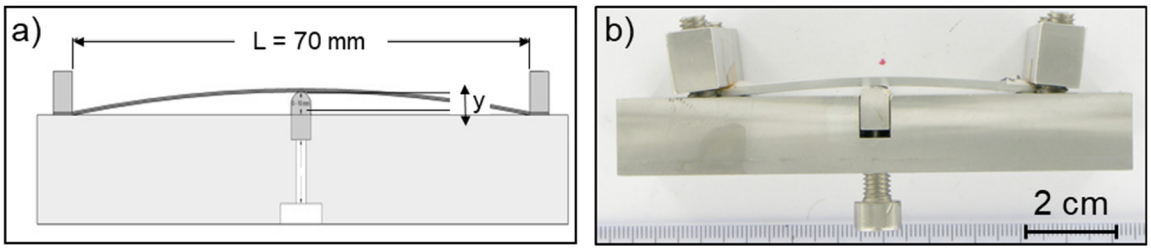

Figure 4-7 Constant extension, three point fixture for SCC testing as drawing a) and image b).

Following the 30-day exposure, surviving samples were subjected to microscopic investigation, including fracture surface analysis conducted on the SEM. Where necessary, corrosion products were removed for visual inspection using 10 % phosphoric acid for 120 seconds.

5 Process

In this chapter, the semi-stationary bobbin tool friction stir welding process is introduced and the working strategy is explained. Further, process data as experienced forces and torque are shown and analyzed with respect to the two alloys under investigation. Finally, the thermal cycle of the welding process is presented and explained for the different alloys. This information is crucial for all subsequent investigations because basic materials modification begins with the process employed. A detailed process understanding is therefore essential.

5.1 Process description

Semi-stationary bobbin tool friction stir welding (SSuBT-FSW) is a stationary variant of the BT-FSW process. While the principle of FSW, i.e., forming a strong joint by the intermixing of plasticized material, is identical, the difference from conventional BT-FSW is that one shoulder remains stationary, causing the heat generation primarily responsibility of the lower shoulder and the probe. This tooling concept was introduced in 2015 by Scupin [14].

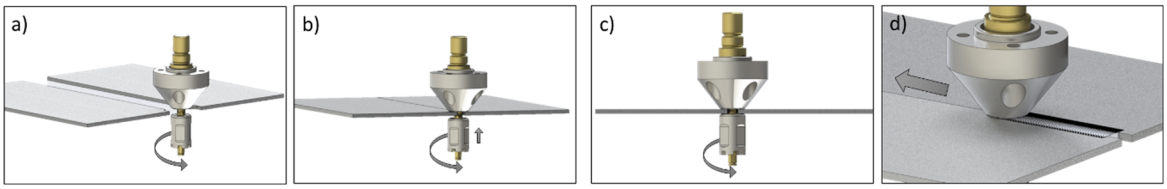

Figure 5-1 Illustration of SSuBT-FSW process: After the rotation has started a), the tool approaches the workpiece where the lower shoulder moves upwards b) until the desired force between the shoulders is reached and c) the tool begins to move forward forming the weld d). Reprinted from [19], with permission of Elsevier.

The SSuBT–FSW process, shown in Figure 5-1 with the tool penetrating the workpieces, joins the two sheets in a butt joint configuration. The lower shoulder and the probe are fixed and in constant rotation, whereas the upper shoulder is decoupled and held. The welding process runs in the force-controlled mode as shown in Figure 5-1 a) - d).

In SSuBT-FSW, the main process parameters are known as the welding speed, the rotational speed and the force between the shoulders, as described in Chapter 3.2. The process runs in the force-controlled mode; therefore, the force between the shoulders was constantly regulated to a preset value by the welding equipment.

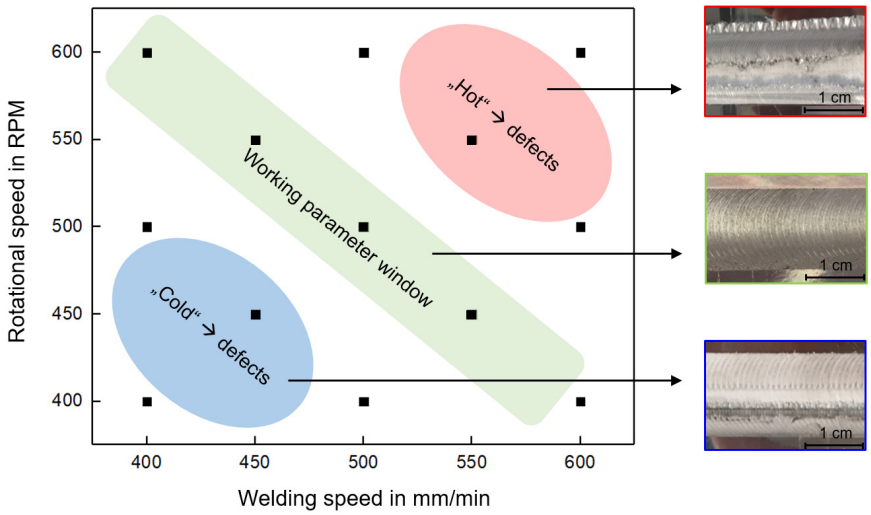

Figure 5-2 Typical parameter window at constant gap force of 5 kN. Examples of welding defects resulting from inappropriate parameters are shown.

The interactions between the three main parameters are complex and only the optimum adjustment will yield a flawless weld [95]. Common difficulties are "hot" conditions, caused by a high rotational speed or a low welding speed and leading to extensive flash formation and hot cracking, and "cold" conditions caused by a low rotational speed or a fast welding speed and leading typically to tool overload or milling of the substrate, as indicated in Figure 5-2. With the semi-stationary variant, the typical material flow, known from BT-FSW, has been modified, leading to a consequent upflow of the material on the AS, as shown in Figure 5-3. This in turn facilitates visual inspection because volume flaws, such as pores or oxide accumulations, will be transported towards the surface. If no such surface defects are observed, the weld can be considered flawless.

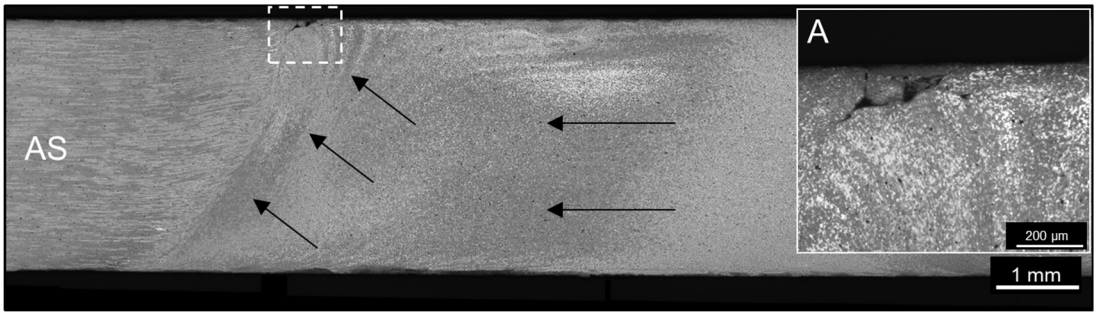

Figure 5-3 Typical material flow towards the stationary shoulder side of an SSuBT-FSW weld. Preferred defect location close to surface is shown in detail A.

In this work, only single parameter sets are treated. Several methods of experimental design, including central-composite design and Box-Behnken design, were employed to optimize the quality criteria, which was the mechanical performance. These statistical methods were employed for the first material (AA 2060) and thereafter transferred to AA 2196. The parameter transfer exhibited difficulties as it became obvious that differences in the chemical composition and temper can have a significant influence on the weld outcome. The final parameters used in this study were chosen to produce an optimized, flawless weld in both alloys. It was possible to find a parameter set resulting in a defect-free result for both alloys, which enabled a valuable comparison between AA 2060 and AA 2196. For the Al-Cu-Li alloys under investigation, SSuBT-FSW parameter sets producing flawless welds were found using a high weld pitch ratio of one rotation per mm.

5.2 Process monitoring

Using process monitoring, it is possible to obtain in- and ex situ feedback of the welding performance, thus leading to an optimized weld strategy. With the equipment presented in Chapter 4.2, force and torque were recorded. Employing an axis transformation, the robot can be programmed to follow a pre-defined path. The welding procedure is typically divided into several sections. These sections can be used for dwelling, ramping or accelerating phases.

In the setup used in this study, a ramping phase was developed to heat the base material and the tool to the process temperature. Additionally, force and torque output data deliver important information regarding the process. For a valid comparison to other thermal processes, the energy input is calculated as follows:

$$E = M \cdot 2\pi \cdot v \tag{2}$$

where E is the energy input, M is the torque and v is the welding speed. Although this equation reflects the total input energy of the tool/material system and gives no indication of the local heat distribution, it has been proved helpful in the comparison between different parameter sets and process variants.

In Figure 5-4 a) and c), the recorded welding parameters over the weld length for AA 2060 T8 and AA 2196 T8 are shown. The overall characteristic of the measured values are similar between both alloys of interest. All forces are measured very close to the preset values, and the curves show that the maximum forces are achieved in the ramping phase before the forces stabilize. The standard deviation of stabilized force and torque between the samples is less than 8 % once the values have stabilized.

The first 30 mm represent the ramping phase to the desired parameters that is used to avoid tool damage when processing the relatively cold material. During the ramping phase, the rotational and the welding

speeds gradually increased, holding the resulting torque and forces under a critical value. Nonetheless, maximum values are reached in the ramping phase, as shown in Figure 5-4.

After the process forces have stabilized for both alloys, the forces in the welding direction settle between 5 kN and 6 kN, while the lateral force is between 1 kN and 2 kN. The torque stabilizes slightly above 50 Nm. Because these values are highly parameter-dependent and characteristic of the semi-stationary BT-FSW variant, they reflect the state using the above-mentioned parameter set. With a input value of 5.5 kN, the force between the shoulders leading to flawless welds is remarkably low compared to the values reported for standard FSW with similar materials [96].

In Figure 5-4 b) and d), the response forces in the welding and lateral directions and the total torque are shown. These parameters give an immediate feedback of the weld quality, e.g., a certain torque is needed to assure full weld consolidation. For the alloys of interest under the investigated parameters, this threshold was found to be just above 40 Nm. This threshold crucially depends on the welding parameters, the workpiece material and the tool dimensions.

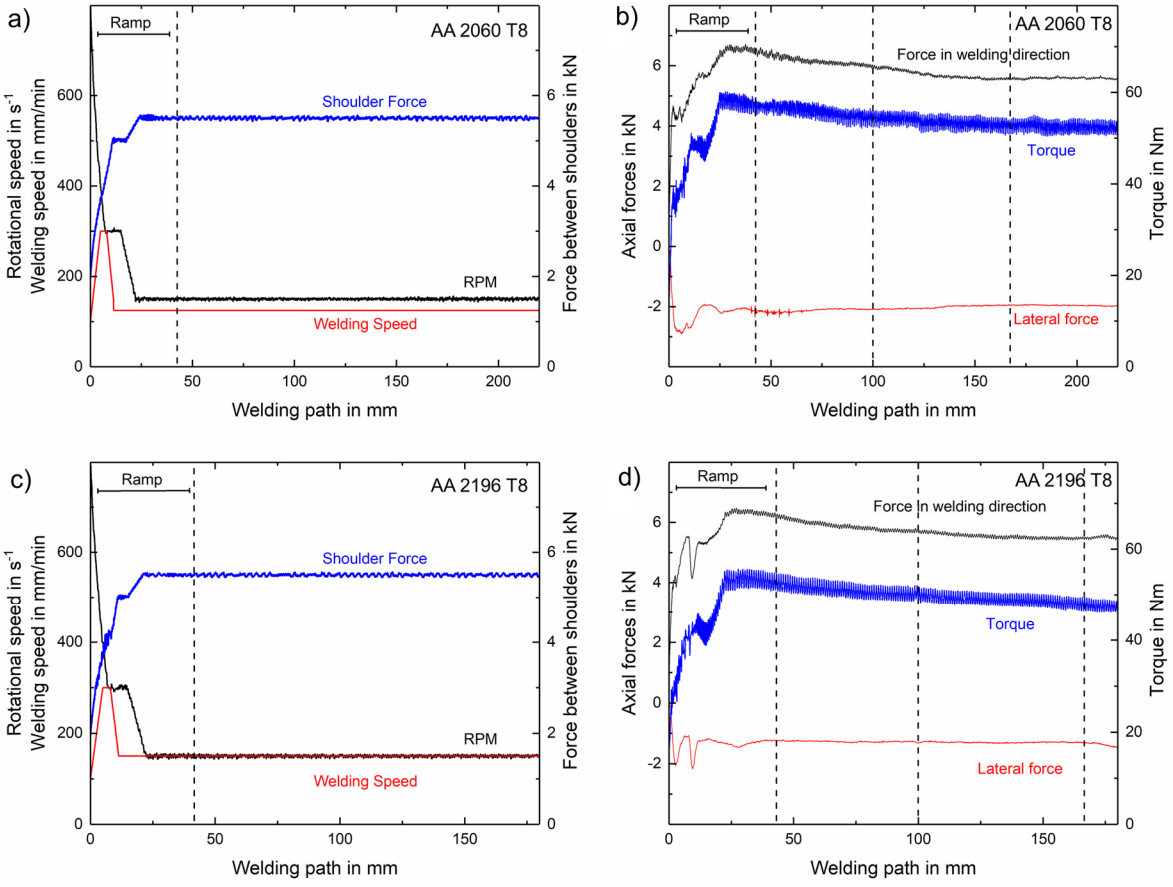

Figure 5-4 Process data recorded during welding for AA 2060 a) and b) and AA 2196 c) and d). Peak load on the tool is experienced during the ramping phase. Reprinted from [64], with permission of Springer.

After the values peak in the ramping phase, the process stabilizes over the length of the weld. The energy input, calculated according to Equation (2), is mainly affected by the torque because the welding speed and rotational speed were constant. Therefore, the energy input is relatively constant following the slope of the torque measurement.

Both alloys, AA 2060 and AA 2196, were welded with identical process parameters but still show different process responses, as shown in Figure 5-5. The measurement was conducted after stabilization of the values. The forces in the welding direction and the torque are approximately 3 % higher for AA 2060, while the forces in the lateral direction are much higher, i.e., 30 %. Although the differences in force in the welding direction and the torque are small, the difference is statistically significant and it was confirmed over all samples. The force in the welding direction represents the resistance against the traversing probe; therefore, this trend was not expected because the base material of AA 2196 features a higher strength in the initial state at room temperature, as shown in Table 4-1. Additional tensile tests under elevated temperatures of both alloys were conducted and indicated controversial behavior. While a higher strength was measured at room temperatures in AA 2196, it seems to have a reduced strength at temperatures of approximately 350 °C compared to AA 2060. This effect might contribute to the observed results. At temperatures above 350 °C, both alloys show similar strengths; detailed information on the testing is given in Appendix B.

It is assumed that the alloys react differently to the experienced thermal cycle and mechanical processing imposed by the process. The high internal pressure between the tool shoulders leads to high shear rates within the SZ. As the shear rate is linked to the evolution of the microstructure in the SZ [97], several researchers attempted to get a precise estimation for the shear rate. For aluminum alloys, this was commonly done by measuring or computing the process temperature and the resulting subgrain size [98], extrapolating the shear strain into the welding zone [97] or other numerical models fitting the ex situ conditions. Because of the inaccessibility of the SZ area during processing, these numbers range between 10 and 100 s^{-1} [99]. Process and tensile measurements at process-similar, elevated temperatures indicate a higher and thermally driven softening for AA 2196 compared to AA 2060. However, additional thermally driven processes can lead to significant changes in the alloy, resulting in different lateral forces. For the precipitation-hardened alloys investigated herein, the thermally influenced microstructure evolution during the process is assumed to be the dominating factor. The analysis presented in Chapter 6 will show the microstructure evolution.

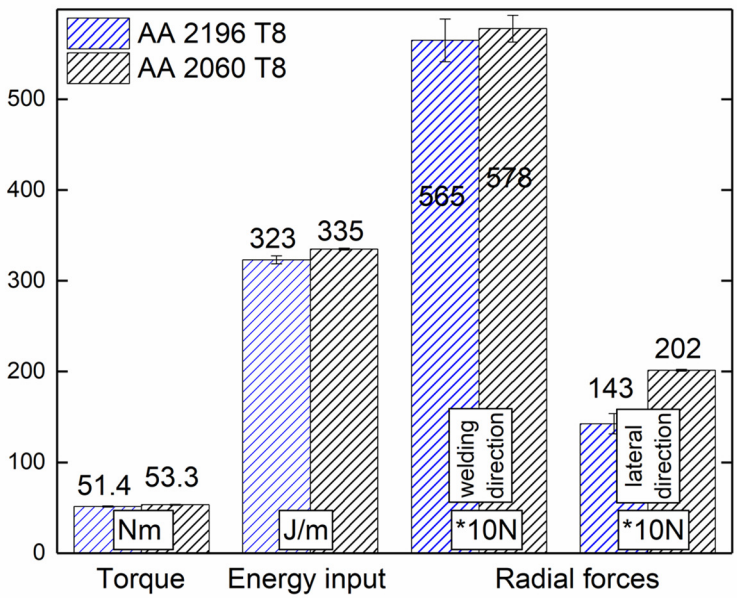

Figure 5-5 Energy input, torque and force output of welds averaged over the sampled length. Reprinted from [64], with permission of Springer.

5.3 Thermal cycle analysis

The temperature development in and around the weld center caused by the energy input is essential to gain information on the temperature-dependent phenomena controlling microstructural and the resultant changes in mechanical properties. Examples shown in Figure 5-6 illustrate two typical thermal cycles for SSuBT-FSW at different distances from the weld center. Position 1 is closer to the weld center and thus experiences higher peak temperatures. The temperatures rise showing high heating rates when the tool approaches and reach their maximum after approximately 10 seconds. After the rotating tool has passed the location of the measurement, the temperature decreases dramatically at a very high cooling rate. Material located closer to the weld center is exposed to higher heating rates and higher peak temperatures than materials located further away. Similarly, locations closer to the weld center experience higher heating and cooling rates.

In general, the thermal cycle shows similarities to the thermal cycles observed with conventional FSW, while compared to fusion-based processes, the peak temperatures are much lower, avoiding the melting temperature.

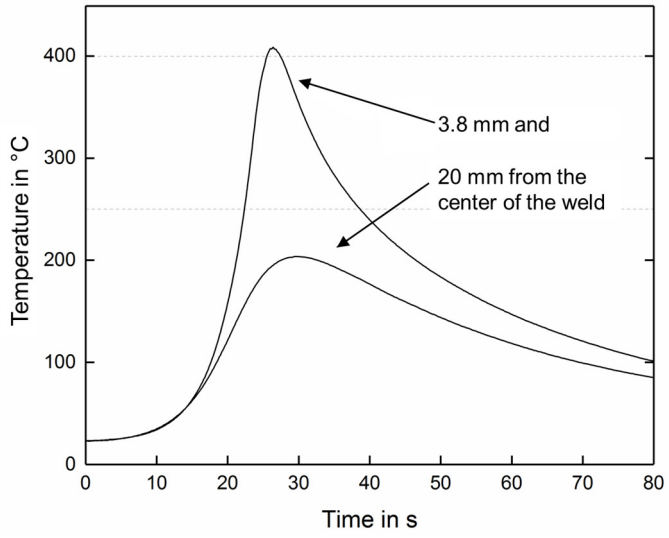

Figure 5-6 Typical thermal cycle of the SSuBT-FSW process at 3.8 and 20 mm from the weld center.

The temperature measurements were recorded for both alloys of interest at mid thickness of the base material and at various distances from the weld center, presented as the distance to the border of the SZ, as described in Chapter 4.2.3. The actual distance to the SZ border was measured, after the process, via metallographic methods. As a result of shear and friction, the SZ experiences the highest temperatures during the process. The heat is generated close to the rotating tool and further dissipated to the surrounding material. Because of the complex mechanical and thermal interactions within the SZ, the exact temperature distribution in the SZ remains difficult to measure. Temperature measurement in the SZ during welding is complicated; therefore, the thermal cycles are measured in close proximity to the SZ and are analyzed with respect to the distance to the SZ border. Chao et al. [24] investigated the temperature fields around the tool and observed that 95 % of the frictional heat is transferred into the workpiece. Therefore, the resulting temperatures of the workpiece are closely related to the heat input. In Figure 5-7 a) and b), the temperature evolution of both materials at distances of 0.3 mm (0.4 mm for AA 2060), 2.5 mm, 5.5 mm and 17 mm outside the SZ are shown.

Additionally, for AA 2060, the temperature was measured in the center of the SZ. Because this method was destructive, measurements were only recorded up to probe contact. A rapid approach to the maximum temperature is seen in all the curves, followed by a slower cooling phase. Material located at further distances is subjected to less temperature variation. Although the general trend is similar for both alloys, the data shows that AA 2196 leads to slightly higher temperatures.

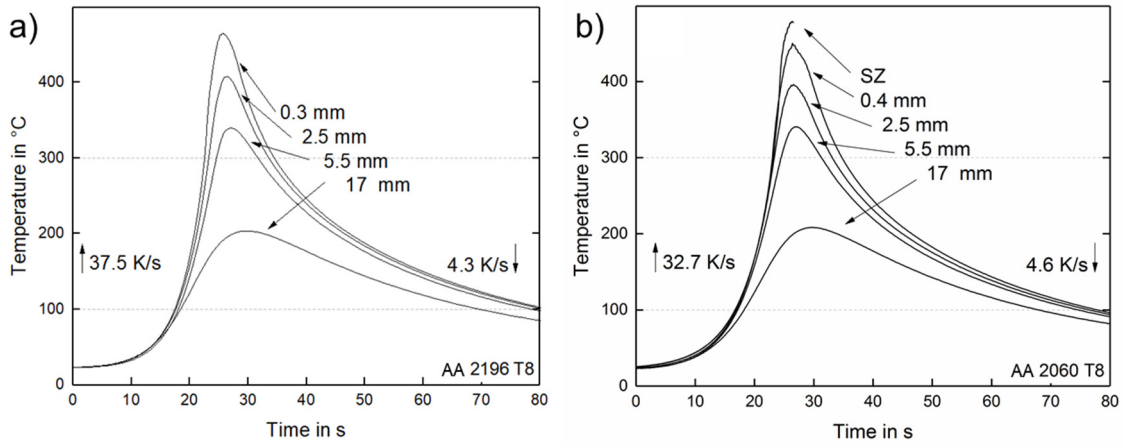

Figure 5-7 Thermal cycle at various positions for AA 2196 a) and AA 2060 b). The temperature course is characterized by a rapid increase (heating) and slower decrease (cooling). Reprinted from [35], with permission of Elsevier.

In Figure 5-8 a), the maximum temperatures are plotted against distance, showing a linear decrease of the peak temperature up to 5 mm from the SZ. At further distances, the temperature measurements develop an exponential behavior in correlation to the heat transfer in welds found by Rosenthal [100]. In the proximity of the SZ, AA 2196 shows slightly higher peak temperatures than AA 2060. The additional data point of the SZ center measurement of AA 2060 allows an estimation of the maximum process temperatures, which were measured as 478 °C. In Figure 5-8 a), the maximum temperatures at various positions of both alloys are compared, and the heating rates are shown in Figure 5-8 b). Heating rates were calculated between 100 °C and 300 °C for the thermocouples at position 0.3 mm and 0.4 mm. AA 2196 experienced rapid heating at a rate of 37.5 K/s; the temperature reaches a maximum of 465 °C at 0.3 mm outside the SZ; and then it cools at a rate of 4.3 K/s. For AA 2060, the heating rate is 32.7 K/s, the maximum temperature was measured as 450 °C at 0.4 mm from the SZ, and the cooling rate is 4.6 K/s. Higher peak temperatures and heating rates were found in AA 2196. The heating rate is approximately 5 K/s higher than in AA 2060, while the measured cooling rates are similar (4.6 K/s vs. 4.3 K/s). Since the boundary conditions, such as the welding parameters, the clamping arrangement and tool properties, are identical for both welds, the above differences depend on the material properties, such as the specific heat capacity and the conductivity. Those quantities are difficult

to determine for alloying systems and their determination would be out of the scope of this work; therefore, pure metal data is used. The conductivity is lowest for lithium, followed by aluminum and copper (71<210<385 W/mK) and the specific capacity, describing the relation between temperature change and energy input, is lowest for copper followed by aluminum and lithium (0.39<0.90<3.31 J/gK) [25]. Following the pure metal properties, alloy AA 2060 will hold high conductivity with a lower capacity while AA 2196 has a low conductivity with a high capacity. A lower conductivity in AA 2196 might contribute to the formation of a heat pool in the SZ, while in AA 2060, more heat will be transferred to the outer areas during that time. In addition, the low heat capacity will result in higher temperatures when exposed to the same amount of energy.

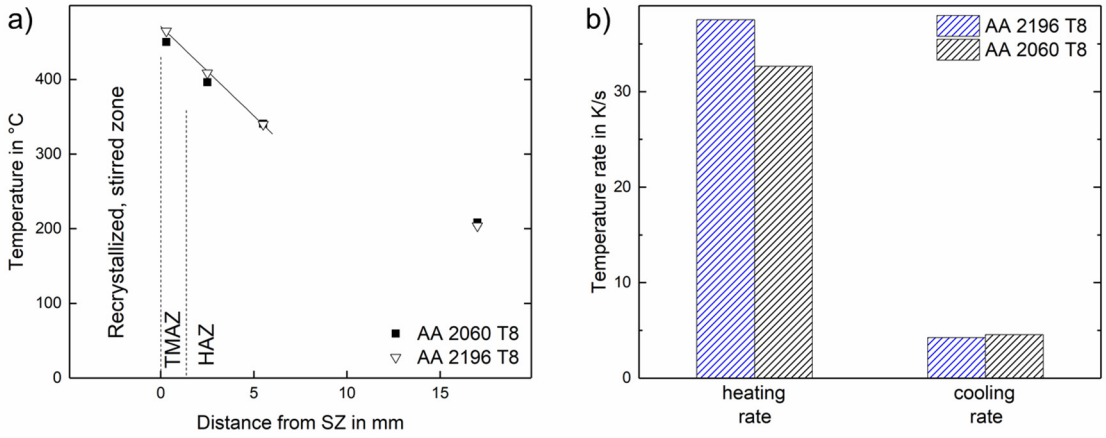

Figure 5-8 Maximum temperatures over distance a) and the heating rates b) for both alloys. Higher temperatures and heating rates were observed for AA 2196 T8. Reprinted from [35], with permission of Elsevier.

The thermal cycle is a key factor in precipitation-hardening aluminum alloys, such as Al-Cu-Li alloys where the dominating strengthening mechanisms, dislocation density and precipitation hardening [101], are highly susceptible to thermal influences. A detailed understanding of the temperature state is essential to correlate the microstructure changes with the mechanical and corrosion properties as done in the following chapters.

6 Microstructure evolution and mechanical properties

In this chapter, the microstructural evolution and mechanical properties for the SSuBT-FSW process of the alloys under investigation are presented. First, the initial state of both alloys will be explained before the actual precipitation evolution during processing will be analyzed. By taking the Cu/Li content ratio of the two alloys into account, the contributing microstructure mechanisms are shown. A detailed discussion on the result of the microstructural changes with regards to the mechanical properties is presented. Additionally, the actual weld performance, achieved for the first time employing SSuBT-FSW in Al-Cu-Li alloys, is determined.

6.1 Microstructure of the base metals

In the as-received condition the BM microstructure consists of pancake-shaped grains 242±55 µm and 222±77 µm in length and 19±2 µm and 27±5 µm in thickness, for AA 2196 T8 and AA 2060 T8, respectively, as shown in Fig 6-1. Constituent particles, which were mechanically broken by the working process, were aligned in the longitudinal direction, as indicated by the arrows in Figure 6-1. No signs of volumetric defects, such as pores, are evident.

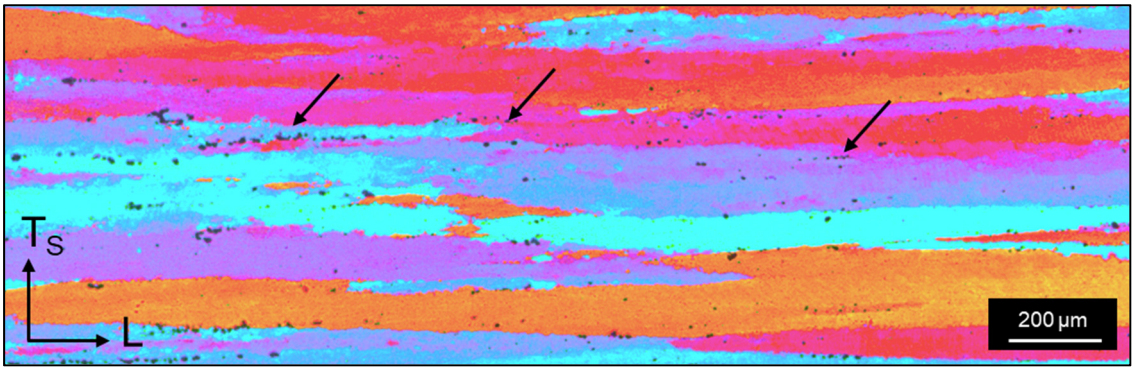

Figure 6-1 Pancake grains typical for BM microstructure demonstrated on AA 2196 T8. Constituent particles are visible at the grain boundaries (arrows).

Al-Cu-Li alloys are a subcategory of 2xxx alloys and precipitation-strengthened alloys, which means that significant strength can be gained by the formation of precipitates from a supersaturated solid solution (SSSS). The precipitation sequence in aluminum-copper-lithium alloys is complex, featuring aspects from both binary Al-Cu and Al-Li systems. The Al-Cu system contributes to the formation of Cu-containing phases, such as Guinier–Preston (GP) zones and θ' (Al_2Cu) precipitates, whereas the Al-Li system promotes the formation of Li-containing phases such as δ' (Al_3Li) precipitates [37,102]. Artificial aging enables the nucleation of ternary precipitates such as the T_1 (Al_2CuLi) precipitate, which is the most

important strengthening precipitate in modern Al-Cu-Li alloys [29]. In 1987, Jo and Hirano reported a strong Cu/Li-ratio dependence of the precipitation sequence [38] and further proposed a Cu/Li-dependent sequence for the Al-Cu-Li system as follows:

For Cu/Li > 4 $$\alpha\ (SSSS) \rightarrow GP\ zones \rightarrow \theta'' \rightarrow \theta'$$ (3)

For Cu/Li = 1-2.5 $$\alpha\ (\mathrm{SSSS}) \rightarrow \mathrm{GP\ zones} + \delta' \rightarrow \theta' + \delta' \rightarrow \delta' + \mathrm{T_1} \rightarrow \mathrm{T_1}$$ (4)

The presented sequences are frequently quoted [10] but do not reflect the state-of-the-art knowledge because other phases have been found, including the S (Al_2CuMg), Ω (Al_2Cu), T_2 (Al_6Li_3Cu) and T_B ($Al_{7.5}LiCu_4$) precipitates [22,24,36,37,103]. The formation of these phases depends on the alloy composition and the processing conditions. Their exact influence on further transformation or resulting properties is not yet fully understood; they are consequently not frequently included in the overall precipitation sequence. Contrary to Equation (3), T1 is frequently reported and confirmed as the main strengthening phase in Al-Cu-Li alloys with high Cu/Li ratios, i.e., greater than 4 [22,104,105]. Additionally, the δ' phase was frequently found in these alloys, especially during the natural aging processes [22,34,104]. Although the transformation mechanism remains unclear, equilibrium phases have been reported [37] and should be included in a precipitation sequence. Therefore, a more precise precipitation sequence is proposed for Al-Cu-Li alloys as follows:

$$\alpha\ (SSSS) \rightarrow GP\ zones + \delta' \rightarrow T_1 + \delta + \theta' \rightarrow T_B + T_2 + \theta$$ (5)

After solution heat treatment, SSSS is formed by rapid cooling, before decomposition into clusters, and GP zone begins. Natural aging describes the decomposition at room temperature, while artificial aging describes the decomposition at elevated temperatures. Precipitates formed at room temperature are GP zones and δ', while θ', T1 and equilibrium phases require higher temperatures, and thus artificial aging, to evolve.

GPI zones are observed as coherent, disc-shaped mono- or bilayers from Al-Cu or Al-Li [106,107], which further evolve to GPII/θ'' or δ' phase. GPII zones, often also referred to as θ'' phase, are regularly spaced arrays of Cu layers [37]. The δ' precipitate is a cubic, superlattice crystal structured, spherical and coherent phase [102]. During further heat treatment, the T1 phase nucleates and the θ' phase evolves while δ' will gradually dissolve into solution. The T1 phase is described as hexagonal, thin shaped platelets that nucleate, depending on other element contributions and preferably on dislocations, loops or existing clusters [34,106], while the θ' is a tetragonal precipitate formed from Al-Cu GPII zones [102]. The T1 phase is the most efficient strengthening phase; however, it competes with the δ' phase for the available lithium [36,108]. Highly dense nucleation of T1 was achieved by increasing the dislocation density [109]. Therefore, these alloys are commonly formed in T8 temper, including a cold working step to introduce

dislocations prior to artificial aging and small additions of Ag and Mg [106]. Both strategies will raise the nucleation spot density and facilitate T1 nucleation.

In Al-Cu-Li alloys, metastable phases from both binary systems, Al-Cu and Al-Li, are found: GP zones, θ' (Al_2Cu), θ'' and δ' (Al_3Li) while the equilibrium phases also include ternary phases: θ (Al_2Cu), δ (AlLi), T_2 and T_B. The main strengthening phases in these alloys are T1, δ' and θ' [29]. While T1 and θ' form at elevated temperatures, δ' forms at room temperature during natural aging. Although T1 is confirmed as the main strengthening precipitate in Al-Cu-Li alloys, the exact contributions of δ' and θ' to the total strength depend on the composition.

Important differences between the two alloys under investigation were found by comparing the microstructures. In Figure 6-2 and 6-3, DSC results from both alloys in solution heat treated (SHT) at 550 °C for one hour and as-received (T8) condition are presented.

6.1.1 AA 2060 T8

The solution heat treated AA 2060 (Figure 6-2 a)) shows an exothermic reaction at 75 °C, which is associated with the formation of Cu-based GP zones, followed by an endothermic, broad peak C at 175 °C, which is related to the dissolution of prior formed phases. Peak D represents the formation of T1 [110], including small θ' contributions at 275 °C [111] and δ formation. At temperatures greater than 300 °C, dissolution of all previously formed phases occurs (peak F).

The dashed line represents the BM condition (T8 temper). In the BM state, the formation of the minor peak B at 130 °C indicates the dissolution of GP zones and fine δ' phases. Peak C at 210 °C represents the dissolution of the δ' phase [112]. The δ' phase observed at 210 °C is believed to form during the artificial aging of the T8 temper [113], which is usually conducted at lower temperatures. At temperatures of approximately 250 °C, the exothermic peak D indicates the formation of the main strengthening precipitates, such as T1 and θ'-like phases [24]. Minor exothermic peaks in the triple-peak region, or region E, superimposed by peak F, are assumed to occur from the formation of equilibrium phases, such as T_2, T_B and θ [112]. The subsequent endothermic dissolution region, starting at 270 °C and ending in peak F, is correlated with the dissolution of the previously formed T1 precipitates, secondary phases and equilibrium phases.

Compared to the solution heat treated material, a lower volume fraction of T1 phases is formed in the BM material because these phases were previously formed during the T8 temper treatment. From these T1 phases in the BM, natural aging phases are observed in higher proportion in the SHT material. In addition, the T8 heat treatment leads to a precipitation sequence that cannot be imitated by the DSC thermal cycle. This is why the formation of equilibrium phases observed in peak F is absent in the SHT sample.

The TEM image of the as-received base metal in Figure 6-2 b) shows the T1 precipitates (arrows in red box) in needle-like shapes, randomly distributed spherical, very small precipitates and a few coarse equilibrium phases in dark contrast. The small precipitates were reported to be θ' (Al_2Cu) precipitates in AA 2060 [22] which could not clearly be indexed in this analysis. Compared to other TEM studies of the same material [22,114], the quantity of coarse equilibrium phases likely to be T_2 or T_B seem to be larger in the present alloy. The often-cited S phase [22,115], [116], which is expected to form in Al-Cu-Li alloys with a Li content below 10 wt% was not observed in the TEM, neither was it identified during DSC analysis. Because of its minor relevance and generally low volume fraction, it is further believed that this precipitate does not influence the main metallurgical reactions.

Therefore, the base metal of AA 2060 mainly consists of strengthening T1 phases with minor θ' contributions and occasional coarse equilibrium phases.

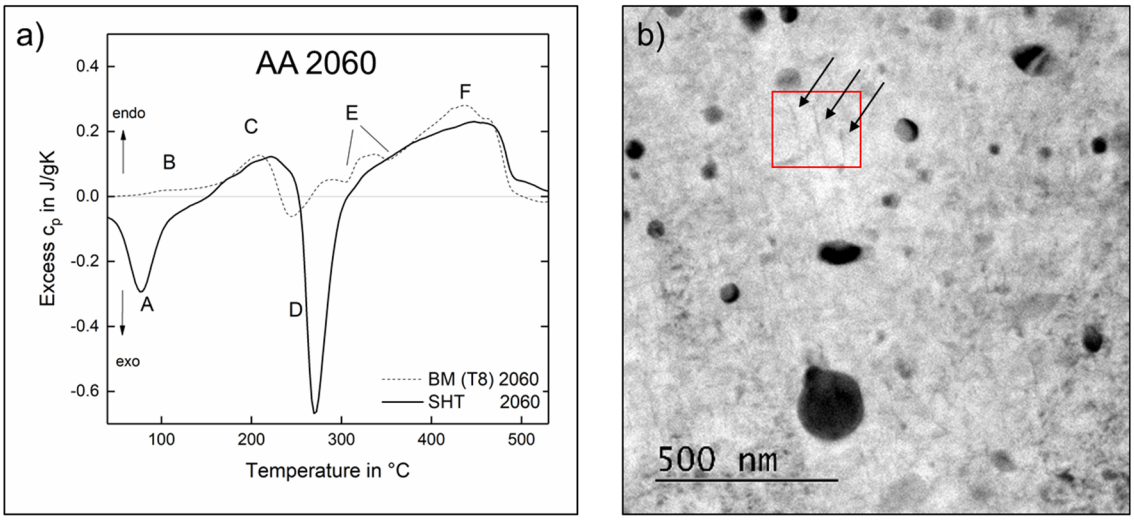

Figure 6-2 DSC thermogram a) of BM and SHT samples and TEM image b) of the AA 2060 base metal indicating T1 needle precipitates in red box.

6.1.2 AA 2196 T8

Details of alloy 2196 are shown in Figure 6-3. The proposed precipitation sequence is assumed to be valid for Al-Cu-Li alloys in general, and thus similar phase formation and dissolution reactions, compared to AA 2060, were observed. The solution heat treated material shows the first peak A at 90 °C, representing the formation of δ' precipitates. These later dissolve in peaks B and C at approximately 200 °C, together with other phases formed at lower temperatures, such as GP zones. Because of the wide temperature range of peak C, further additional reactions, e.g., the formation of Al-Li-based GP zones,

are assumed to occur within these temperatures. The formation of T1 phases is observed at 290 °C in peak D, followed by the final dissolution of all phases represented by peak F at approximately 400 °C.

The base metal, in T8 condition, is represented by the dashed line. Peak A is absent; however, peaks B and C are more distinct, indicating that phases formed at low temperatures, such as δ', have existed before dissolving in peak C because of the T8 temper treatment. As a consequence of the T8 temper and the present T1 precipitates in the microstructure, peak D is smaller. Superimposed by the dissolution of the main precipitates at temperatures above 300 °C, a small exothermic peak E developed, which is related to the formation of equilibrium phases, such as T_2 or T_B. Finally, all phases dissolve at high temperatures, indicated by peak F. The shift of peak F compared to the solution heat treated material towards higher temperatures is associate with a thermodynamically more stable condition resulting from the heat treatment and found in the base metal.

The TEM image in Figure 6-3 b) shows the microstructure of the BM with fine distributed T1 phases (arrow in red box) as well as randomly distributed equilibrium phases. Additionally, small spherical phases are visible which are assumed to be of the δ'/β' structure [103]. These pre-existing δ' particles cause the dissolution of peak C during DSC analyses. The phase δ' was reported to preferably nucleate at existing Zr containing β' particles, which are present to inhibit recrystallization [113]; therefore, they often exist together.

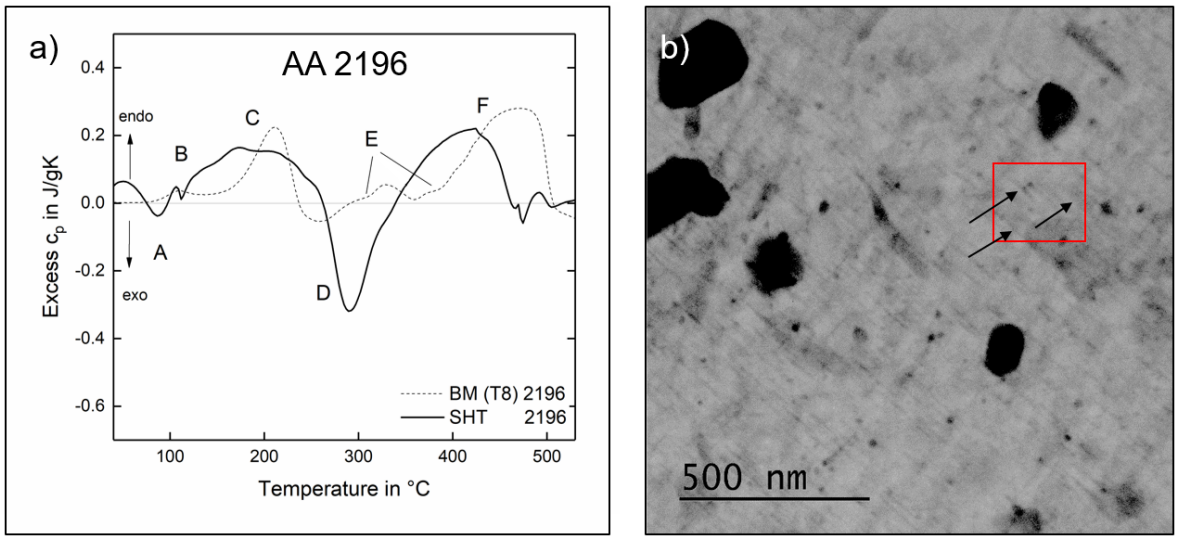

Figure 6-3 DSC thermogram a) of BM and SHT samples and TEM image b) of the AA 2196 base metal indicating T1 needle precipitates in red box.

6.1.3 Comparison of AA 2060 T8 and AA 2196 T8

Comparing both alloys in the as-received state, the data show that peaks B and C are more pronounced for AA 2196, indicating a higher volume fraction of low temperature precipitates present in the T8 temper. Last, the high-temperature dissolution peak F occurs at higher temperatures in AA 2196 compared to AA 2060, which leads to the assumption that T1 precipitates in AA 2196 develop slightly coarser, reaching a more stable condition and thus lowering the Gibbs-Thomson effect, which was also seen for other Al-Cu-Li alloys [24]. The dissolution temperatures are in agreement with the DSC results found for identical phases [10]. Both alloys are in the as-received condition characterized by the presence of the main strengthening precipitate T1, small amounts of spherical precipitates assumed to be δ'/θ' phases, and the occasionally appearing equilibrium phases of the T_2, T_B and θ types.

Diffractograms of HEXRD are shown in Figure 6-4 as a complimentary identification method for the phases observed during the DSC analyses in AA 2060 and AA 2196. Major peaks were indexed at 2θ positions, i.e., at 3.04°, 3.51°, 4.96°, 5.82° and 6.08°, caused by the aluminum matrix. BM samples show traces of T1 phases that are more pronounced in certain orientations from its elliptical shape. The θ' and δ' precipitates are generally difficult to detect because of their small mismatch with the Al-matrix [113]; however, traces of δ' appeared in AA 2196 at 1.7°. A generally higher amount of Cu-containing phases, such as θ in AA 2060, implied that the predecessor phase is present also.

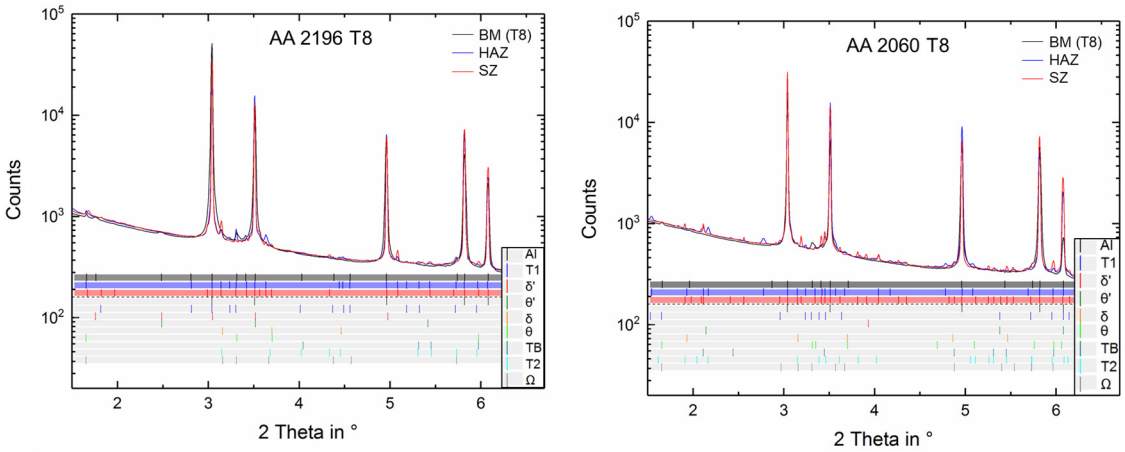

Figure 6-4 HEXRD signal for AA 2060 a) and AA 2196 b) in all welding zones. Simulated diffraction pattern of expected phases are shown for qualitative analysis.

Base material analyses of the two alloys under investigation was performed with DSC, TEM and HEXRD techniques. Both base metals mainly consist of strengthening precipitate phases with minor secondary precipitate contributions and with occasional, coarse equilibrium phases. The main strength contributors in the strengthening phases are T1 precipitates, estimated to contribute more than 90 % of the overall

strength in AA 2195 T8 [115]. The additional strengthening phases found are therefore of minor importance to the overall integrity. Nonetheless, the data showed that the high Cu/Li ratio in AA 2060 promoted the formation of phases found in Al-Cu alloys, while the low Cu/Li ratio in alloy AA 2196 promotes the formation of Al-Li-containing phases. Both alloys exhibit coarse phases, which are indexed as T_B and T_2 phases. This may be due to a rapid transformation into the successor phase or to low instantaneous volume fractions. The difference found in the BM is the behavior at low temperatures, where AA 2196 forms δ' and AA 2060 is strengthened to a lesser extent by forming Al-Cu clusters.

Therefore, the proposed precipitation sequence described by Equation (5) covers both alloys under investigation and provides a more detailed microstructure evolution when looking at phase reactions during heating. Additional reported phases, such as Ω, δ or θ, could not be precisely indexed; however, it is assumed that they do not influence the following mechanical or corrosive properties and thus are not functional microstructure phases.

6.2 Microstructure of the weldments

The microstructure after welding, was very heterogeneously formed across the weld. This is indicated by the macrostructure in Figure 6-5 because it exhibits the typical welding zones, i.e., a centered SZ, which is flanked by the thermomechanically affected zones (TMAZ), and the HAZ. Further from the weld center, the microstructure was not affected by the welding process and the properties returned to the BM properties.

Although using identical weld parameters, the respective weld zones develop different dimensions in the two alloys of interest. The SZ widths at mid thickness were measured as 7.9±0.44 mm for AA 2060 and 8.17±0.03 mm for AA 2196, as shown in Figure 6-5 a) and b).

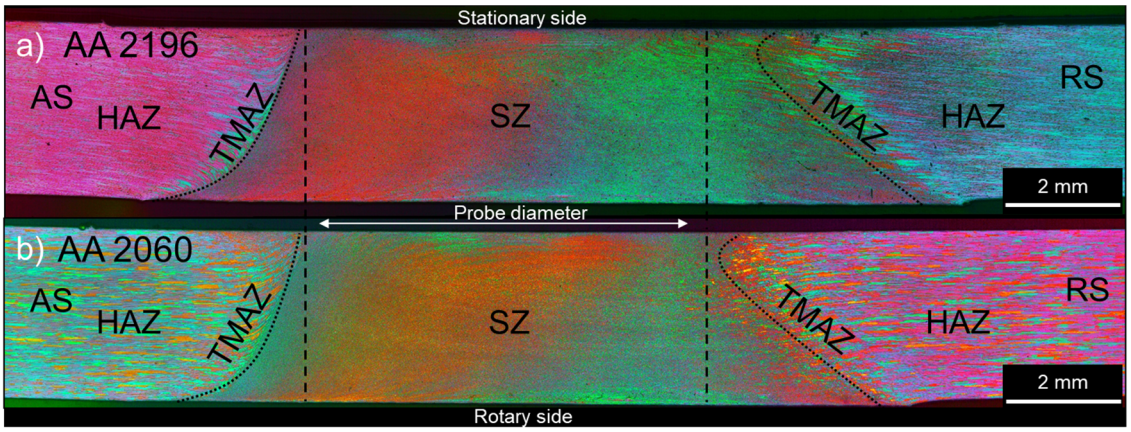

Figure 6-5 Macrostructure of SSuBT-FSW weld for both alloys showing typical welding zones. Alloy 2196 develops a wider SZ using identical process parameters.

The high resistance against the AA 2060 material found in Chapter 5.2 is accompanied by a narrower weld zone development. The properties of the alloys at high temperatures and under high strain rates lead to different slip conditions in the boundary between tool and BM, hence different volumes are transported by the probe. The SZ, consisting of fully recrystallized fine grains, experienced the highest strain rates and peak temperatures. The mid-width of the SZ is extended to the retreating side (RS) of the weld and the widening of the SZ is from the extrusion of hot sheared material around the probe. This was also observed by Colligan [117], who applied the steel ball tracer technique to analyze the material flow in aluminum FSW joints.

The TMAZ is the transition zone from the SZ to the HAZ. It experiences medium strain rates and temperatures, conditions that did not cause recrystallization. The grains are slightly elongated and deformed vertically in both alloys. The interface to the SZ is sharper on the advancing side (AS) and appears fuzzier on the RS. This is a characteristic feature observed in all FSW variants. Cabibbo et al. [118] conducted a microstructural investigation on FSW AA 6056 and found higher strain rates and temperature gradients on the AS caused by the increase in material flow on the RS and high shearing from the probe. The width of the TMAZ varies with the tool dimensions and the parameter settings; however, it was not significantly influenced by the type of alloy.

The HAZ is affected by the thermal cycle and does not experience plastic deformation. The grain size corresponded to the grains of the unaffected base material for both materials, and the pancake-shaped grains originating from the rolling process can still be observed.

While the HAZ did not show significant grain variations, grain size gradients were observed within the SZ for both alloys. Representative micrographs indicating grain size variations for both alloys are shown in Figure 6-6. These results show that the grain size increases from the AS towards the RS, from 6.6±0.47 μm to 7.4±1.0 μm and 5.0±0.22 μm to 8.5±0.81 μm for AA 2196 and AA 2060, respectively. Vertically, the grain size grows in the direction of the rotating shoulder (lower) side, from 5.3±0.4 μm to 7.2±0.9 μm and 6.4±0.7 μm to 9.1±1.2 μm for AA 2196 and AA 2060, respectively. Grain size variations within the SZ have been reported for FSW, indicating that the grain size tends to decrease corresponding to the temperature gradient, i.e., decreasing from top (higher temperature through shoulder influenced zone) to bottom and from AS to RS [9]. Additionally, Esmaily et al. [119] investigated conventional BT-FSW and FSW in extruded AA 6005 profiles and found an increasing grain size from AS to RS in one parameter set of BT-FSW. The subgrain diameter is defined by the strain rate when dynamic recrystallization occurs during high temperature deformation [98,120]. The phenomena of increasing grain size on the RS is thought to be related to the change in shear rate experienced by the material. According to Gerlich et al. [98], the process leads to the smallest grains on the AS, where the highest shear rates occur, and which was confirmed for both alloys under investigation. Vertical

variations can be related to the higher heat generation of the rotating shoulder as well as to the facilitated heat dissipation at the stationary shoulder.

In the SSuBT–FSW welds shown in Figure 6-5, the asymmetric shape of the SZ opens up towards the lower surface. At the lower side, the SZ width equals the shoulder diameter from the shoulder-influenced rotation. Towards the upper surface, the SZ widens much less because of the missing stirring effect in the upper stationary shoulder. The addition of the stationary shoulder reduces the total area of the SZ and the overall width of the affected material from decreased mechanical and thermal influences. This is assumed to have beneficial consequences with respect to the precipitation evolution, which is further discussed in detail in the following section.

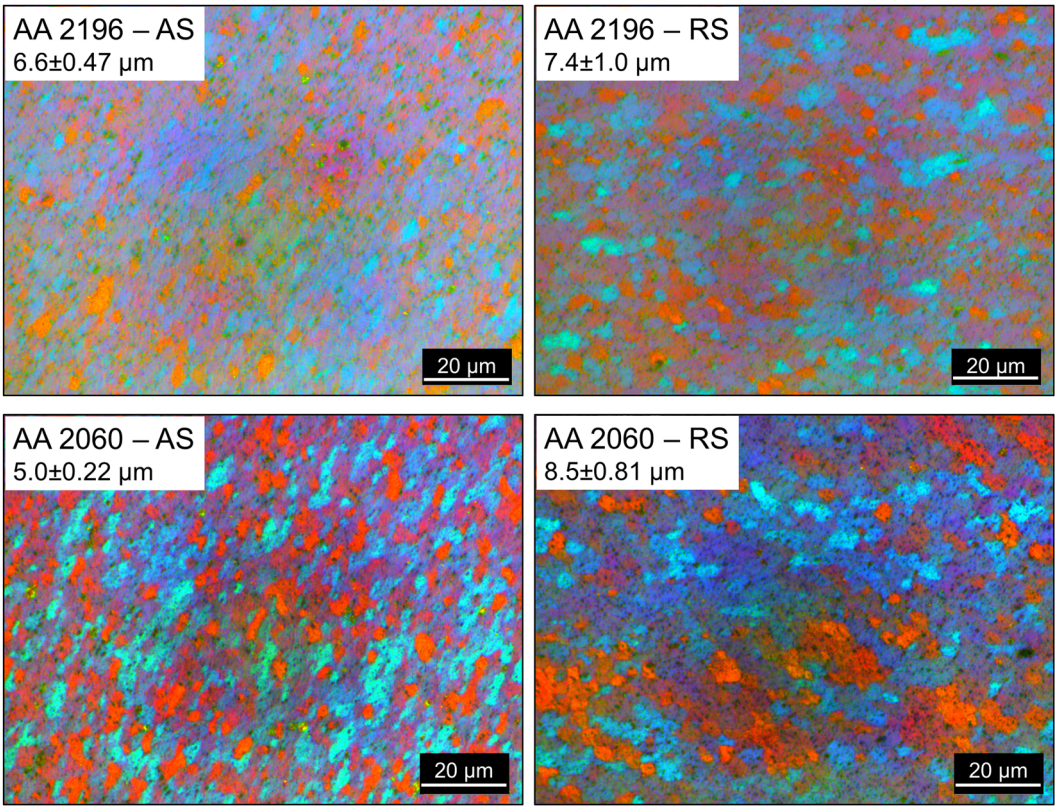

Figure 6-6 Horizontal grain size variations in the SZ for both alloys. Smaller grains are observed in the AS. Reprinted from [64], with permission of Springer.

Because precipitation strengthening is the dominating strengthening factor in Al-Cu-Li alloys, the macrostructure which describes the size, distribution and shapes of the grains does not explain the heterogeneity in the weld. To analyze the resulting weld properties, the microstructure, which gives a detailed look into the precipitation evolution during welding, is discussed in the following paragraphs.

6.2.1 Precipitation state in AA 2060 T8 weld regions

In Figure 6-7, the precipitate transformation of the welding zones in AA 2060 is shown. Because the BM material did not undergo any change, it is used as the reference and presented in dashed lines. SZ samples are shown in red and HAZ samples are in blue. To compensate for the different sample shapes, BM samples of identical shapes were measured and are shown in the respective color because the sample mass and shape can influence the quantitative outcomes of the data. The SZ specimen was exposed to peak temperatures of approximately 480 °C during the welding process, resulting in strong dissolution reactions of the strengthening phases. The SZ sample was tested several weeks after welding and in a stabilized condition, implying that the major natural aging processes have stabilized. In comparison with the BM, AA 2060 shows increases in peaks C and D, which represent the dissolution of δ' (peak C) and the formation of T1 phases (peak D). Peaks in region E related to the formation of equilibrium phases T_2/T_B do not occur, while peak F is similar to the BM sample. The DSC results indicate that the SZ in AA 2060 is characterized by a higher volume fraction of GPII and δ' precipitates, which dissolve in peak C, while only minor T1 precipitate contribution is expected. This is indicated by the high volume fraction formed in peak D, as well as the absence of peak E, confirming that there is no formation of equilibrium phases.

In the HAZ, which is shown in blue in Figure 6-7, a maximum temperature of 396 °C was measured for AA 2060 during welding. With regards to the DSC signal, the HAZ is an intermediate state, exhibiting all of the features of the SZ material, but to a lesser extent in comparison to the BM. The data show a small formation of equilibrium phases represented by peak E, indicating surviving T1 precipitates that can further evolve.

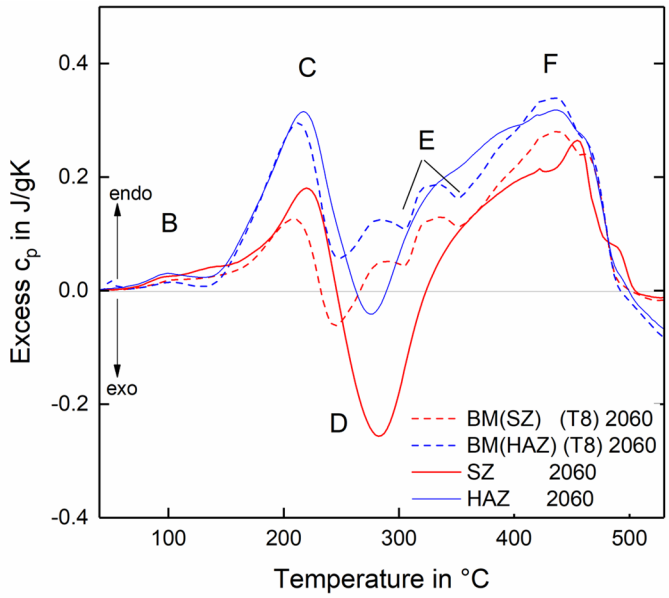

Figure 6-7 DSC signals of the SZ and HAZ compared to BM response for AA 2060.

The HEXRD diffractograms shown in Figure 6-4 confirm the existence of the highest volume fraction of T1 precipitates in the BM and their consequent dissolution during the welding process. Equilibrium phases from Al-Cu (θ) as well as Al-Li (δ) were indexed with higher intensity in the SZ and HAZ samples compared to BM samples. This shows that equilibrium phases are present in the HAZ as well as in the SZ to a lager extent when compared to the BM. Because of their small mismatch with the Al matrix [36], δ' and θ' phases are unlikely to be observed using this technique.

The TEM images in Figure 6-8 provide a detailed view on the precipitates in AA 2060. In the BM, as discussed in Chapter 6.1, the microstructure is primarily characterized by fine distributed T1 needles, with occasional spherical, equilibrium phases. The HAZ includes a high volume fraction of equilibrium phases. Three types of particles shown in Figure 6-8 were classified by shape and EDS analysis, which are presented in detail in Appendix C. Type 1 is rod-like and related to the T_2 phase. Although the T_2 phase has been linked to a spherical shape in some studies [103], a rod-like shape is more likely because this phase evolves from other ternary, rod-like shaped precipitates similar to T1. Type 2 is square-shaped and associated with the θ/Ω phase, a phase that is formed between Al and Cu and therefore likely to be found in overaged, high Cu/Li alloys. Type 3 is a large spherical precipitate, assumed to be T_B. This phase is formed by the transformation of θ' phases by replacing the Al atoms with Li, which occurs with heat exposure [102,121]. The T1 streaks known from the BM material are barely visible while the quantity of small spherical precipitates, possibly δ', is increased.

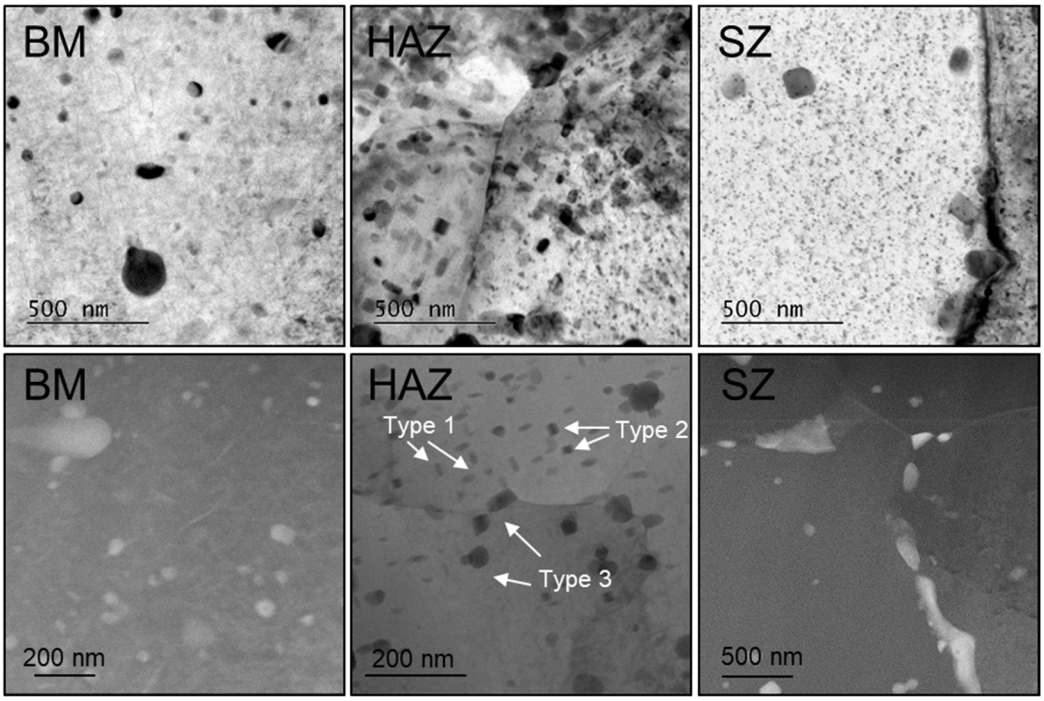

Figure 6-8 Microstructure of AA 2060; TEM (top) and STEM (bottom) images in different welding zones. HAZ and SZ show overaged particles and equilibrium phases which can be classified in three types. Particles are found to preferably accumulate at grain boundaries.

The condition in the SZ sample is clearer. While T1 streaks cannot be observed, the microstructure consists of finely distributed small spherical precipitates and equilibrium phases that tend to accumulate near the grain boundaries. The small precipitates are assumed to have formed after processing and therefore include δ' and GPII structures. The S' precipitate often reported for high Cu/Li alloys [22] was not observed because of the low Mg content; this precipitate is known to form only at considerably high Mg content (above 0.8 wt%) [113].

Important differences between the weld regions of AA 2060 include the following. The SZ consists of small, spherical phases within the grain interior that are related to Al-Cu clusters and minor δ' contributions, while the grain boundaries are pinned with coarse phases of T_2, T_B and θ. The HAZ shows an additional high volume contribution of coarse phases in the grain interior, possibly overaged T1 phases and other equilibrium phases that have not yet segregated to the grain boundaries. Similar to the SZ, the HAZ shows different coarse high-copper phases at the grain boundaries. The BM material remains unchanged (compare TEM images in Figure 6-8).

6.2.2 Precipitation state in the AA 2196 T8 weld regions

The calorimetric thermogram of the precipitation state for AA 2196 analyzed using DSC is presented in Figure 6-9. BM material was used as the reference and is shown in dashed lines. Similar to the samples of AA 2060, the welding zones were tested several weeks after welding in stabilized condition which means that the major natural aging processes have ended. In the SZ material shown in red, peak B, which is related to the dissolution of fine and small GP zones, is much stronger. This reaction, at approximately 125 °C, indicates that a high volume fraction of fine phases of unknown structure were present in the sample. Consequently, peak C is vastly decreased. The decrease of peak C, which indicates the dissolution of δ' at 210 °C, leads to the conclusion that the δ' phases did not reach stable conditions. Instead, fine precipitates formed, inhibiting the known stable δ' condition. This behavior has been shown to be related to the dissolution of clusters formed during natural aging in other Al-Cu-Li studies; however, it has not been further explained [122]. From the samples in this study, these phases form during natural aging and are nearly absent after artificial aging. Therefore, a fine predecessor phase of δ' is suspected. At almost 300 °C, peak D, indicating the formation of T1 precipitates, is more pronounced because more solute elements are present. Similar to AA 2060, peak E is suppressed in the SZ material because of a lack of stable T1 precipitates. The final dissolution of most precipitates occurs at temperatures greater than 450 °C, similar to the BM and shown in peak F.

The HAZ, illustrated by the blue curve in Figure 6-9, shows an intermediate state between the BM and SZ microstructures. Minor peak E is still visible. In this case, the formation of equilibrium phases is still possible, indicating the existence of T1 phases and allowing the transformation referred to as overaging.

Similar to the observations in the AA 2060 material, HEXRD investigations suggest the decrease of T1 in the HAZ and SZ samples.

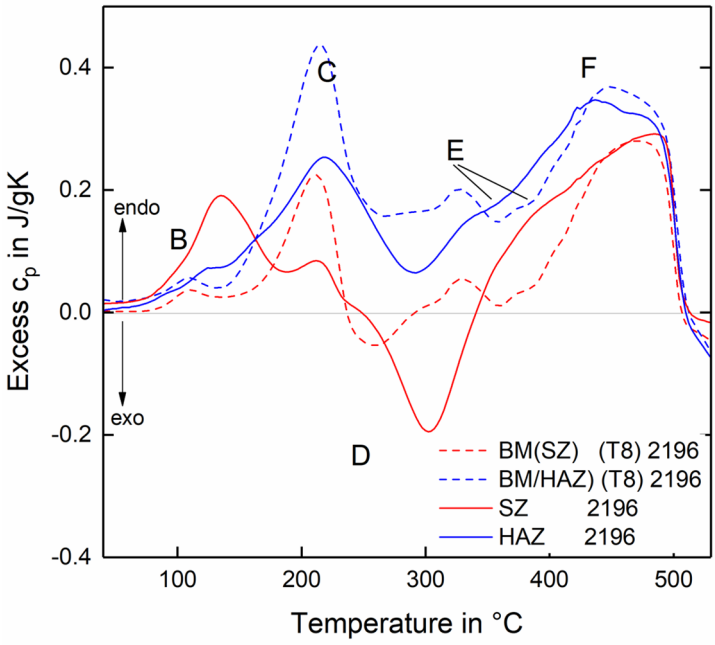

Figure 6-9 DSC signals of the SZ and HAZ compared to BM response for AA 2196.

The HEXRD diffractograms of AA 2196 are shown in Figure 6-4, confirming the dissolution of T1 precipitates in the SZ and the HAZ, similar to the findings for AA 2060. In the HAZ and the SZ, binary equilibrium phases, such as θ and δ, and the ternary T_2 and T_B phases (e.g., at 5.8 °) were indexed.

The TEM images of all the welding zones are presented in Figure 6-10. While T1 streaks are visible in the BM, the HAZ is characterized by coarse phases of types 1 (T_2) and 3 (T_B). The rod-like T_2 phases are still distributed within the matrix, indicating an intermediate, overaged state. The equilibrium phase of the Al and Li δ was reported to nucleate spherically on the T_2 phases [113]. This is confirmed by the observations in the HAZ shown in Figure 6-10. At the grain boundaries of all zones, phases with dark contrast, containing a high fraction of manganese, were indexed. These phases might result from early insoluble Mn-Ag clustering functioning as grain and recrystallization control [102].

Most of the equilibrium phases observed in the HAZ are not present in the SZ. In this study, high-contrast phases with a high fraction of copper stick preferably to the grain boundaries. Within the grain of the SZ sample, fine spherical precipitates are observed that are related to the δ' phases formed during natural aging.

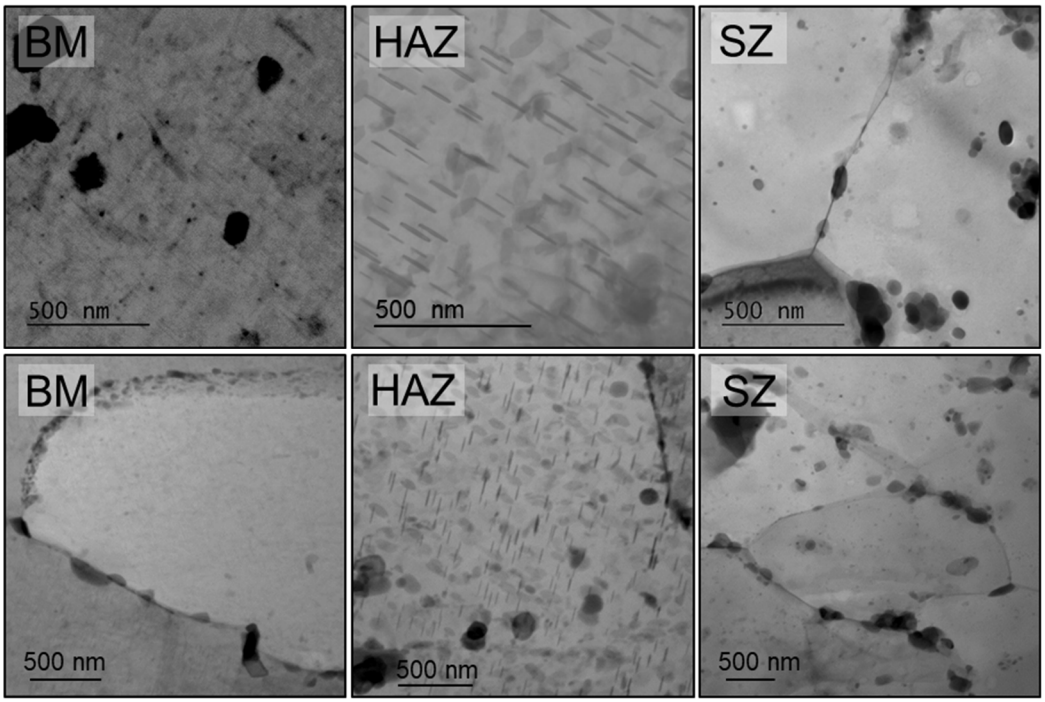

Figure 6-10 Microstructure of AA 2196; TEM (top) and STEM (bottom) images in different welding zones. HAZ and SZ show overaged particles and equilibrium phases which are found to preferably accumulate at grain boundaries.

In the HAZ, AA 2196 shows a microstructural state between the SZ and the BM state described above. Compared to the BM, less phase formation reactions were detected because of the higher volume fraction of overaged precipitates already present. This might be related to a coarsening of the T1 precipitate that was also reported in [39,112]. Peaks in region E are present in BM, not observed in SZ, and very weak in the HAZ. This indicates that T1 precipitates partially survive the welding process in this region; however, a high volume fraction of equilibrium phases have already been formed during the welding process in the HAZ location (overaging).

Observed differences between the weld regions in AA 2196 are the following. In the SZ, small, spherical δ' phases are present within the grain interior that have formed during the natural aging processes after welding. The grain boundaries attract coarse phases of T_2 and T_B. The HAZ shows an additional high volume contribution of coarse phases in the grain interior, most likely overaged T1 phases and other equilibrium phases. Coarse high-copper phases are also present at the grain boundaries in the HAZ. The BM remains unchanged.

6.2.3 Microstructural evolution in the SZ

Extreme conditions during the welding process lead to severe microstructure changes in the material, which are evident in the post-process state, as shown in Chapters 6.2.1 and 6.2.2. High heating rates, exposure to high temperatures, and high deformation rates are dominating influencing factors in friction stir welding processes and especially harmful to precipitation-hardened aluminum alloys.

In Chapter 5.3, the thermal history of the weld was given. In both Al-Cu-Li alloys under investigation, peak temperatures near 500 °C are measured near to center of the weld. These temperatures are above the dissolution temperature of all precipitates known from the time-temperature-precipitation diagram at equilibrium state [123], which is confirmed by the DSC measurements analyzed in the previous section. The SZ experiences a high heating rate of approximately 35 K/s to the maximum temperature followed by a slower cooling rate of 4.5 K/s, for both alloys. Besides the heating rate, the absolute temperature and the holding time above certain temperatures are highly critical for precipitate transformation. The solution temperature of T1 precipitates is reported to be around 450 °C [124] and the actual phase dissolution starts at approximately 320 °C; see Figure 6-2.

As a quantitative measurement, the time at temperatures higher than 400 °C was calculated. The AA 2060 BM was exposed for 5.2 seconds and the AA 2196 for 3.8 seconds. Because of the short exposure time, kinetic considerations hinder a complete dissolution, which is evidenced by the HEXRD analysis in Figure 6-4, where T1 phases are still indexed after welding. Full dissolution was reported in other studies for different thermal cycles and a consequently higher exposure time at a similar peak temperature [105]. Because of the heat input, all phases still transform within the SZ. T1 is mostly dissolved, while small volume fractions evolve towards the more stable equilibrium phases T_B and T_2. Small phases previously formed at low temperature dissolve rapidly at the beginning of the thermal cycle. After reaching the peak temperature, the microstructure is cooled to a supersaturated solid solution. The cooling rates are sufficient to suppress most phase formations, but not high enough to form a perfect solid solution, which is usually achieved by quenching after heat treatment. After the welding process, the material cools at intermediate rates, allowing a small volume fraction of solutes to accumulate and form precipitations, which are found afterwards as the coarse particles or equilibrium phases seen in Figure 6-11. T1 phases found after welding might also have formed during cooling. Besides the thermal impact, the SZ experiences intense mechanical stirring, introducing a high deformation energy. While this deformation does not primarily influence the precipitation transformation, it influences the grain morphology by recrystallization of the SZ [97].

In summary, the SZ experiences the highest temperatures greater than the solution temperatures of all the strengthening precipitates, which leads to severe dissolution during welding. Full dissolution is hindered by kinetic restrictions, which is evidenced by the presence of equilibrium phases confirming

overaging during the heat impact. During the cooling process, reprecipitation of T1 and low-temperature phases, such as δ' and GP zones is assumed.

6.2.4 Microstructural evolution in the HAZ

The HAZ is affected only by the thermal cycle of the welding process. Temperatures varying from 200 °C to 400 °C occur. Heating and cooling rates experienced by the material are slightly lower than observed in the SZ. Because the HAZ is a transition zone experiencing different thermal cycle characteristics, further discussion focuses on the area experiencing the most detrimental changes, which is located 6-7 mm from the center of the weld. This position is defined by the material and process dependent parameter combination and is only valid for the boundary conditions in this study. At this location, the temperature approaches 400 °C. The total exposure to temperatures above 250 °C was approximately 16 seconds for both alloys. Short intervals below 250 °C have been reported to not modify the microstructure significantly [124] because at this temperature, the T1 precipitates are reported to dissolve only partially. Coarsening effects in T1 were observed via small angle X-ray scattering technique only for highly overaged conditions in AA 2196 and AA 2198 [24]. In both alloys, the main strengthening precipitate T1 coarsens and partially dissolves.

This outcome is confirmed by diffraction analysis, which shows a reduced volume fraction of T1 in the HAZ area; compare Figure 6-4. More evolved T1 precipitates transform in one of the ternary equilibrium phases T_2 or T_B, also indexed by HEXRD for the HAZ material. These phases preferentially stick to the grain boundaries, as observed post-process in Figure 6-13.

Summarizing, the HAZ material is exposed to temperatures approaching 400 °C, which leads to intense coarsening transformations, the partial dissolution of T1 precipitates and the formation of ternary equilibrium phases. While the overaged phases are found within the grain interior, coarse copper-containing phases are observed to be preferentially located at the grain boundaries.

When the welding tool has passed, the cooling process starts. Reprecipitation from the slow cooling rates is highly likely. However, a major part of the matrix will remain in a metastable supersaturated solid solution, which enables natural aging after the material has cooled to room temperature. The natural aging behavior is shown in Chapter 6.4.1. The natural aging capability is a proof of the intense dissolution of precipitates, mainly T1 phases, which represent the highest fractions in the as-received temper T8. Natural aging processes are visible far into the HAZ, up to 15 mm from the center of the weld. At this point, maximum temperatures greater than 250 °C were measured, resulting in partial dissolution and a supersaturated solution after welding. The onset of major precipitate dissolution in both alloys is confirmed at these temperatures by DSC analysis; see Figure 6-2 and Figure 6-3. Alloy-specific characteristics will be discussed in the following chapter.

6.3 Cu/Li ratio dependent microstructure evolution during the process

The microstructure state in as-received, as-welded and post-welded conditions were analyzed in the previous chapters. Additionally, the dominating phase transformations during welding were discussed. Both alloys under investigation belong to the third generation Al-Cu-Li alloys; therefore, the precipitation sequence is similar. However, important details have been observed and reported in Chapter 6.1 that led to differences in the final microstructure caused by the welding process. These specific differences are explored for the SZ and the HAZ in this section.

6.3.1 Stirred zone

Microstructure images showing the accumulation of overaged and equilibrium phases at the grain boundaries in the SZ are shown for both alloys in Figure 6-11. Because of the high peak temperature in the SZ, a high volume fraction of precipitates were dissolved in both alloys. Kinetic reasons hindered full dissolution and resulted in intensive overaging and, to a similar extent, the transformation to equilibrium phases. The main difference between the two alloys were the precipitates that form at low temperatures. These phases were responsible for the natural aging strengthening and, from severe dissolution and reprecipitation during post-weld natural aging, mostly pronounced in the SZ. High Cu/Li ratio alloy 2060 is strengthened by GP zones and the clustering of Al and Cu [22], while the low Cu/Li ratio alloy employed the δ' precipitates for the strengthening phase at room temperature. Both phases precipitate as fine disperse spherical phases within the matrix that are nearly unobservable in the TEM analysis.

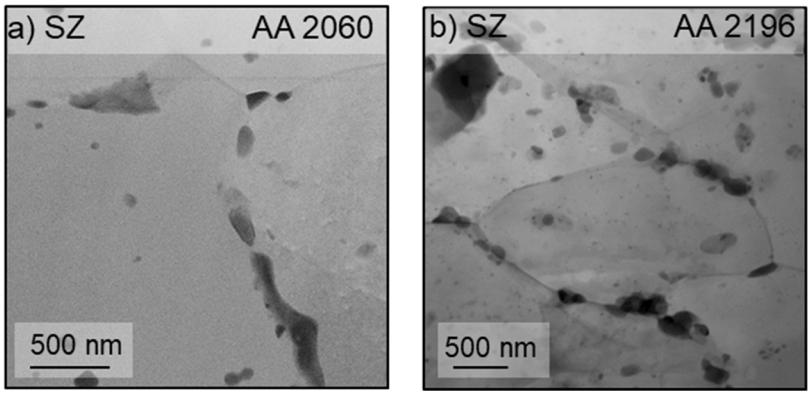

Figure 6-11 Comparison of the SZ microstructure formed during the welding process. Both alloys show accumulation of coarse phases at the GB containing T_2 and T_B equilibrium phases.

Therefore, the DSC analysis shown in Figure 6-12 a) was carried out eight weeks after welding to detect the fine phase transformation. During post-weld natural aging, phases have formed, which in return

dissolve in the DSC measurement giving rise to peaks B, C and D. Peak B represents the dissolution of GP zones, clusters and fine δ' formed during post-weld natural aging and is pronounced for AA 2196. Peak C primarily indicates the dissolution of stable δ' phases. The rise of peak B in AA 2196 represents the higher natural aging response of AA 2196, which has also been reported for the similar Cu/Li ratio alloy AA 2199 [112]. Both alloys show an increased peak D compared to the BM. Because of a higher volume fraction of low-temperature dissolution reactions in peaks B and C (below 210 °C), elements such as Li and Cu are available for the subsequent phase formation reactions observed in peak D, which are phases known to form at elevated temperatures, such as T1 and θ'.

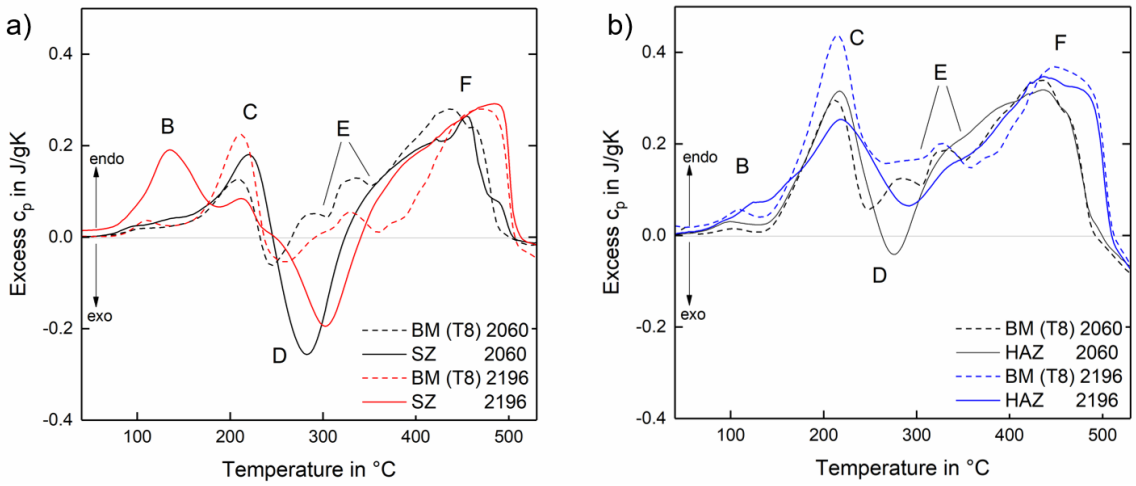

Figure 6-12 DSC signal compared for AA 2060 and AA 2196 in the SZ a) and the HAZ b). AA 2196 shows a higher response to post-weld natural aging while both alloys confirm a high dissolution of strengthening precipitates in peak D. Reprinted from [35], with permission of Elsevier.

6.3.2 Heat affected zone

A comparison of the HAZ analyzed by TEM is shown in Figure 6-13. Both alloys show overaged precipitates and equilibrium phases distributed in the microstructure. The particle density at the grain boundaries is increased. In this microstructure state, the intermediate state between the BM and the SZ is visible, indicating more coarse particles in AA 2196, previously identified as T_2, which resulted from the higher Li solute content in this alloy. Interpreting the DSC signal shown in Figure 6-12 b), the major trends follow the trends in the SZ, while details confirm the intermediate microstructure state. Compared to the BM, peak C was reduced for AA 2196 and slightly increased for AA 2060, indicating alternating volume fractions of the δ' phase from the different Cu/Li ratios. The fine particles present in the BM have evolved during the welding process and were no longer available to form δ' during the natural aging in AA 2196. In AA 2060, the naturally aged phases consisted of Al-Cu clustering and were not much affected by the welding thermal cycle. Peak D decreased for both alloys, which is associated with fewer

phase formation reactions because of the higher volume fraction of overaged precipitates and fewer solute elements. Peaks in region E, which were not observed in the SZ, were very weak in the HAZ. This indicates that T1 precipitates partially survived the welding process in this region; however, a high volume fraction of equilibrium phases were already formed during the welding process in the HAZ (overaging). This finding is also confirmed by the DSC curves of the solution heat treated material, where peak E was also suppressed.

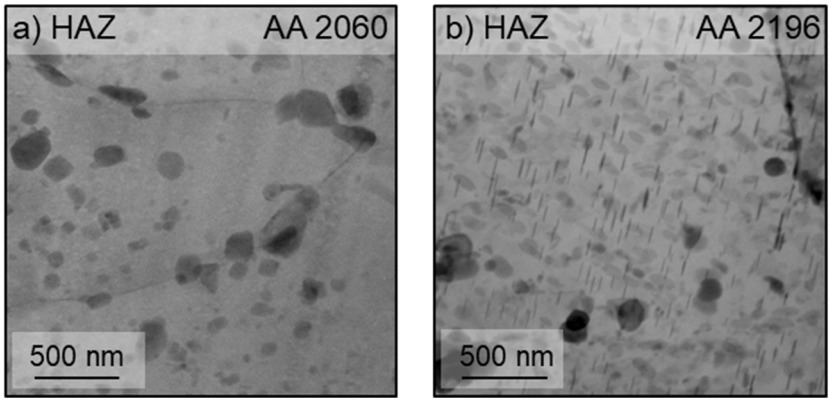

Figure 6-13 Comparison of HAZ structure formed during welding. Both alloys show high density of overaged particles and equilibrium phases which accumulate preferably at the GB.

6.4 Influence of the Cu/Li ratio on mechanical performance

6.4.1 Influence on post-weld natural aging behavior

The microhardness profiles of the welds showed a W-shape, which is a feature typically reported for friction-based welding processes in precipitation-hardened aluminum alloys. In the SZ, a relatively constant hardness plateau was observed. From the beginning of the TMAZ, the hardness values decreased continuously to a minimum in the HAZ. Subsequently, as the distance from the center of the weld increased, the hardness values in the HAZ increased to the initial BM hardness.

Immediately after welding, the alloys showed a hardness of 111 HV and 87 HV in the SZ, while the lowest hardness was measured as 92 HV and 82 HV for AA 2060 and AA 2196, respectively. During post-weld natural aging, the hardness increased in all welding zones, but to varying degrees. The SZ increased by 19 %, the lowest hardness increased by 132 % for AA 2060 after eight weeks (44 % and 27 % for AA 2196).

In Figure 6-14, the hardness across the weld is shown for both alloys. Measurements were performed directly after welding (as-welded), after one week and after eight weeks (post-welded). No further

hardening was detected at longer aging times. The diagrams indicate the age-hardening potential at room temperature. With respect to the natural aging behavior shown in Figure 6-14, the data shows that the precipitates forming at low temperatures can contribute significantly to the total strength of the material. In AA 2196, the hardness increased by 44 %, while AA 2060 was strengthened by 19 % from natural aging, in the center of the weld. AA 2196 exhibited a higher strengthening potential from the precipitation of δ', which was less present in the high Cu/Li ratio alloy 2060. The HAZ was strengthened in both alloys to a similar extent, i.e., 30 % because partial dissolution does not allow the reprecipitation of δ' to the same extent as in the SZ. A minor hardness increase in the HAZ was observed for both alloys, which was related to a reduced formation of phases formed under low temperatures because more elements were bound by overaged particles.

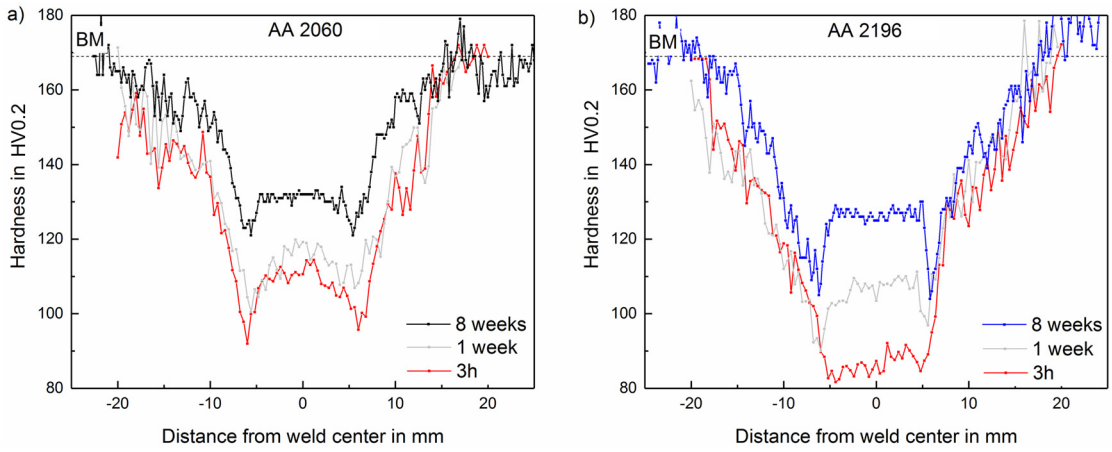

Figure 6-14 Cross-weld hardness distribution over time after welding for AA 2060 and AA 2196. AA 2196 shows more response to post-weld natural aging.

In the case of defect-free welds, the thermal cycle is the main factor for a reduction in mechanical properties in precipitation-hardened alloys in peak aged temper. Several studies have correlated the precipitation state with the mechanical properties in precipitation-hardening aluminum alloys [9,23,125]. Therefore, additional studies on the mechanical properties were carried out. In this chapter, the main results will be discussed based on tensile testing, hardness evaluation and fractography.

Tensile testing perpendicular to the welding direction was performed to assess the global strength and microhardness of cross-sections to reveal details of the local hardness distribution. A summary of the mechanical properties of the BM and the welded specimen is shown in Table 6-1.

Table 6-1 Mechanical properties of as-received (T8) and SSuBT-FSW welded material

Alloy	BM YS/UTS [MPa]	YS efficiency [%]	UTS efficiency [%]	BM hardness [HV0.2]	SZ hardness [HV0.2]	Lowest hardness [HV0.2]
2196 T8	518/572	56±2	67±3	170	130	110
2060 T8	457/512	62±1	78±2	170	135	128

Figure 6-15 represents the stabilized microhardness state of both alloys. Values were taken from mid-thickness across the weld. Starting with identical BM hardness values of 170 HV for both alloys, the hardness values in the SZ were measured as 135 HV for AA 2060 and 130 HV for AA 2196. The lowest hardness located in the HAZ was measured as 128 HV and 110 HV for AA 2060 and AA 2196, respectively. These data show a drop of 25 % (29 %) in the center of the weld, while the weakest point decreased by 29 % (39 %) for AA 2060 (AA 2196) with respect to the BM values.

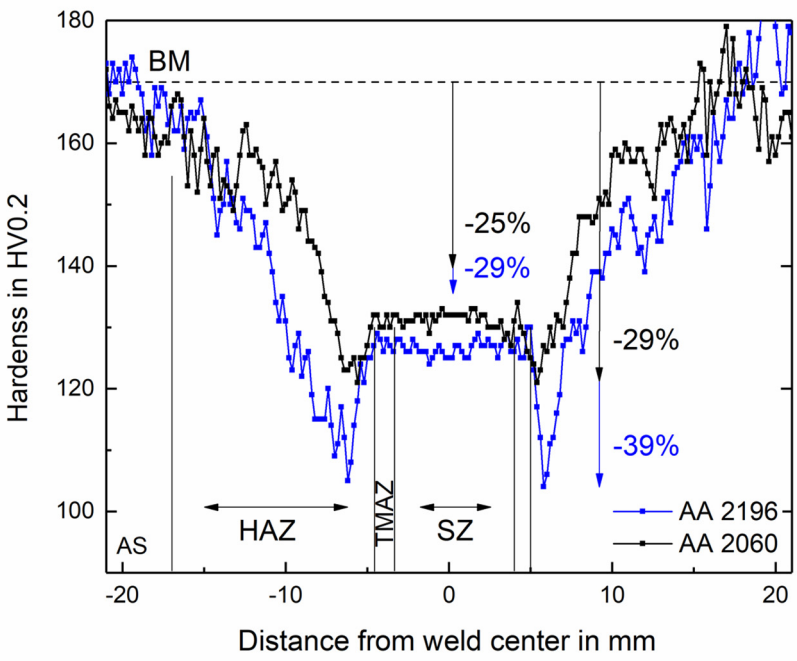

Figure 6-15 Microhardness in the post-welded state of both alloys. AA 2196 softens significantly in the point of lowest hardness located in the HAZ. Reprinted from [35], with permission of Elsevier.

Further, the base metal hardness was measured nearer to the center of the weld in AA 2060; AA 2196 presented a wider area that was softened by the process. This confirms the observation of the wider

welding zones for AA 2196 reported in Chapter 6.2. Interestingly, the typical shape, meaning the SZ width does not correlate with the center plateau seen in the hardness measurements. The welding zones known from the macrostructure are not strictly reflected in the hardness values leading to the conclusion that the precipitate evolution is the primary driver for the development of the mechanical properties. Additionally, the lowest hardness was measured outside of the SZ, where deformation did not influence the material, and the most intense softening results only from the thermal impact of the welding process. After being subjected to identical process parameters, the investigated alloys change to a different microstructure state, as seen in the previous paragraphs. With respect to the lowest hardness, AA 2196 degraded to 61 % of the base metal hardness while AA 2060 degraded to 71 % of the base metal hardness. Identical welding parameters led to a similar temperature cycle, shown in Figure 5-7, with a different hardness distribution caused by the different composition, more particularly, the Cu/Li ratio content.

6.4.2 Analysis of the tensile strength

In Figure 6-16, a comparison of the stress-strain curves of the welded and unwelded material as well as between the two alloys under investigation is shown. Under monotonic uniaxial loading, the BM values agree with the literature data and the welded samples show characteristic behavior, indicating a single fracture mode.

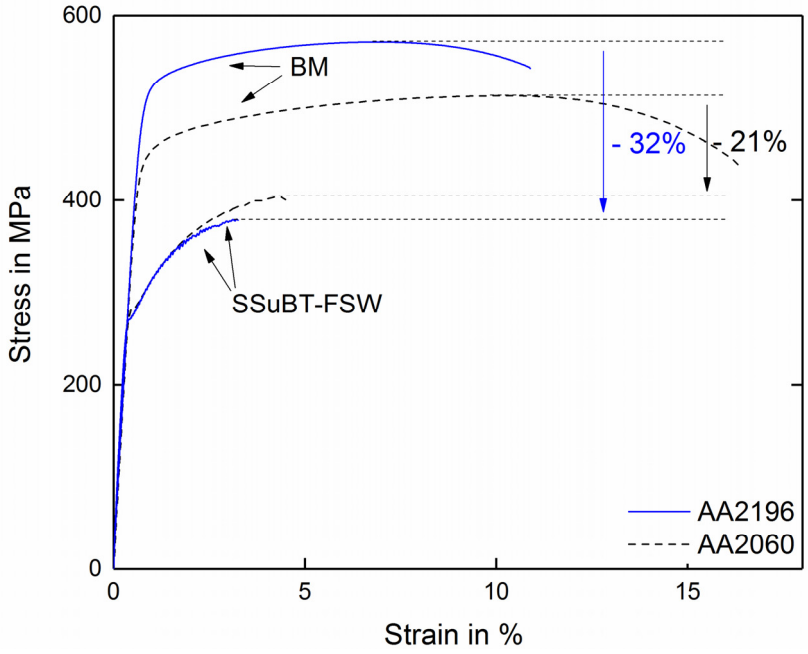

Figure 6-16 Stress-strain performance of both alloys compared to BM after welding. Tensile strength of AA 2196 is reduced to a higher extent.

Over all the tested samples, the YS degraded by 38 % ± 1.4 % and the ultimate tensile strength (UTS) was reduced by 22 % ± 2.5 % for AA 2060. For AA 2196, the YS was reduced by 44 % ± 2.2 % and the UTS was reduced by 30 % ± 2.7 %. The elongation decreased more than 75 % in both alloys, which can be attributed to the inhomogeneous nature of the weld microstructure, causing a concentration of strain in and around the weld. The weld efficiencies shown in Table 6-1, calculated as UTS/UTS_{BM}, are similar to the reported results for FSW and BT-FSW in Al-Cu-Li alloys, e.g., in AA 2060 T8 [22], AA 2198 T8 [17] or AA 2195 T8 [116].

During testing, plastic deformation led to necking on both sides of the center of the weld until the final failure occurred. All fractures were observed near the transition of the SZ and the TMAZ on the AS. The crack path followed a 45° path, where the shear stresses were the highest. A representative fracture micrograph for each alloy is shown in Figure 6-17. Although the crack propagation followed the SZ shape, it is not thought that the physical TMAZ/SZ border, with a high grain-size gradient, is responsible for the crack growth direction. This appeared in several samples, e.g., the AA 2196 sample shown in Figure 6-17, where the fracture advanced through the TMAZ as well as through the SZ. Grain size gradients and high misorientation between the two zones had a minor influence compared to the changes in precipitation morphology that caused the heterogeneous mechanical property distribution. Nonetheless, these factors might contribute differently after initial yielding because the crack propagation was not completely located in the region of the lowest hardness, rather it was closer to the SZ. This might be attributed to geometrical heterogeneities.

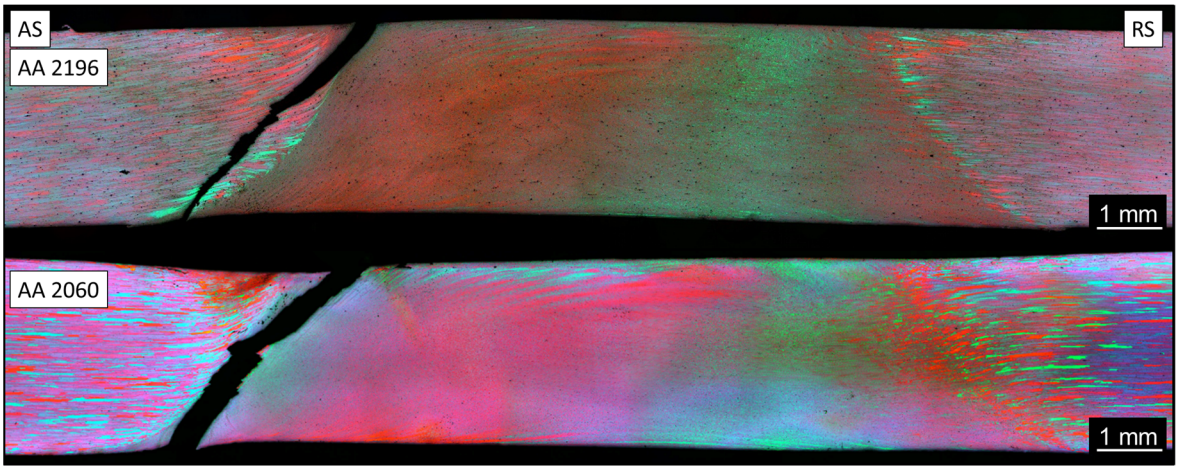

Figure 6-17 Fracture modes for welded AA 2060 a) and AA 2196 b). Both alloys fractured on AS close to the border to SZ. Reprinted from [64], with permission of Springer.

All fractured surfaces featured a primary ductile behavior showing microvoid coalescence with components from trans- and intergranular crack propagation. Detailed images of the fracture surface for

both alloys are shown in Figure 6-18. Large dimples were observed in both alloys. Second-phase particles are visible, accounting for the ductile fracture nucleation. The intergranular artifacts resulted from grain boundary shear. Both alloys also exhibit very fine dimples at high magnification (compare the details in Figure 6-18 a1) and b1)) which have nucleated from fine disperse phases. The fracture surface of AA 2196 alloy exhibited larger grains resulting from the extrusion process as seen previously in the BM prior to welding. Comparing both materials, alloy 2196 shows a higher intergranular fraction, which can be attributed to the larger grains.

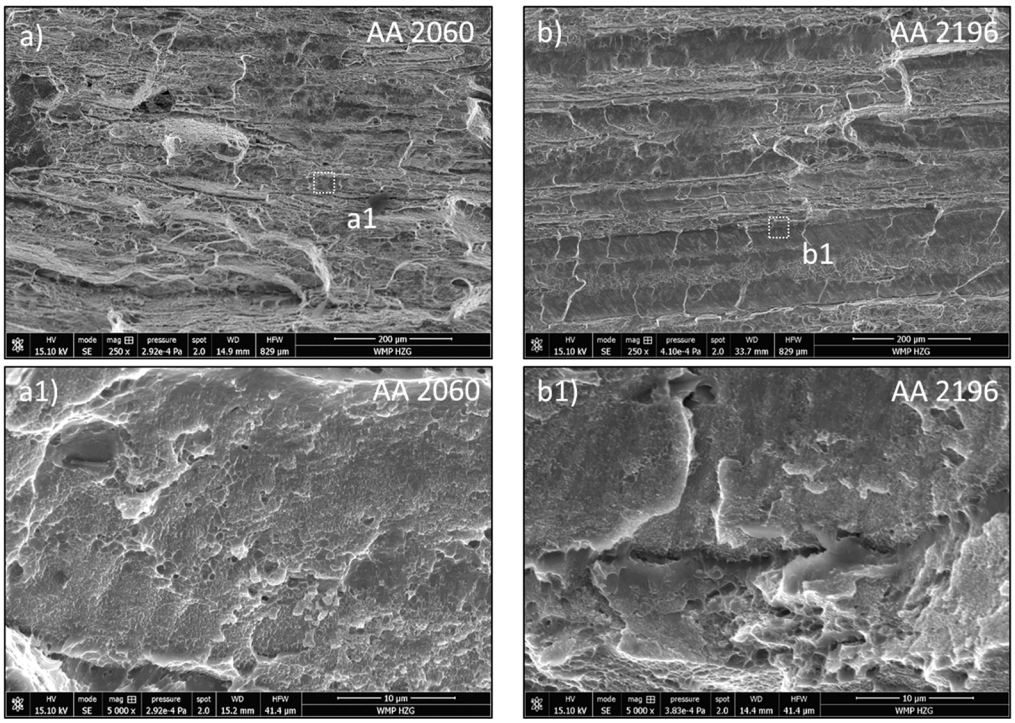

Figure 6-18 Fracture surfaces of welded coupons for AA 2060 a) and AA 2196 b). Reprinted from [64], with permission of Springer.

The mechanical performance of both alloys under investigation in welded and unwelded condition has been determined. Considering that this is the first focused attempt in welding this alloys with the SSuBT-FSW process, the efficiencies are high, and comparable to other peak aged (T8) Al-Cu-Li alloys welded using optimized FSW parameters. The achieved efficiencies are 78 % for AA 2060 and 67 % for AA 2196. Mechanical heterogeneity has been determined by microhardness analysis and shows a characteristic W-shape across the weld. Again, the hardness measured in AA 2196 was lower than that for AA 2060 in the location of the lowest hardness, which is taken as the weakest component of the weld in the given load case. Both alloys show a significant potential of natural age hardening during the first eight weeks after welding; however, this effect is more pronounced in AA 2196.

6.5 Summary

In this chapter, the microstructure and mechanical evolution during SSuBT-FSW welding of the two Al-Cu-Li alloys of interest were presented and discussed. It is well known that microstructural changes lead to significant changes in material properties. Therefore, the microstructure was analyzed prior to and after the welding process. Additionally, in situ temperature measurements supported the characterization of the microstructure evolution during the welding process. These findings were correlated to the mechanical properties and the local mechanical performance of the weld.

AA 2060 T8

Alloy 2060, with a high Cu/Li ratio, showed a microstructure characterized by the main strengthening T1 precipitates in the as-received T8 state. In addition to the dominating precipitate T1, this temper holds minor volume fractions of small, spherical precipitates θ' as well as equilibrium phases T_2 and T_B, which can be viewed as impurities because there are no known strengthening functions related to these phases. After welding, the T1 volume fraction decreased towards the center of the stir zone. The SZ consisted of only very few reprecipitated T1 phases; this region mainly consists of naturally aged phases, such as Al-Cu clusters, δ' phases and equilibrium phases.

The HAZ contained a high volume fraction of overaged precipitates. Compared to the SZ, a greater amount of solute elements is still bound onto the phase structures and not available for post-weld natural aging. This led to the development of a heterogeneous distribution of the mechanical properties perpendicular to the welding direction. Microhardness measurements identified the lowest hardness at approximately 6 mm from the weld center, where the hardness decreased by 29 % of the BM hardness while the hardness in the SZ decreased by 25 %. Because of the low YS in this position, necking appeared during tensile testing and final failure occurred at 78 % of the BM UTS, showing a single fracture mode in the TMAZ/SZ border region. This location showed the most unfavorable microstructure constitution with partial dissolution and overaging phenomena.

AA 2196 T8

Alloy 2196, with a low Cu/Li ratio, was characterized by the main strengthening precipitate T1 in the as-received T8 temper. Other phases in the analysis were equilibrium phases of the T_2 and T_B types and small finely distributed δ' precipitates, which formed at low temperatures during the natural aging processes. After welding, the center of the weld experiencing the highest temperatures showed a high fraction of dissolution of the strengthening precipitates. The amount of equilibrium phases was increased after the welding process as a consequence of the heat exposure, while the amount of δ' precipitates increased as a consequence of reprecipitation during post-weld natural aging.

Hardness measurements showed a high heterogeneity after welding where the hardness of the center decreased by 29 % and the lowest hardness was measured 7 mm from the weld center with a decrease of 39 % of the BM value. During tensile testing, the area of the lowest hardness showed early, resulting in a UTS efficiency of 67 % compared to the BM. A single failure mode propagating at 45 ° near the TMAZ/SZ border was observed. This area is near to the position of the lowest hardness, where severe dissolution and overaging reactions occurred. Microstructure analysis showed a high number of overaged particles, assumed to be T_2, which form preferentially at high Li availability. The dissolution of T1 precipitates caused Cu and Li to be available for subsequent phase formations. After the process, a high response to natural aging was observed in the DSC analysis and in the hardness development over time.

Comparison of the two alloys under investigation

Mechanical testing of the two alloys indicated good weld efficiencies compared with the state-of-art literature. The identical process parameter were employed in both alloys; therefore, the parameters and consequent results were not necessarily optimal for both alloys. Nonetheless, efficiencies of up to 78 % UTS showed that high quality welds were achieved. The lowest hardness was located near to the SZ; it is usually located further from the center of the welds. In the area of the lowest hardness, AA 2196 showed more softening, resulting in a lower overall strength of 67 % compared to the BM UTS. AA 2060 showed a higher weld efficiency of 78 % of the BM UTS. The final fracture appeared even closer to the SZ in a similar mode for both alloys.

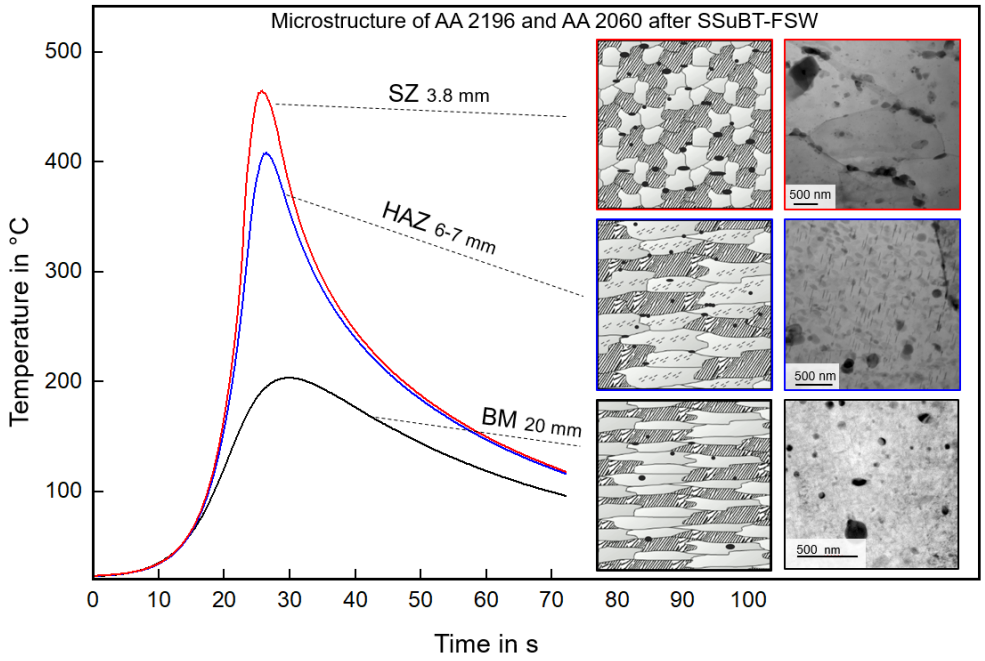

Figure 6-19 SSuBT-FSW thermal cycle and resulting microstructural appearance for Al-Cu-Li alloys. Shown are schematic illustration and TEM images of SZ showing coarse phases at the grain boundaries, HAZ showing overaged particles and GBP and BM indicating the initial state consisting from fine, distributed T1 precipitates and occasionally coarse phases.

Comparing the two alloys, the low Cu/Li alloy 2196 showed more δ' phase reactions, while AA 2060 showed fewer δ' reactions. Precipitates forming at low temperatures were also related to Al-Cu clustering in AA 2060. In general, the low Cu/Li composition in AA 2196 allowed more phases to form during the natural aging processes. Although a higher volume fraction of precipitates formed during natural aging in AA 2196, it did not contribute significantly to the overall strength because the SZ hardness was similar in both alloys after welding. The microstructure evolution resulting from the respective thermal cycle is illustrated in Figure 6-19 for both alloys. Three characteristic regions were identified and characterized.

7 Corrosion

Corrosion is a natural process of degradation that is observed on metals when exposed to corrosive environments. In the present chapter, the corrosion behavior of the two alloys of interest is investigated. To gain a greater insight into the corrosion mechanisms influenced by the welding process, the materials are analyzed in the as-received (T8) condition and in the welded condition.

In Chapters 7.1 and 7.2, the analysis of the general corrosion behavior of both alloys in pre- and post-welded conditions by immersion testing and electrochemical analysis is presented. Described in Chapter 7.3, the material was additionally subjected to stress. This scenario explored in-service conditions, where stress-related corrosion phenomena might occur. SCC tests are conducted and analyzed for the first time for friction-welded AA 2196 and AA 2060 alloys. A detailed discussion combines the findings of the corrosion analysis with the welding history and gives a detailed picture of the resulting corrosion properties that can be expected when friction stir welding Al-Cu-Li alloys.

7.1 Base metal corrosion analysis and the influence of the Cu/Li ratio on general corrosion

For an overview of the corrosion degradation under a saline solution, optical micrographs of AA 2196 T8 and AA 2060 T8 are taken after 30, 60 and 120 minutes of exposure to 3.5 % NaCl solution. The results are presented in Table 7-1. The samples showed similar behavior for the two alloys. Occasional attacks are observed after 30 minutes of exposure to constituent intermetallic particles along the grain boundaries. These particles are aligned in the orientation of the mechanical working direction (longitudinal). The intermetallic particles corroded immediately after exposure and were strongly attacked after 60 minutes (black dots in the micrographs in Table 7-1). From 120 minutes of exposure, the entire surface showed corroded artifacts while the intermetallic particles slowly formed pits surrounded by a protected area, usually referred to as a corrosion pit [126].

Table 7-1 Surface degradation of the unwelded base metal exposed to a 3.5 % NaCl solution

BM	30 min	60 min	120 min
AA 2060 T8	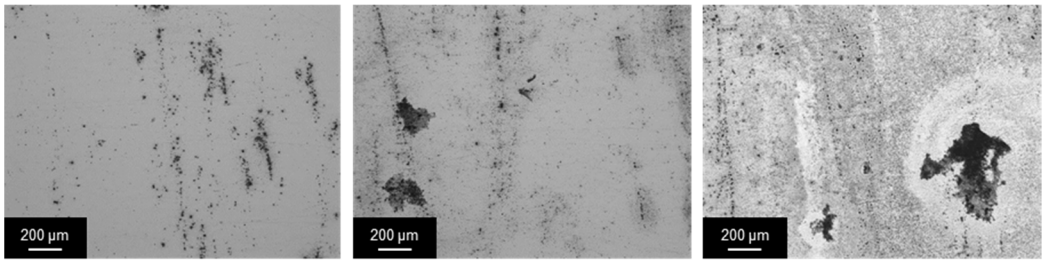		
AA 2196 T8	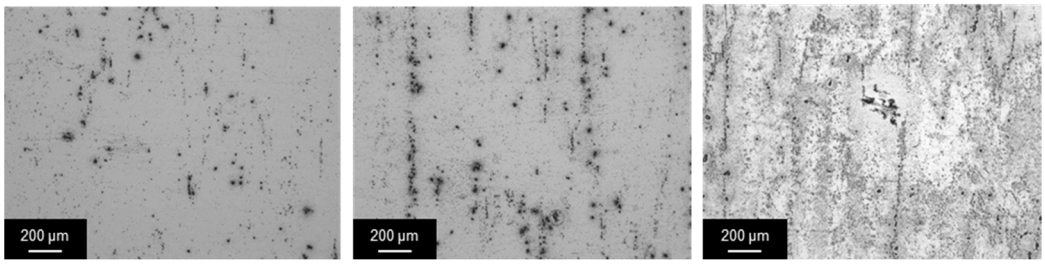		

These constituent particles have a high concentration of noble, high-melting elements, such as copper, iron, nickel and silver and are known as insoluble particles formed during homogenization [106]. Therefore, their potential was nobler than the surrounding matrix, thus acting as the cathode and forming a galvanic cell. This resulted in degradation of the surrounding Al matrix in form of anodic dissolution, as observed in Figure 7-1. These observations were found in agreement with immersion tests on other Al-Cu-Li alloys [127].

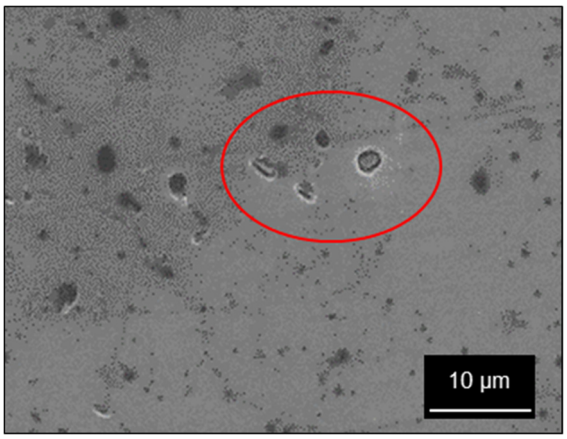

Figure 7-1 Constituent particles leading to anodic dissolution of surrounding matrix in AA 2196 T8 after 30 minutes of immersion in 3.5 % NaCl solution.

Upon immersion, the severe localized corrosion propagated further over the whole sample surface. The attacked sites grew to pits, as shown in Table 7-1 (60 min, AA 2060). This localized attack was influenced by crystallographic imperfections that led to corrosion propagation on imperfections, such as dislocations, grain boundaries and other lattice defects, as shown in the high resolution image in Figure 7-2. Crystallographically propagating pits are observed for other Al-Cu-Li alloys, and the preferential precipitation of T1 phases at dislocation sites was identified as the main reason for this [127,128].

In detail, this phenomenon originates in the slip bands observed for these alloys. Altering the bands of high deformation led to bands of T1 precipitates that nucleate preferentially at dislocations. Consequently, the grains are composed of T1-rich and T1-free bands. Furthermore, the slip bands were shown to be parallel to $\{111\}_{Al}$, indicating a grain orientation dependency [129]. Among others, this has been investigated by Ma et al [130] to explain the crystallographic pit propagation.

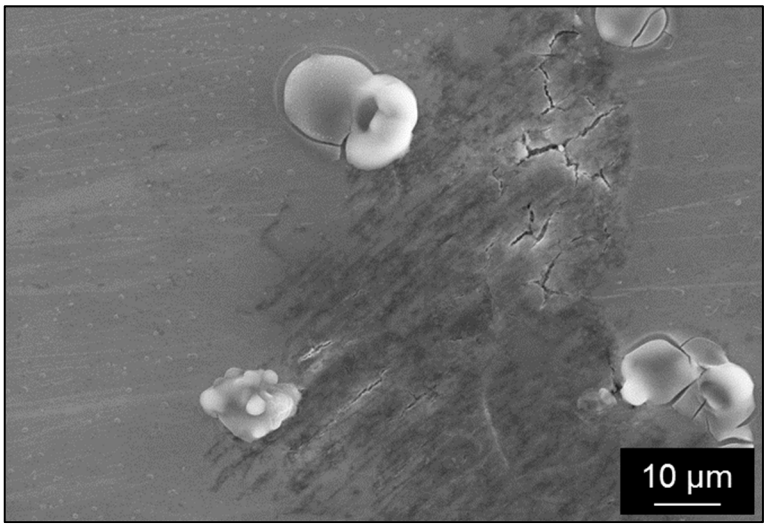

Figure 7-2 Localized pitting propagating on crystallographic imperfections observed on AA 2196 BM after 120 minutes exposure to 3.5 % NaCl. The pit is surrounded by corrosion products.

A similar corrosion mechanism was also recently reported for AA 2198 T8 [131], as well as for the non-Li containing alloy AA 2219 [132], where severe localized corrosion initiated on noble constituent particles. Later, the attack propagated, leading to severe pitting corrosion of the whole surface. Intermetallic particles in the latter study were shown to contain high concentrations of the Al-Cu-Fe and Mn [132]. As a further feature, corrosion rings growing from pits were observed after exposure to a saline solution, as shown in Figure 7-3. Strong anodic reactions on the attacked sites led to cathodic protection and coverage, with the corrosion products providing further protection of the surrounding matrix. This was evidenced by the appearance of corrosion spots surrounded by a circular area with little or no trace of

an attack. The formation of these corrosion rings is typical for severe localized corrosion sites and has been reported for other Al-Cu-Li alloys [128,130,133].

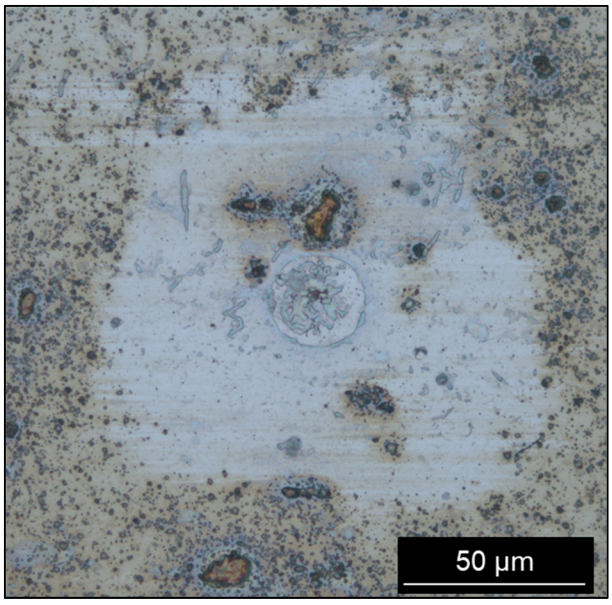

Figure 7-3 Corrosion ring on AA 2060 exposed for 120 minutes to 3.5 % NaCl solution.

In addition to the coarse intermetallic particles, smaller phases have been reported to play an important role in the corrosion behavior. The main precipitate T1 has been suspected of playing an important role in the corrosion process in Al-Cu-Li alloys, and many studies have found a correlation between the presence of T1 and an observed corrosion attack [127,131,134,135]. Areas of high T1 concentration acted as preferential corrosion sites because of the electrochemical heterogeneity of the matrix [136]. Corrosion conversion mechanisms for the precipitates T1 and T_2 (Al_6CuLi_3) have been found that include the noble Cu and the reactive Li simultaneously. Although the particle is cathodic with respect to the aluminum matrix, at the beginning of the corrosion process, the phase shows a dissolution of Li because of the less-protective character to the oxide of the particle. Because of the dissolution, Cu enriches on the surface of the precipitate, moving the potential into the cathodic region. Consequently, the precipitate becomes cathodic with respect to the surrounding matrix, which will then further be anodically dissolved [136,137].

The evolution of the open circuit potential (OCP) is shown in Figure 7-4. Both alloys showed relatively stable behavior after the initial potential drop in the first 30 minutes (1800 seconds). The alloy 2196 exhibited a lower OCP than AA 2060. Possibly, the higher Li content in AA 2196 shifted the OCP negatively.

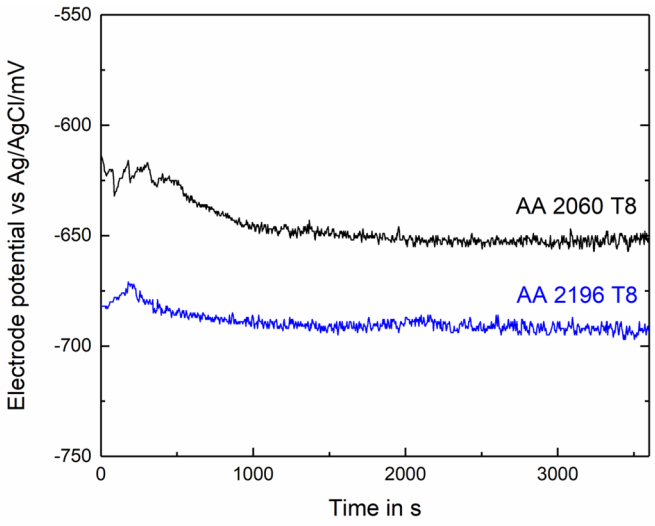

Figure 7-4 OCP measurements of the material in its as-received state over 60 minutes in 3.5 % NaCl electrolyte.

In Figure 7-5, the potentiodynamic polarization curves are shown. Both graphs show oxygen diffusion in the cathodic region with similar current densities at approximately 10^{-2} mA/cm². No evidence of passivation was detected in the measurements of the anodic reaction. The corrosion potential and the breakdown potential occur simultaneously and are therefore difficult to differentiate. When the potential was increased, the signal reached the breakdown potential, located very near the corrosion potential at approximately 0.01 mA/cm². This indicates a fast and spontaneous corrosion reaction. The absence of passivity in the anodic region suggests that spontaneous pitting occurs at the corrosion potential with an increasing current.

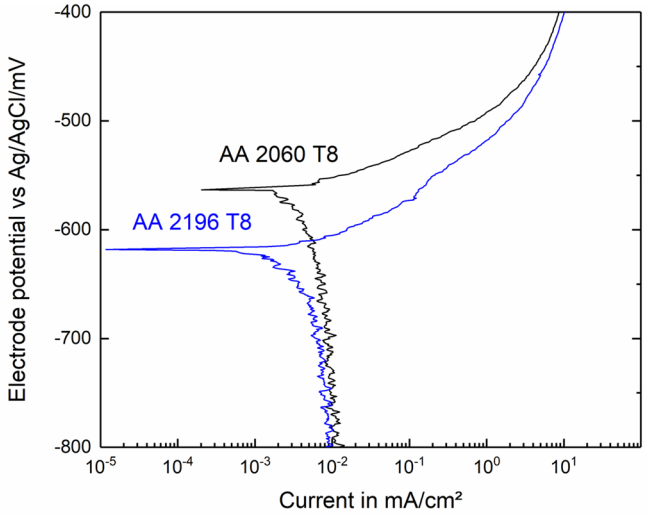

Figure 7-5 Polarization curves of BM for both alloys in 3.5 % NaCl solution. AA 2060 shows a higher corrosion potential.

The corrosion potential for AA 2196 is -613 mV and consequently more negative than the measured corrosion potential for AA 2060 (-561 mV), suggesting a kinetically driven, higher susceptibility to corrosion in AA 2196.

The localized corrosion mechanism of the Al-Cu-Li alloy is illustrated in Figure 7-6. First, shown in Figure 7-6 a), constituent particles, usually containing higher amounts of nobler elements, such as copper or iron, become attack spots for oxygen reduction and hydrogen evolution (reduction), resulting in an anodic dissolution of the matrix near the particle. As hydrogen evolution is not typically expected at the measured potential, it might still form in the pits, where the pH value is strongly acid, or from self-activity on the particles (micro galvanic coupling between elements within a single phase). Micro galvanic cells between the particles and surrounding matrix are the reason for localized corrosion because these surface-near intermetallic phases interrupt the formation of a homogenous oxide layer. Later the localized corrosion propagates and forms pits as shown in Figure 7-6 b). The micro galvanic cell evolves to a pit which preferably grows on crystallographic defects. Ultimately these pits will connect forming a large, attacked surface area.

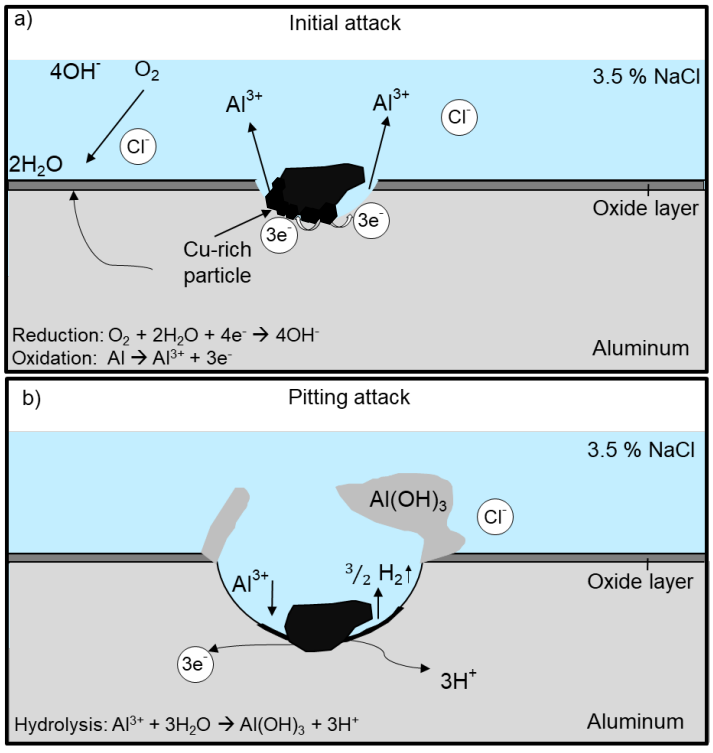

Figure 7-6 Illustration of initiation a) and progressing b) localized corrosion attack. Surface corrosion start on intermetallic, constituent particles and propagates into the metal forming localized pits.

Electrochemical impedance spectroscopy analysis (EIS) was performed to differentiate the corrosion mechanisms on an electrochemical basis. The Bode plots and respective theta graphs of the EIS spectra for AA 2060 BM and AA 2196 BM are shown in Figure 7-7 a)-b) and Fig 7-7 c)-d), respectively. During the test, the impedance is measured while the frequency of a low-amplitude voltage sine wave perturbation is changed. Two time constants were observed, indicating two relaxation processes. The middle frequency time constant at approximately 40 Hz is attributed to the presence of an oxide layer and the second time constant at the low frequency of 10^{-1} Hz is related to a localized corrosion process, also indicating pitting [138].

A general reduction with time is notable in both alloys. The impedance values decreased to approximately 20 % in the range of 0.2 Hz after one hour of exposure for both alloys. This decrease is attributed to the decrease of the initial oxide layer and the formation of corrosion products.

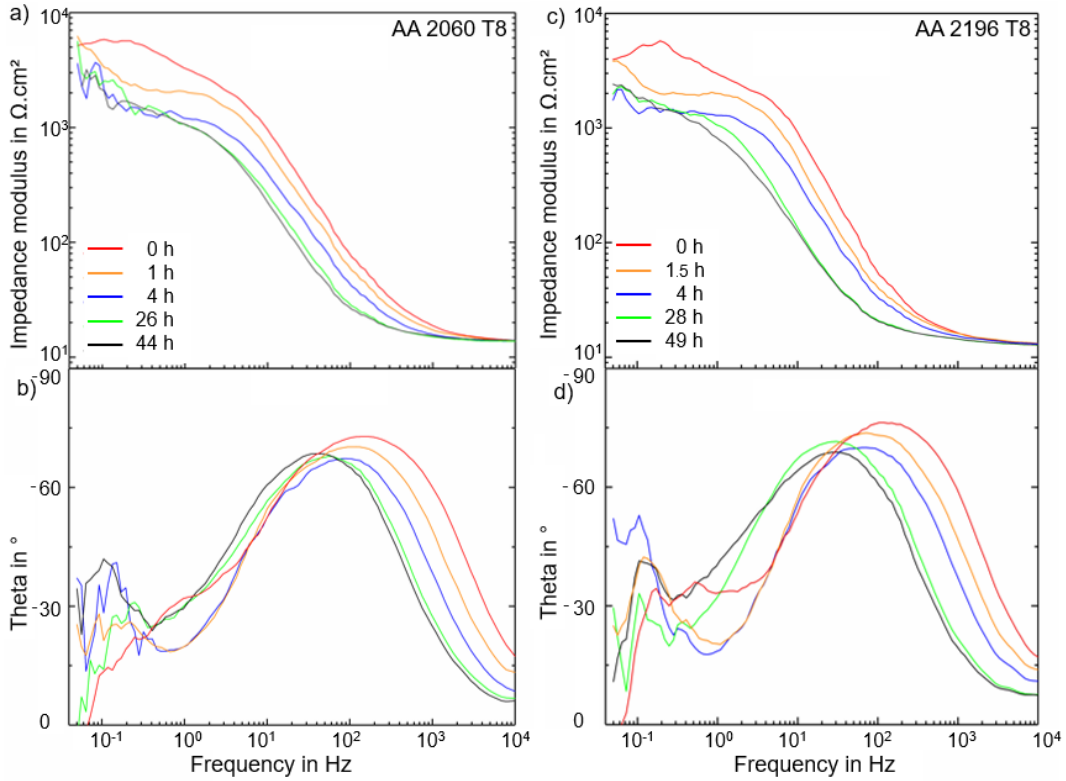

Figure 7-7 Bode plots of EIS spectra of the BM samples exposed to 3.5 % NaCl solution for AA 2060 T8 a)-b) and AA 2196 T8 c)-d).

EIS analysis is used to characterize the electrical behavior of systems in which several simultaneous processes occur at different rates; therefore, these electrochemical processes can be represented and simulated by electrical circuits. These circuits are known as an electrical equivalent circuits (EEC) and a schematic representation of the equivalent circuit for the alloys of interest is shown in Figure 7-8,

R_s is the ohmic resistance of the electrolyte, R_{ox} and the paralleled constant phase element CPE_{ox} represent the response of the oxide present on the alloy surface at middle frequencies and Z is the Warburg impedance. The CPE is used as equivalent circuit component representing the behavior of a double layer which is an imperfect capacitor. If the oxide film is permeable, the electrolyte can reach the surface of the aluminum. Therefore, the second time constant appears in the low-frequency region, which is the initiation of the corrosion process and is attributed to the existence of the double layer capacitance at the metal/electrolyte interface represented by the double-layer constant-phase element (CPE_{dl}) and corresponding charge transfer resistance (R_{ct}).

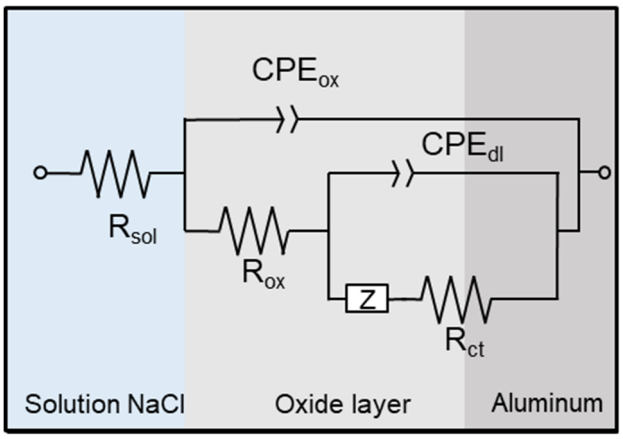

Figure 7-8 Schematic representation of the equivalent circuit for surface degradation.

Summarizing, the corrosion behavior of the as-received material can be described as locally initiated corrosion progress in both materials. The severe localized corrosion started from constituent intermetallic particles at initiation spots observed at around 30 minutes, as shown in Table 7-1. These particles have high contributions of noble elements like copper, iron and silver. At longer exposure times, the attack evolves towards a surface pitting in selected areas preferably along crystallographic imperfections. Potentiodynamic analysis showed slight differences between the two alloys under investigation, which can be correlated to the different chemical compositions. The corrosion rate is similar for both alloys because it is limited by the oxygen diffusion; however, a higher Li content in AA 2196 might lead to a lower corrosion potential. Electrochemical impedance measurements revealed two relaxation processes attributed to the presence of an oxide layer and to localized pitting corrosion.

7.2 Influence of the process on localized corrosion

After processing, the welding zones have been immersed in 3.5 % NaCl solution to evaluate the corrosion response. Representative micrographs of the surface degradation after different exposure

intervals are presented in Table 7-2. The SZ samples feature a small grain distribution with a regular, symmetrical grain boundary network. The intermetallic particles which were found initiate localized corrosion in BM material, were observed unchanged in BM and HAZ samples after welding. In the SZ location, these particles were found distributed along the equiaxed grain boundaries. Similar to the BM behavior, evolving localized corrosion was observed, where constituent particles are first rapidly activated, followed by pitting along crystallographic orientations. Compared to the pristine (unwelded) BM, the total attacked fraction was increased in the HAZ and SZ samples. Because of the small, regular grains found in the SZ, corrosion rings appear more clearly. In total, a greater number of pits developed in the SZ areas caused by the increased grain boundary density providing a high amount of potential attack locations.

Table 7-2 Surface degradation of welding zones after 30, 60 and 120 minutes of exposure to 3.5 % NaCl solution

	30 minutes	**60 minutes**	**120 minutes**
AA 2060 HAZ	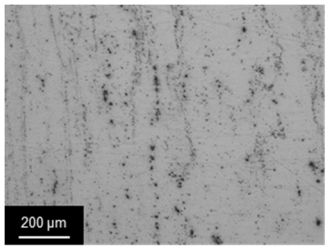	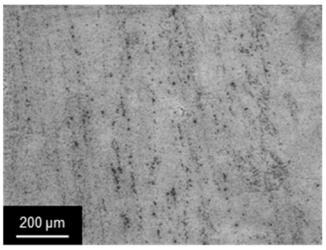	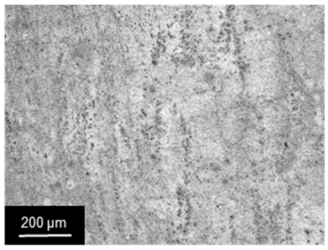
AA 2060 SZ	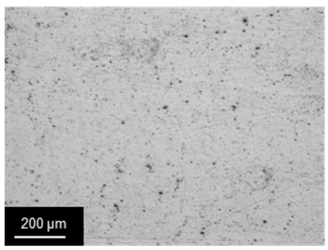	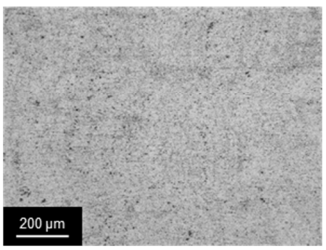	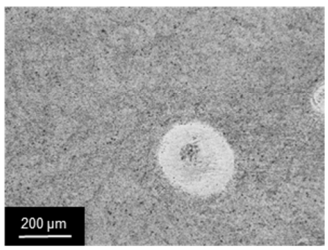
AA 2196 HAZ	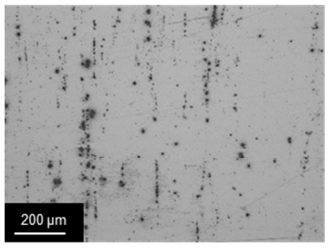	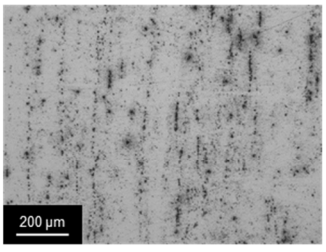	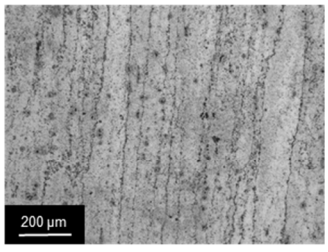
AA 2196 SZ	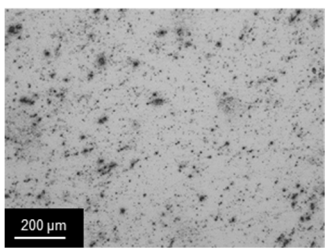	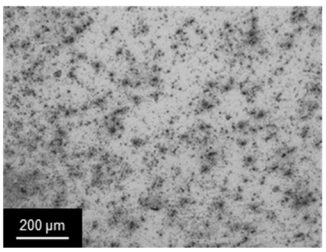	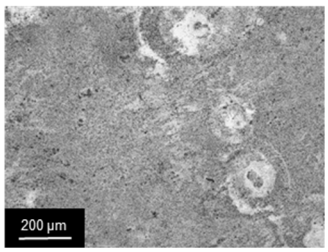

Similar to the BM, the welding zones have been analyzed using electrochemical techniques to reveal details of the corrosion response of the different zones. First, the three welding zones (SZ, HAZ, and BM) of each alloy are compared and in a second step, the results are compared between the two alloys under investigation.

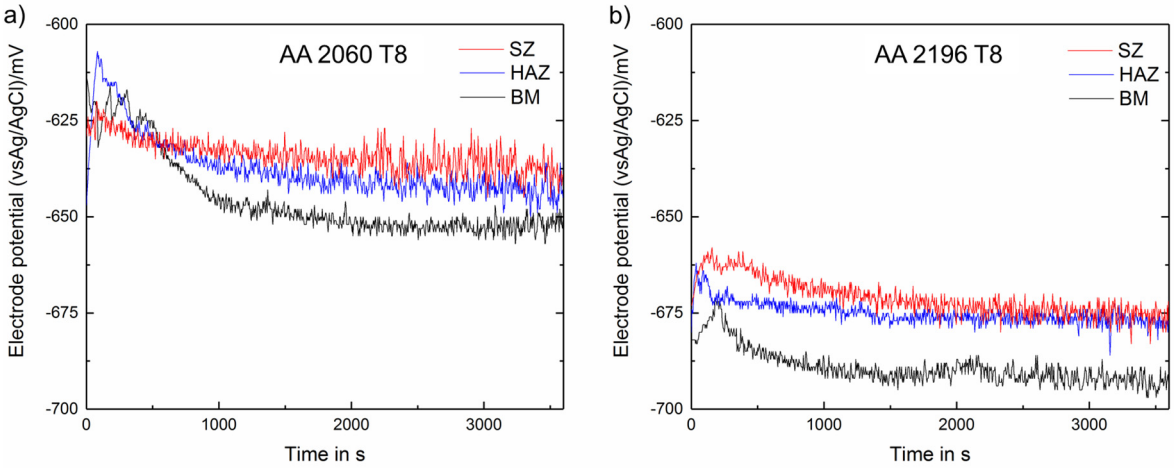

Figure 7-9 OCP measurements over 60 minutes of exposure to 3.5 % NaCl solution for welding zones of AA 2060 T8 a) and AA 2196 T8 b).

The open circuit potential curves versus time, shown in Figure 7-9, confirm the relatively stable behavior after an initial potential drop in the first 30 minutes. As seen in the BM, AA 2196 exhibited a more negative OCP in all zones when compared to AA 2060. The increased Li content causes the alloy to be more reactive. However, both alloys followed the same sequence when stabilized: $OCP_{SZ}>OCP_{HAZ}>OCP_{BM}$.

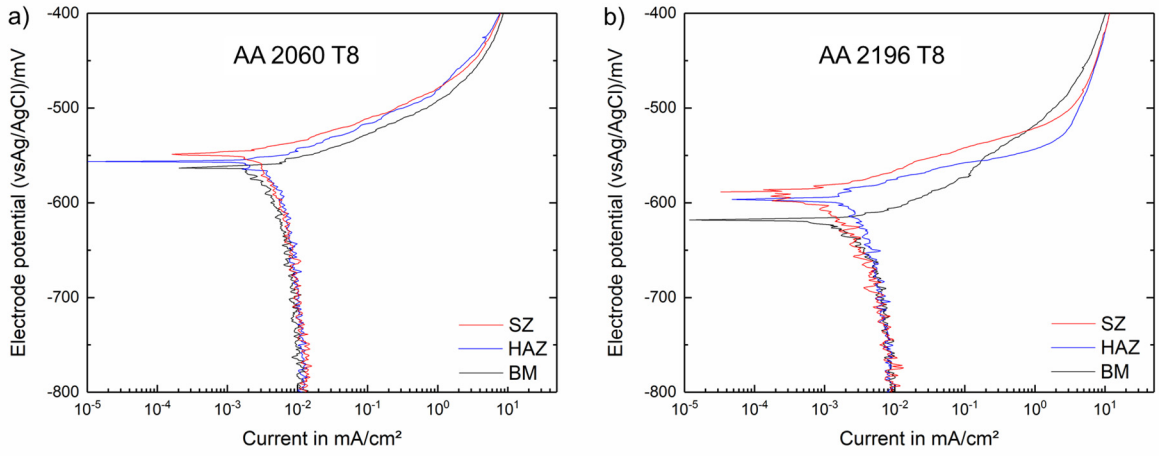

Figure 7-10 Dynamic polarization curve of AA 2060 a) and AA 2196 b) for different welding zones in 3.5 % NaCl solution.

The corrosion resistance was evaluated by a dynamic polarization technique for the two respective alloys in all welding zones. All potentiodynamic polarization curves showed an oxygen diffusion controlled process in the cathodic region with similar current densities as seen in Figure 7-10.

Similar to the findings in the BM samples, no passivation was detected in the measurements of the anodic region. However, breakdown locations were observed at OCP potential related to the breakdown of the attack of the first particles (probably T1 phase) in all samples. Later, at approximately -550 mV, a second and weaker breakdown is observed that is possibly related to the attack of the BM structure, e.g., at the grain boundaries. This second breakdown is more pronounced in the HAZ and the SZ samples for AA 2196, where more grain boundary particles have been observed in Chapter 6. These results are consistent with the OCP curves and have the same tendency (SZ>HAZ>BM). In the SZ area, the potential is nobler compared with the other zones, and may be from the reduced presence of large intermetallic phases.

7.3 Stress-enhanced corrosion

The corrosion behavior under applied stress is of special interest for academia and industry alike. While all materials in application are constrained by design requirements that may cause internal stresses, the mechanism of corrosion under stress differs significantly from the standard corrosion behavior, treated in the previous chapters. The systematic investigation of stress-enhanced corrosion is complex because the appropriate stress levels and the corrosive media must be controlled and conform to a generic procedure. In this study, the investigation aims to acquire more details on the mechanisms leading to stress-dependent corrosion in the alloys of interest. To date, stress corrosion studies have not been published on AA 2060 or AA 2196 friction-based welds. Rising interest in the stress corrosion behavior of Al-Cu-Li alloys is evidenced by recent findings of the susceptibility of intergranular, stress-related corrosion in AA 2198 T851 [131]. As seen in Chapters 5 and 6, intense thermomechanical influences led to modifications of the microstructure, resulting in different welding zones. In addition to the influence of these modifications on the mechanical properties, which were treated in Chapter 6.4, the impact on the corrosion properties under stress is crucial for design and application. At the same time, SCC mechanisms in aluminum alloys remain uncertain. While different hypotheses have been proposed, as covered in Chapter 3.3, this study provides some detailed insight into the stress corrosion response of BT-FSW processed Al-Cu-Li alloys, including a general description of the observations during testing, a detailed study of the impact on the mechanical properties and a detailed look onto the microstructural mechanisms related to the stress corrosion testing.

To evaluate the stress corrosion characteristics, a series of tests were conducted. Base metal and welded samples of both materials were exposed to 3.5 % saline solution in stressed and unstressed conditions. Testing was performed in constant-load conditions, meaning the samples were tested under a constant

loading. Because of the time-consuming test procedure, only AA 2060 was subjected to additional testing, where the different welding zones were exposed separately in stressed and unstressed conditions. This test was performed under constant elongation conditions, i.e., the absolute elongation representing the required loading in the initial state was maintained throughout the entire test. Both testing sequences followed the procedure of alternate immersion (10 minutes immersion, 50 minutes drying) for 30 days as described in ASTM G44 standard.

7.3.1 Stress corrosion behavior of the base material

Prior to exposing the welded specimens to the test environment, the behavior of the BM was determined. Neither AA 2060 nor AA 2196 have ever been tested for SCC; therefore, the evaluation of the BM is performed to set a valid reference. Figure 7-11 shows the exposed samples after tensile testing, which was performed to determine the residual strength. After exposing the specimen testing environment, significant changes were observed visually on the surface. Nonetheless, all samples under evaluation survived the test without failure. After removal of the corrosion products, randomly distributed pits were observed on the surface. AA 2196 showed pits more pronounced in the longitudinal direction, as shown in Figure 7-11.

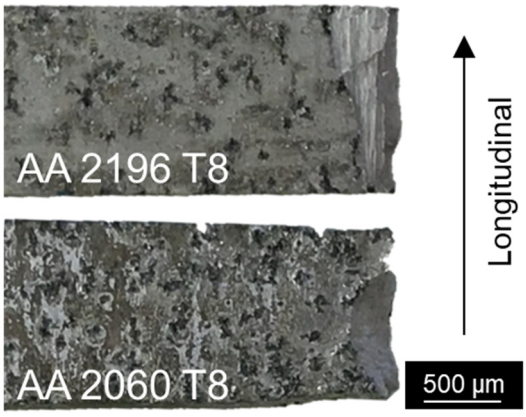

Figure 7-11 Surface appearance after 30 days of alternate immersion exposure in 3.5 % NaCl solution and removal of the corrosion products.

Throughout the surface, localized pitting attacks were observed. Over a sampled length, the pit density was taken at mid thickness and found similar for the two alloys. The average pit depth was determined via microscopic measurements to 102.7 ± 27.3 µm and 81.9 ± 40.9 µm for AA 2060 and AA 2196, respectively. The different grain morphology also resulted in a different pitting appearance, as shown in Figure 7-12. AA 2060 suffers a grain attack that is primarily restricted to a single grain dissolution. Once that grain is dissolved, the pit propagates along the grain boundaries to the next susceptible grain. Certain

grains appear more susceptible to corrosion attack than others. This phenomena was described as selective grain dissolution [128,139]. It has been observed for various Al-Cu-Li alloys and was recently investigated by Ma et al. [130]. The authors investigated AA 2099 T8 and found that localized corrosion, evident by selective attack on grain boundaries and individual grain interiors, was correlated to the inhomogeneous distribution of T1 precipitates.

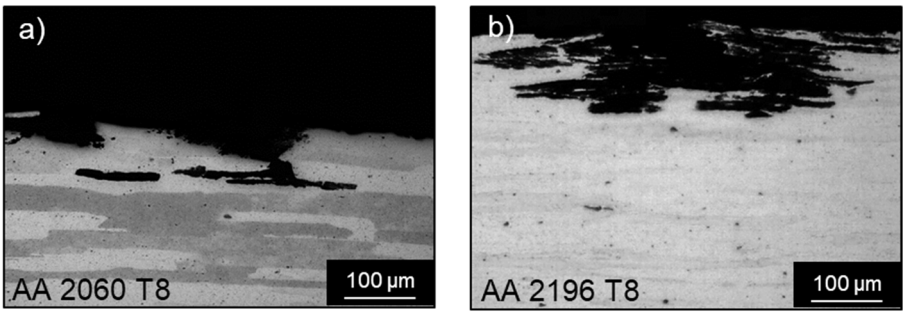

Figure 7-12 Pitting attack in stressed BM samples exposed to 3.5 % NaCl solution. Selective grain dissolution was observed in AA 2060 and selective grain dissolution with exfoliation characteristics occurred in AA 2196 material.

Further, it was found that grains with a large Schmid factor were preferential attack locations because these grains will experience more deformation leading to a higher dislocation density and thus to a higher precipitation of T1 phases. While AA 2060 showed this phenomenon, the different grain morphology in AA 2196 resulted in a different appearance, intermixing with exfoliation characteristics. Selective grain dissolution was observed, leading to localized pits. Because of the high aspect ratio of the grains, they were not fully dissolved before the next grain was attacked. AA 2196 was analyzed from an extruded base material; therefore, a generally larger Schmid factor might lead to a decreased attack threshold.

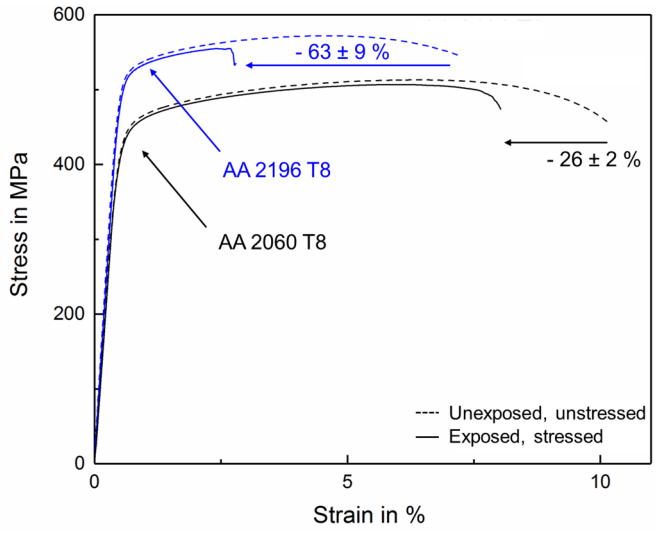

Figure 7-13 Stress-strain curve of BM samples after SCC testing in 3.5 % NaCl solution. While the strength was barely not reduced, the ductility was highly affected by the exposure, especially for AA 2196.

The residual strength was determined after the exposure and is shown in Figure 7-13. Neither of the alloys lost any significant strength. The YS were similar, while the ultimate tensile strength was slightly lower with a decrease of 1 % ± 0.2 % for AA 2060 and 3 % ± 1.5 % for AA 2196. Significant changes appeared in the decrease of the elongation, which is decreased by 26 % and 63 % for AA 2060 and AA 2196, respectively. Pitting and hydrogen-induced embrittlement via cathodic charging during the exposure can lead to a loss in ductility [72] as shown in the two alloys of interest. The corrosion phenomena observed in this study for stressed Al-Cu-Li alloys in T8 temper would lead to a classification of level 1 following the ECSS-Q-ST-70-37C classification [140] which means a survival of the samples with a residual strength above 90 % of UTS and no microscopic evidence of SCC at 50x magnification.

7.3.2 Stress corrosion behavior of the weldments

To investigate the welded specimens, two testing procedures were chosen. First, constant load testing, according to the ASTM standard, was conducted, analogous to the procedure subjected to the BM. As a second test, the individual welding zones were separated and tested individually in constant-extension mode at different loading levels. All samples have been tested against control samples that were not loaded but exposed to the corrosion cycle.

Constant load testing was performed on welded specimens with a load of 75 % of YS, according to the standard. All tested samples survived the testing duration. Visual inspections revealed severe corrosion attacks, confirmed by the appearance of corrosion products, as shown in Figure 7-14 a). After removal of the corrosion products, the pitting attack was observed following the known grain structure. The BM and the HAZ appear similar with respect to the surface pitting, shown in Figure 7-14 b); however, the SZ exhibits round symmetrical pits (Figure 7-14 c) as a result of small equiaxed grains.

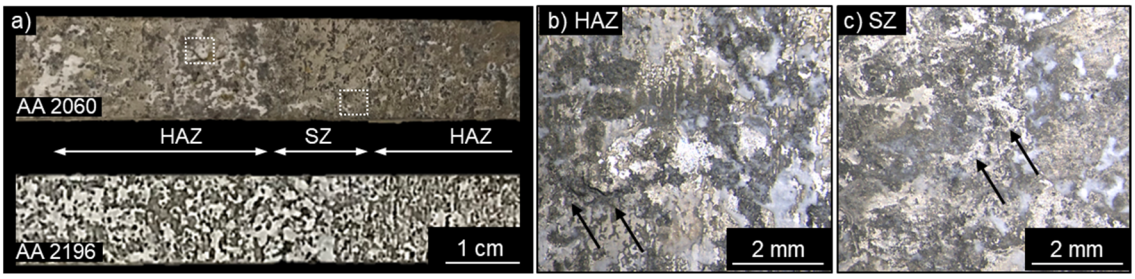

Figure 7-14 Surface appearance of a welded specimen after SCC testing a) and close-up on pit formation in HAZ b) and SZ c). The arrows indicated the pits following the grain structure in the welding zones.

The pit distribution is shown in Figure 7-15. For stressed and control samples, the pit location and depth was determined at mid thickness of the tested samples. The data show that the overall pit count remains

similar, independent of the loading condition. The SZ area experienced more pitting, which is related to the smaller grains, where more grains pose a susceptible orientation. However, the pits in the HAZ developed under load differ from the control (unloaded) ones in depth. Deeper pits were observed for loaded specimens, reaching 270 µm for AA 2060 and 190 µm for AA 2196 (59 µm for AA 2060 and 52 µm for AA 2196 in unloaded HAZ state). The stress led to enhanced pit growth in the HAZ. Additionally, pits developed deeper in the HAZ located closer to the weld center. The pits were randomly distributed over the selected welding zone, and there is no evidence of interaction between the welding zones that would promote pit accumulation at the welding zone borders.

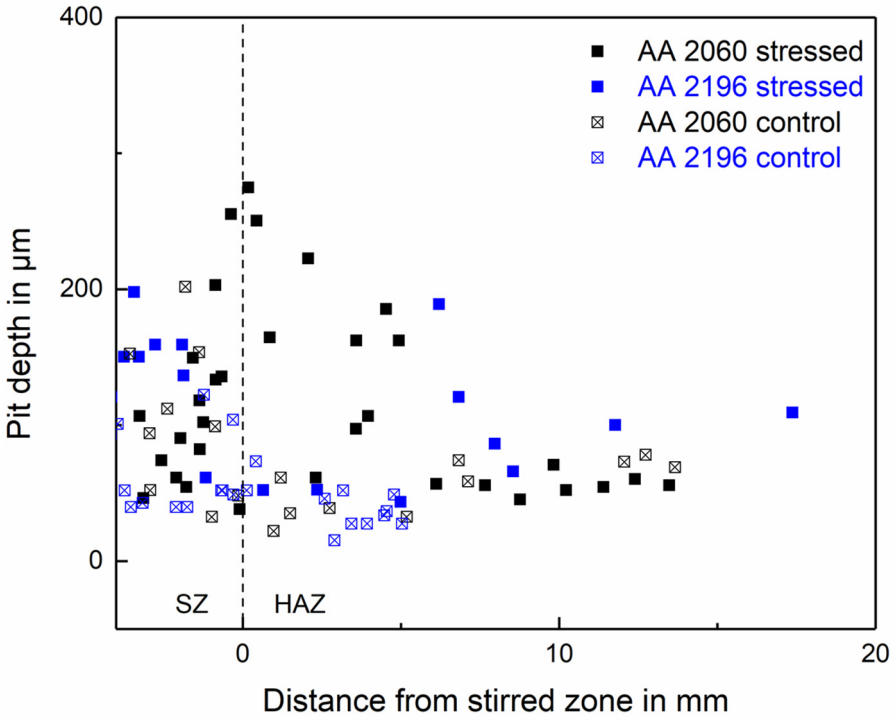

Figure 7-15 Pit distribution of the welded sample surface after stress corrosion testing in 3.5 % NaCl solution. The HAZ shows deeper pits when samples were under load for both alloys.

A general overview of the corroded samples is shown in Figure 7-16. The overview images were taken after the evaluation of the residual strength, and no fractures appeared during the stress corrosion testing. As seen in the top view in Figure 7-14, round pits are evident in the SZ of both alloys, while elongated pits are visible in the outer areas. For AA 2196, exfoliation is visible because of the extruded grains. Pits in the HAZ develop differently when a load is applied. On the macroscopic scale, pits formed under a load develop deeper and seem to embrittle the outer grain layers, as indicated on both alloys by arrows in Figure 7-16.

All samples fractured in the region between HAZ and SZ and not at the location of deepest pitting. However, stressed samples fractured at lower loading levels, indicating a higher surface degradation that can be confirmed by analysis shown in Figure 7-15.

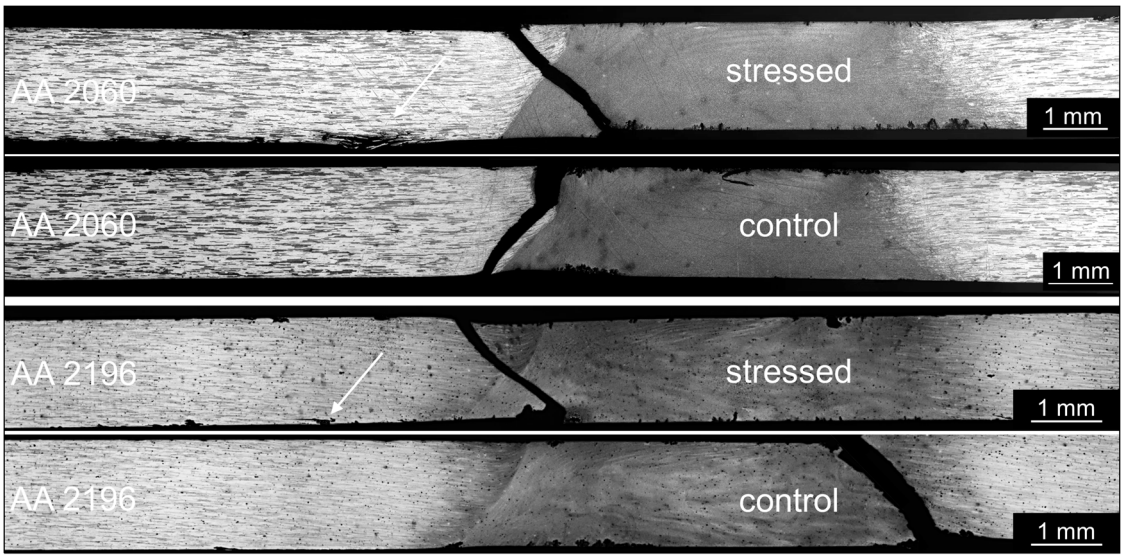

Figure 7-16 Fracture location macrographs of SCC tested samples after residual strength testing for both alloys. Deepest pits occurring in the HAZ (arrows) did not lead to the final fracture.

Detailed cross-section images of representative corrosion attacks are shown in Table 7-3 for each zone and both alloys. While the BM section presented the same selective grain attack as observed in the plain BM samples shown in Chapter 7.3.1, the HAZ and the SZ exhibit different mechanisms. The pitting attack in the SZ is characterized by round pitting, which is related to the grain structure. As selected grains get attacked individually, these are quickly dissolved and the pit propagates to the next susceptible grain. Because the diameter of the grains was 7 μm, they caused symmetrical round pit growth in both conditions, loaded and unloaded. In the HAZ region, the pit development differed from the loaded to the unloaded condition. The unloaded control sample features selective grain dissolution phenomena similar to that observed in the BM. The loaded samples show significantly deeper pits and a grain boundary dissolution leading to intergranular cracking. This intergranular corrosion (IGC) was especially pronounced for AA 2060 while in AA 2196 the stress enhanced corrosion shows a fine cracking network and exfoliation characteristics.

Table 7-3 Details of the microstructure of the welding zones after SCC testing in 3.5 % NaCl solution

	SZ	HAZ	BM
AA 2060 stressed	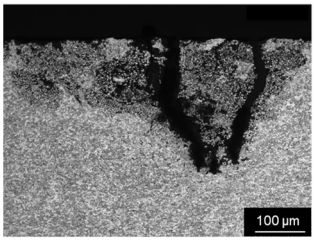	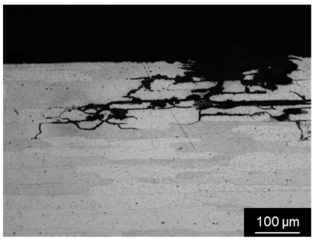	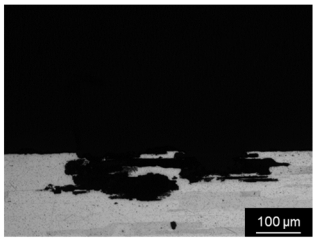
AA 2060 control	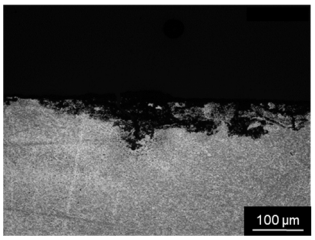	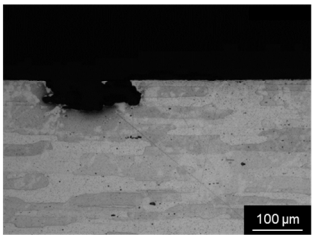	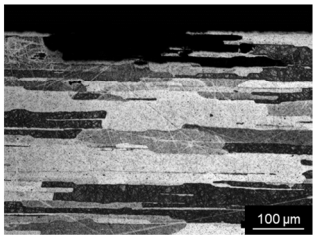
AA 2196 stressed	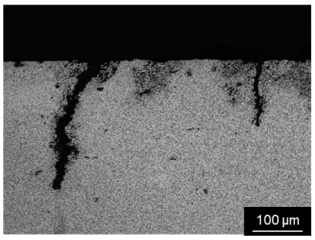	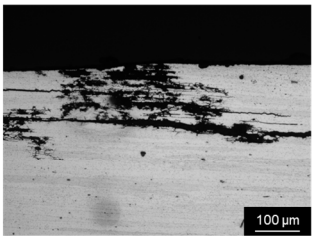	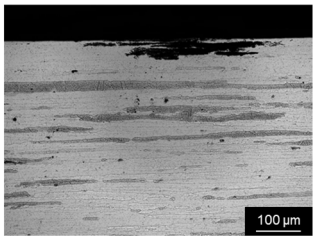
AA 2196 control	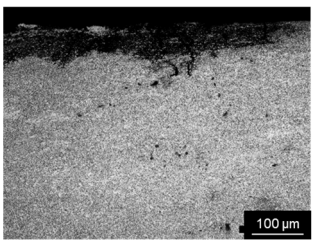	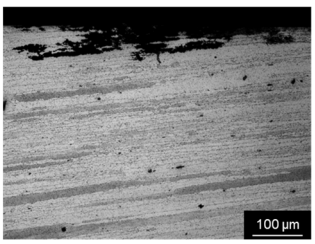	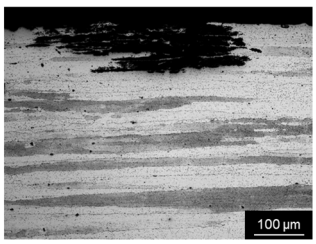

All samples survived the exposure period; therefore, it was possible to determine the residual strength by tensile testing. The results of the residual strength efficiencies with regards to the pristine BM properties are presented in Figure 7-17 for AA 2060 and in Figure 7-18 for AA 2196. A full table of numerical results is included in Appendix D. For better clarity, a statistical comparison of the BM in its as-welded condition and the SCC-tested condition was repeated a), and the comparison between the SSuBT weld in its as-welded, exposed and unstressed condition (control) is shown in b). Figure 7-17 a) confirms that the welded specimen was more susceptible to degradation during the SCC testing, and both the YS and the UTS were reduced compared to the BM material. This is especially evident when looking at the UTS, which was reduced in the SCC-tested SSuBT weld. More details are visible when the residual strength was compared to the weld efficiency of as-welded samples, in Figure 7-17 b). The SCC-tested weld shows an 18 % lower UTS compared to the untested sample and a decrease of 9 % with

regards to the control samples. The data show that both influences, the alternate immersion exposure and the loaded condition, contribute to the loss in strength. The significant loss in UTS accompanies the loss in ductility seen in the BM in the previous chapter.

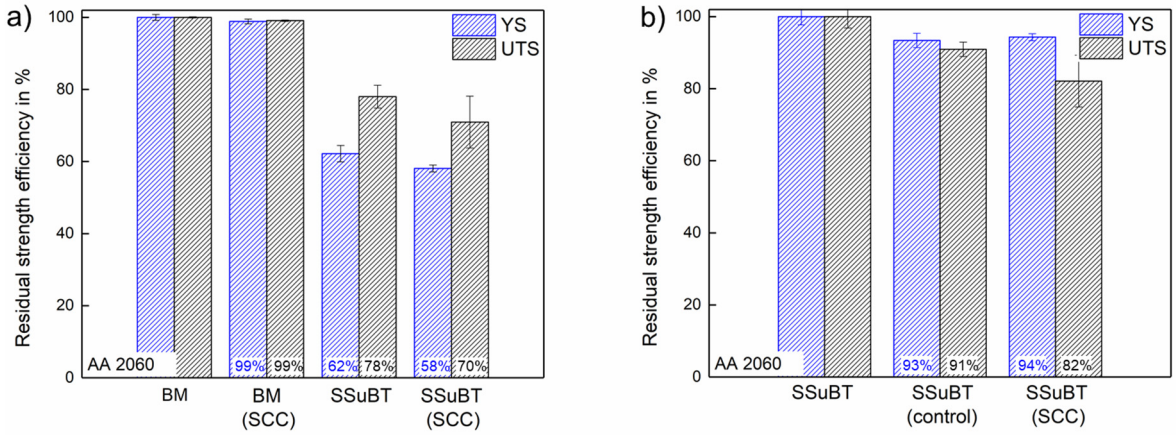

Figure 7-17 Residual strength efficiencies with regards to BM a) and SSuBT b) welds of AA 2060.

The resulting residual strength for AA 2196 is shown in Figure 7-18. Graph a) shows the residual strength efficiencies in the BM. The decrease of the UTS showed that the weld was more influenced by the SCC testing than the BM. In graph b), the comparison with the control sample revealed that the additional stress led to a decrease, primarily in the UTS. The UTS was reduced by 10 % in the control sample and an additional 13 % when the sample was stressed. A slight stress-related decrease in YS was observed that was not notable in AA 2060.

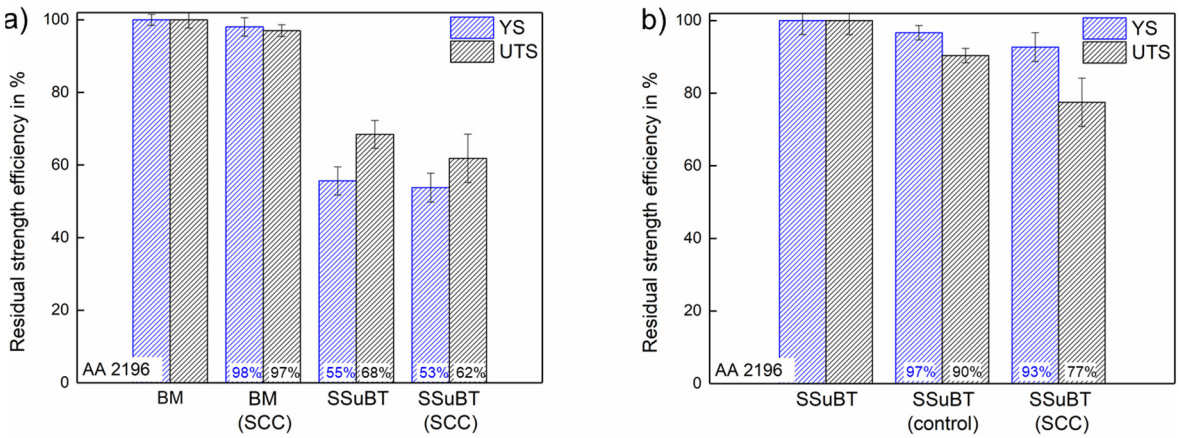

Figure 7-18 Residual strength efficiencies with respect to BM a) and SSuBT b) welds of AA 2196.

The SCC results presented in this chapter confirm that the welded specimens are more susceptible to SCC than the BM material is. In this study, the data showed that the HAZ was the primary location where the pits developed deeper. The final fracture during the determination of the residual strength was initiated in the HAZ of the SCC-tested specimens, as shown in Figure 7-16. The control samples followed a similar fracture location as seen in the as-welded samples shown in Chapter 6.4.2. Stress-enhanced corrosion mechanisms are working during the exposure to saline solution.

When the influence of the Cu/Li ratio was considered, only minor differences were seen in the corrosion results of the welded specimens. In addition to the lower mechanical properties of the weld itself, AA 2196 experienced a similar SCC-related degradation with respect to the as-welded performance and compared to AA 2060.

7.3.3 Details of the mechanism of stress-enhanced corrosion

To explore the pit growth in the two regions where intense microstructure modification occurred, the HAZ and the SZ were exposed, both stressed and unstressed, to the alternate immersion cycle. It was found that the Cu/Li ratio played a minor role with respect to the microstructural modification during the SSuBT process; therefore, the focus is on the results for AA 2060 only. In Figure 7-19, high-magnification cross-sectional images of the HAZ and SZ regions are shown that compare a corrosion attack in stressed and unstressed conditions. Similar corrosion features are visible in the SZ sample for both loading conditions. What is seen as a pit at low magnification reveals to be intergranular corrosion and cracking. Because of the small, round grain morphology, grain boundary dissolution appears around the grains. As a consequence, the grains are released from the material and the pit grows. This mechanism is known as intergranular corrosion (IGC). Small differences in the corrosion propagation mechanisms occurred when the material was stressed. During the testing, pits in the stressed coupons formed more frequently and grew to a larger depth in the direction normal to the applied stress. These large cracks indicate a higher susceptibility provoked by the stress. Figure 7-19 b) shows a very pronounced case of attack, which then develops as a stress corrosion crack (SCC).

For the HAZ, the unstressed condition developed similarly to the selective grain dissolution observed for the BM material (see Chapter 7.3.1), while the stressed condition showed a grain boundary attack, indicating SCC. The corrosion attack appeared to propagate along the grain boundaries, leaving intergranular channels behind, which appear similar to deep cracks. The cracking structure was initiated from small pits or at grain boundaries on the surface. This mechanism indicates an anodic metal dissolution accelerated by stress, known as SCC. Phases in the grain boundaries containing an increased Cu content and thus acting cathodically might lead to an anodic behavior of the surrounding regions and are thus prone to first dissolution. The dissolution process propagated along the grain and subgrain boundaries. The loading was applied in the transverse long (T_L) direction, indicated in Figure 7-19 d).

This direction yields an enlarged grain boundary density and is therefore susceptible to SCC. In this study, the grain morphology led to an increased number of grain boundaries perpendicular to the stress axis facilitating growth, as the propagation rate was determined by crossing boundaries that are not parallel to the stress axis [141].

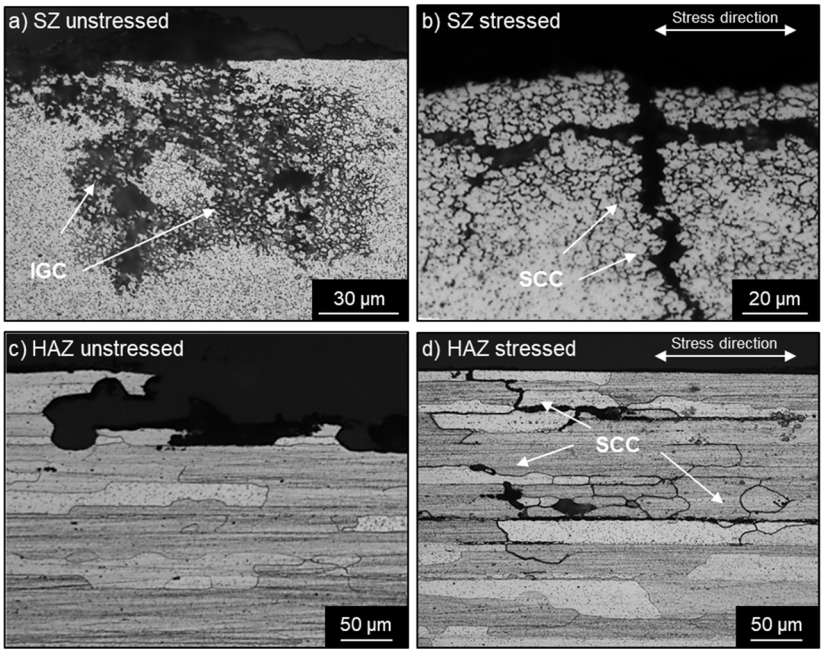

Figure 7-19 Detailed view of the corrosion attack for SZ unstressed a) and stressed b), HAZ unstressed c) and stressed d) exposure in AA 2060. The loaded condition promoted intergranular cracking in both zones.

7.4 Summary

Corrosion mechanisms reported in current studies for aluminum alloys [126,127,130,142] were observed by immersion testing in both alloys in all welding zones. A localized corrosion process occurred, where the initial corrosion spots were intermetallic particles enriched with copper, iron, manganese, silver or nickel that acted as a cathode with respect to the aluminum matrix. After the initial matrix dissolution around the intermetallic particles, pits started to develop, confirmed by the formation of corrosion rings around the pit. This behavior is known as localized corrosion (pitting corrosion). The pits propagated preferably on crystallographic imperfections in the HAZ and the BM. In the SZ, the pit grew with no preferred orientation because of the symmetric grain morphology. Electrochemical analysis showed that AA 2196 features lower corrosion resistance because of a higher lithium and lower copper content.

Regarding the different welding zones, both alloys showed increased corrosion resistance in the SZ, assumed to be caused by the absence of large intermetallic particles.

The stress-enhanced corrosion behavior of the as-received and welded material was investigated by a number of tests. BM samples of both alloys were exposed to the standardized procedure. Samples of AA 2060 revealed a corrosion mechanism known as selective grain dissolution, previously reported for Al-Cu-Li alloys [139]. For AA 2196, exfoliation at these attack spots was additionally observed. The susceptibility of the grains depends highly on the orientation, as shown by Ma et al. [130], who correlated the Schmid factor with the corrosion resistance. Because certain grains are more prone to anodic dissolution, they are attacked first, leading to an overall appearance of localized grain dissolution. The mechanism remained the same independent of the applied stress. Differences were noticed when the residual ductility was determined. While the residual strength did not significantly change, the elongation at failure was decreased by 26 % and 63 % for AA 2060 and AA 2196, respectively. The decrease in ductility is assumed to be related hydrogen uptake. Subsequent embrittlement also showing exfoliation characteristics develops in AA 2196 to a larger extent because of the high aspect ratio grains owing to the extruded grain morphology.

The welded specimens showed a different behavior. As the entire weldment was subjected to the testing procedure, a slight drop of the residual strength appeared. The UTS dropped by approximately 10 % (9 % for AA 2060 and 10 % for AA 2196) when the welds were exposed to the testing cycle and 20 % (18 % for AA 2060 and 23 % for AA 2196) when the welds were exposed to the testing cycle under load. This implies that both the exposure to 3.5 % NaCl solution as well as the applied stress of 75 % of YS leads to corrosion attacks that are significant with respect to the mechanical performance of the weld. Because the samples were tested in their as-welded condition, the applied load was calculated according to the mechanical properties of the weld. As seen in Chapter 6.4, the mechanical properties of the weld reflect the local properties of the weakest area which is the HAZ, near the TMAZ/SZ transition. Consequently, only this zone was loaded to 75 % of the YS during the SCC testing procedure. The final fracture at post-exposure testing occurred in the SZ/TMAZ transition, initiated on a corrosion pit.

The microstructure of the corroded weld zones was analyzed, revealing that the BM acted as expected, i.e., identical to the BM samples previously tested. However, the zones modified by the welding process revealed a different mechanism showing intergranular corrosion in all loading conditions. In the center of the weld, small, recrystallized grains led to intense grain boundary attack with no preferred orientation, and resulting in partial undercutting and releasing of the grains forming symmetrical pits. The influence of the stress could not be readily seen within the SZ; however, the HAZ showed stress-related corrosion phenomena like cracking. The unstressed HAZ material followed a similar mechanism as seen for the BM, where selected grains were attacked and dissolved completely. After applying stress to the specimen, the grain boundaries were predominantly attacked in the HAZ. Further, the attack propagated along the

grain boundaries until several hundreds of microns into the material, fulfilling all the criteria of SCC. This attack did not lead to a final failure of the structure because certain pits formed in the SZ traveled deeper into the material, decreasing the cross-section and leading to stress concentrations in the residual strength testing.

A detailed view of the microstructure in the SZ and the HAZ revealed that both locations under stressed conditions experienced similar corrosion attacks on the grain boundaries. The different grain morphology led to large pitting cracks in the SZ and to defined crack paths in the HAZ. In this study, grain boundary dissolution probably took place because of its anodic character, which can be accelerated by stress. The propagation rate in the SZ was observed to be higher, and it is assumed to be related to the short and symmetrically connected grain boundary net, which is independent of the stress axis. The grain size and orientation in the HAZ is set during the rolling process and consists of pancake-shaped grains with high aspect ratios. Grain boundaries are longest in the longitudinal direction and the stress axis during the SCC tests is parallel to the transverse long (T_L) direction. Therefore, it can be assumed that the propagation rate of SCC in the HAZ is slightly hindered, despite the more susceptible microstructure composition. The SSuBT welding process led to severe microstructure modification, which resulted in an increased IGC in the HAZ and the SZ. Both zones showed susceptibility for IGC and SCC. As the SZ did not feature the lowest strength, the relative stress is not as critical as in the HAZ. However, the HAZ might have been protected by the grain morphology, which could decrease the SCC propagation rate.

8 Discussion

The aim of this chapter is to discuss the main process characteristics, as shown in Chapter 5, the microstructural evolution shown in Chapter 6 and the corrosion response presented in Chapter 7. In the scope of an interdisciplinary analysis, the origins of the resulting corrosion are explored. Therefore, two areas are further discussed in detail. The first subchapter gives an insight into the short-timed thermal impact that is typically experienced by friction welded materials. Known microstructure evolution models are used to address the process data. As common microstructural investigations focus on medium to long timed thermal impact, the knowledge was transferred to the findings for short-timed impact in the range of a few seconds, as found during BT-FSW.

The second section addresses the corrosion phenomena found during the testing under applied stress. As the results of the corrosion testing depends on the history of the material, it is unavoidable to take the microstructural evolution and the processing into consideration. Intergranular SCC found in the processed alloys of interest is therefore linked to the microstructure modification during the short-timed thermal impact.

8.1 Microstructure evolution during the short-timed thermal impact in Al-Cu-Li alloys

Both base metals investigated in this study were delivered in T8 temper, which means cold working after solution heat treatment was conducted intending to raise the dislocation density prior to artificial aging. For Al-Cu-Li alloys, dislocation sites are preferred nucleation spots for T1 precipitates, which are the preferred strengthening precipitates in the third generation of this alloy family. In this work, two alloys with differing Cu/Li ratios were used to explore the mechanisms working by transient thermo-mechanical processing such as in FSW. To understand the microstructural state, analyses have been conducted prior to and after welding. Material samples have been analyzed during simulated heating events to investigate the general precipitation sequence, which remains controversial in the state-of-art literature. While AA 2196 was introduced in 2000, AA 2060 has only been patented since 2011. Consequently, the microstructure state and especially the phenomena during transient processing, have not been so far studied in depth in the literature.

In Chapter 6.1, the characteristics of the initial microstructure state were determined. During the welding process, the initial microstructure was subjected to severe thermo-mechanical processing. The welding forces were analyzed in Chapter 5.2, showing the highest forces in the welding direction of approximately 6 kN at a rotational speed of 150 RPM with a gap force of 5.5 kN, which causes an internal pressure of approximately 34 MPa (340 bar). These conditions lead to high shear rates within the SZ. The high shear rate transforms intermetallic particles into smaller dimensions within the SZ [119] and create a high

density of nucleation sites. Additionally, the high deformation energy resulted in major recrystallization within the SZ, which in turn led to a reduction in dislocation density [143]. Although a precise estimation of the strain rate remains difficult, it was shown to be highest within the SZ, resulting in a fine, recrystallized grain structure.

While the changes in grain size (grain boundary density) and dislocation density influence the initial nucleation of precipitates, the thermal impact during the process has a major impact on the dissolution and reprecipitation of precipitates. The thermal cycle during the process is shown in Chapter 5.3 and leads to a maximum measured temperature of 478 °C for AA 2060. Because of the nature of friction stir processes, this temperature is reached within a few seconds, as illustrated by the extremely high heating rate of approximately 35 °K/s.

The microstructures of alloy 2060, with a high Cu/Li ratio, and alloy 2196, with a low Cu/Li ratio, are characterized by the main strengthening precipitate T1. Secondary strengthening precipitates are binary and reflect the higher Cu content in the case of AA 2060, forming Al-Cu phases. Similar effects occur because of the higher Li content in the case of AA 2196 forming Al-Li phases. While both alloys in T8 temper are strengthened by the T1 precipitate, differences are observed when the microstructure is exposed to the process. After welding, the DSC analysis shows that the center of the weld will form more δ' precipitates for AA 2196 (compare Figure 6-12) and that the HAZ consists of more overaged particles, most likely T_2 phases, as shown in Figure 6-13. The AA 2060 is also strengthened by phases such as Al-Cu clusters, θ', and fine δ' particles owing to the high availability of Cu. These phases seem to contribute to the resistance against the heat exposure experienced during the welding process because AA 2060 degrades less than AA 2196 with respect to the mechanical properties.

While the differences are not significant with respect to the strength at the weld center, the location of the lowest hardness, presenting the weakest microstructure, softened considerably more for AA 2196, possibly caused by a higher degree of overaging and less reprecipitation of the strengthening phases. The welding process results in a significant change of the microstructure because the thermal impact initiates a thermally activated metallurgical phenomena. Temperatures were highest in the region of the SZ and decrease as the location moves towards the unaffected base metal.

Two major metallurgical phenomena are present, dissolution and overaging of precipitates followed by post-weld reprecipitation at low temperatures, also referred to as natural aging. Dissolution starts when the solution temperature has been exceeded. Overaging phenomena start at temperatures of approximately 200 °C. The temperature profile over the weld is illustrated in Figure 8-1 c) and the link to the local distribution in the weld zones is shown in Figure 8-1 d). The SZ experiences the highest temperatures leading to almost full dissolution of the primary strengthening precipitate T1. The

surrounding material was exposed to intermediate temperatures; therefore, less dissolution and more overaging reactions occurred. With decreasing distance to the weld center, the ratio of overaging reactions to particle dissolution decreases also.

If the individual metallurgical mechanisms are considered separately, the loss in strength can be estimated. In Figure 8-1 b), the influence of the main strength attributing metallurgical factors over the cross section of the weld is shown. Dissolution of T1 precipitates leads to major strength loss and is found to increase towards the weld center. Overaging also results in strength loss and is found mostly in the HAZ. The overaging reactions increase towards the SZ, before the phases are exposed to temperatures above solute temperature, which will result in dissolution. Natural aging occurs after welding and at ambient temperatures. Strengthening phases, mainly δ', are formed where solute elements are available, leading to an increase of the strength when dissolution reactions are present. This was predominantly observed in the SZ but was also indicated in the HAZ. The last mechanism of reprecipitation during cooling, describes a strength-contributing phase formation during the cooling phase at intermediate temperatures and is assumed in the center of the weld.

The first three primary mechanisms are often reported and are well-accepted in the literature. Reprecipitation during cooling is assumed to raise the strength, as mentioned in several studies [10,115]. Therefore, it is highly likely to occur during SSuBT-FSW. During welding, regions close to the weld center will experience high heating rates to its peak temperature, as shown in Chapter 5.3. Compared to the heating rate, the cooling rate is seven times slower, which means that the material stays longer within certain temperature ranges that allow the activation of precipitations. Reflections of T1 structures were indexed in the SZ and HAZ samples during the HEXRD analysis (see Figure 6-4). Possible reprecipitation suspected by the presence of T1 was also reported in a study by Lin et al. [144] during the FSW of AA 2099 T3. T1 phases were observed in the HAZ/TMAZ, while the higher strength in the SZ was neglected and might contribute to the reprecipitation.

When the previously mentioned metallurgical reactions occurring during the welding process are superimposed to a single factor, the trend of the local strength contribution across the weld is similar to the local hardness distribution exemplary shown for AA 2060 in Figure 8-1 a). The lowest hardness reflects the location where the ratio of all metallurgical mechanisms are the most unfavorable. If these individual mechanisms are quantified, a precise prediction of the local and global strength can be made according to the given thermal data, which can lead to temperature-controlled optimization.

High-strength alloys of the Al-Cu-Li system are designed to be property-specific by applying the appropriate heat treatment to optimize the microstructure. A typical heat treatment starts with the solution heat treatment for several hours to dissolve existing precipitates prior to quenching and aging. Al-Cu-Li alloys are often referred to as "extremely complex precipitate systems" [10] and the

metallurgical reactions during heat treatment have frequently been researched in recent decades. Nonetheless, in comparison to commercial legacy aluminum alloys, detailed thermodynamic data, such as the time-temperature-precipitation (TTP), the time-temperature-transformation (TTT) or continuous-cooling-diagram (CCD) diagrams are missing in the state-of-the-art literature. A single TTP diagram for AA 2195 exists that was published by Chen and Bhat [123] as a technical report by NASA in 2002.

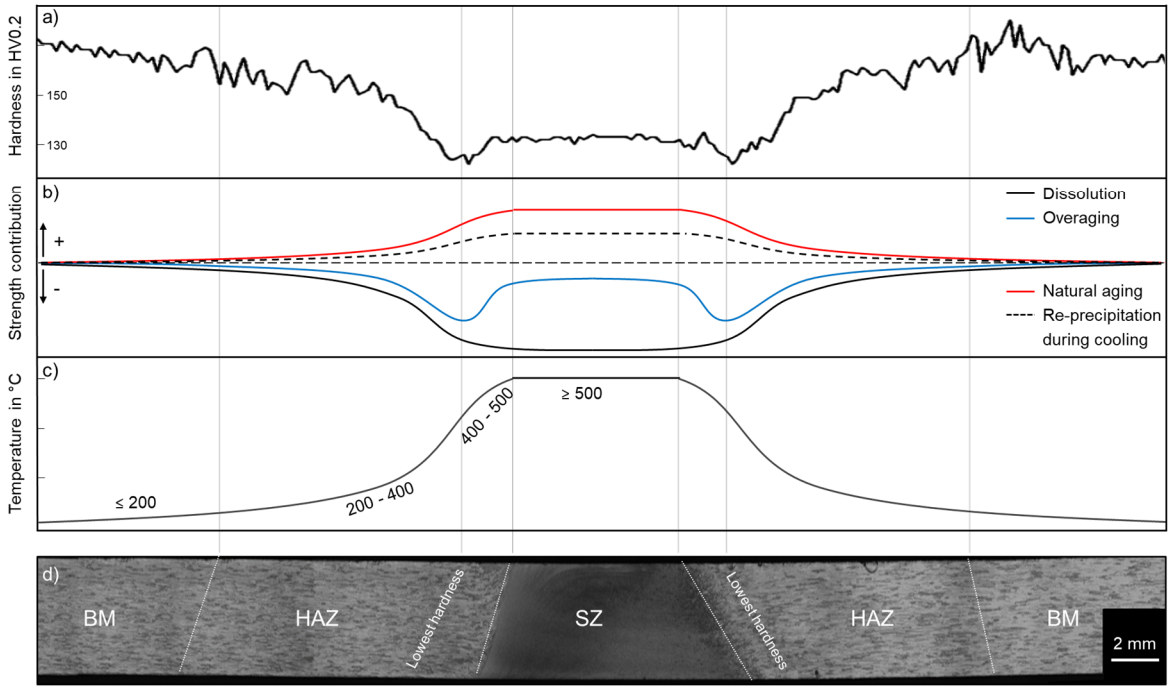

Figure 8-1 Hardness distribution a), strength contribution profile b) and schematic temperature profile c) over the cross-section of a typical SSuBT-FSW weld in Al-Cu-Li alloys d). Transient temperatures experienced in the HAZ lead to the most unfavorable microstructure resulting in lowest hardness.

With respect to processing, a thermal heating event such as FSW can be seen as a transient local heat treatment because the metallurgical changes are defining the mechanical outcome. For this case, the only available TTP diagram is not suitable because the heating and cooling rates and the holding times are much smaller than those considered in a conventional TTP diagram, which considers the equilibrium state. In Figure 8-2, the TTP diagram by Chen and Bhat [123] is extended to the processing times of friction welding, and an SSuBT-FSW cooling curve is added. The cooling curve is taken at 3.8 mm from the SZ center of AA 2060 material (see Chapter 5.3) which is, assuming homogeneous heat distribution within the SZ, thought to be close to the hottest spot in the weld. Even though the transformation curves are constructed on the basis of equilibrium state data and the cooling curve transforms dynamically in

this diagram, the TTP diagram does not cover short interval heat exposures. However, phases shown to form only after long exposure to high temperatures, such as T_2, T_B and θ, are found in the microstructure after being SSuBT-FSW processed.

In Figure 8-2, the transformation curves resulting from the microstructure analysis are shown in red. Reprecipitation of the T1 phases is highly likely at holding times of few seconds above the lowest formation temperature of approximately 140 °C and below the dissolution temperature starting at 300 °C. Similarly, the formation of the equilibrium phases T_2 and T_B phases occurs during short intervals of intermediate to high temperatures. Other important transformations, such as the dissolution of T1 particles and overaging, are shown as functions of temperature and time.

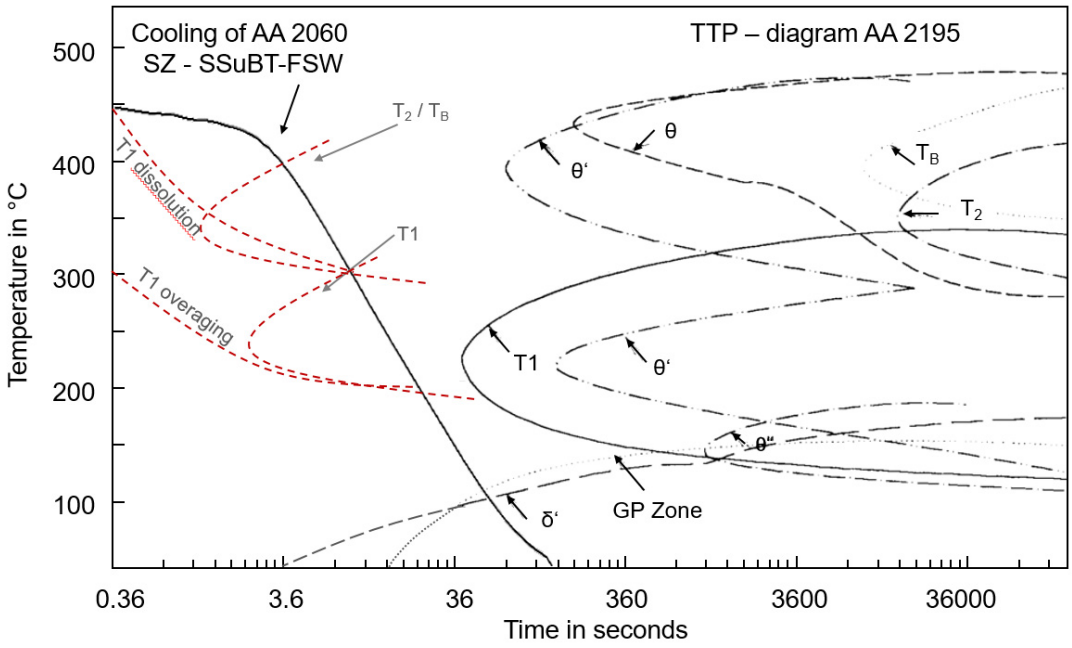

Figure 8-2 Extended TTP diagram with overlaid cooling curve of SSuBT-FSW. Phase transformation predicted by TTP diagrams are observed earlier when subjected to high heating rates as seen in SSuBT-FSW process. Data taken from [123].

Summarizing, a very short interval at maximum temperature is sufficient to dissolve most of the existing precipitates, allowing subsequent reprecipitation during the cooling leg of the thermal cycle in which the formation of T1 phases is possible within a few seconds at high temperatures. The remaining phases that did not dissolve during the peak temperatures are likely to transform to equilibrium phases, which usually involve prior evolved phases and higher temperatures. Conditions found during SSuBT-FSW are fulfilling these requirements because increased amounts of ternary equilibrium phases have been found in the HAZ and the SZ after welding. These phases were identified as T_2 and T_B phases. In addition to crystallographic information [113,145], little is known regarding the formation mechanisms or

temperatures. As the T_2 phase is frequently mentioned in studies investigating its corrosion behavior [136], it appears to have a greater influence on the corrosion than on strength. Further in situ experiments might enable the elaboration of a quantitative representation of the microstructural state during rapid continuous cooling, which can help to predict the exact microstructure composition during non-equilibrium events, similar to friction welding.

8.2 Stress corrosion mechanisms in short-timed thermal impacted microstructures

Intergranular SCC failures are very common in high-strength aluminum alloys containing pancake-shaped grains, typically occurring in rolled plates and extrusions [68]. While coarse precipitates and equilibrium phases in Al-Cu-Li alloys have been observed to gather at grain boundaries, especially in thermomechanical-modified regions [37,146,147], only a few investigations exist that treat the stress corrosion behavior of FSW welded structures. Hu and Meletis [75] exposed samples of AA 2195 to a 90-day NASA standard cycle and stated that the samples were not susceptible to SCC. No further details on temper, residual strength or corrosion artifacts were provided. Dhondt et al. [20] exposed FSW SZ material of AA 2050 to 1.0 M NaCl solution and found pitting attacks that changed to intergranular SCC when stress was applied. Developing isotropic crack branching were observed similar to what was seen in the present work. While several studies investigate FSW zones by electrochemical techniques, works including stressed samples are rare. With respect to the increasing complexity of application structures, where stress contributions are always present, the systematic investigation of stressed individual specimens as well as component structures is crucial and, currently, is underrepresented in the open literature.

An intergranular corrosion attack was identified when stress was applied during the corrosion analysis. While the BM, which is as-received in T8 temper, is not that much affected by stress influences, process-modified microstructures found in the different weld zones react differently. This phenomenon has not been reported for welded Al-Cu-Li alloys in the literature. The results were presented in Chapter 7.3; the connection to the underlying microstructural features are addressed in this section.

The zones modified by the short-timed thermal impact revealed a different corrosion mechanism, as illustrated in the pristine BM material (see Chapter 7.3.1). In the SZ, small, recrystallized grains lead to an intense grain boundary attack with no preferred orientation, resulting in partial undercutting and releasing of the grains forming symmetrical pits. The HAZ sample revealed attacked grain boundaries leading to deep cracks.

Microstructural investigations of the SZ and the HAZ showed that under stressed conditions, both zones experienced similar corrosion attacks on the grain boundaries. The different grain morphology led to

large pitting cracks in the SZ and to defined crack paths in the HAZ. The propagation rate in the SZ is expected to be higher because of the short and symmetrically connected grain boundary net, which is independent of the stress axis and only present in the SZ. For the HAZ, the propagation rate of the SCC is slightly hindered despite the susceptible microstructural state which was addressed in the previous Chapter 8.1. The short-timed thermal impact led to severe microstructure modifications, resulting in an increased IGC in the HAZ and the SZ.

As confirmed by the preferred corrosion sites, the modified microstructures in the SZ and in the HAZ play an important role for the corrosion mechanism. Within this region, grain boundary attack was observed as a key mechanism. The grain boundaries changed during the welding from the thermal impact and the introduced deformation, as discussed in Chapter 6.2. While grain boundaries are not preferred nucleation sites for coarse phases in the BM, this behavior was seen in the analysis of the SZ and the HAZ (see Figure 6-8 and Figure 6-10 respectively). Coarse precipitates accumulate at the grain boundaries, increasing the inhomogeneity of the composition. Following the literature [103,112,148] and the microstructure analysis shown in Chapter 6.2, these coarse phases were assumed to be T_2 and T_B phases with a minor contribution from the Ω phase. EDS data showed a highly increased copper content, with other elements such as manganese on the coarse grain boundary precipitates (GBP). Summarizing, the grain boundaries in the thermally modified microstructures consist of coarse equilibrium phases which are of high copper content. This results in a precipitation-depleted region surrounding the GBP and grain boundaries [66]. The overall grain boundary composition indicates a noble character with respect to the surrounding region, thus posing a potential difference.

In Chapter 7.3, the degradation of the microstructure modified zones from a stress-instigated corrosion attack was discussed. First, SCC occurred in stressed SZ and HAZ regions of both alloys and second, IGC occurred in the unstressed SZ specimens. These findings are explored in detail.

SCC in stressed HAZ and SZ

The microstructure evolution is the answer to the first issue. Al-Cu-Li alloys are known to accumulate precipitates at grain boundaries [66]. The experienced thermal cycle leads to severe changes that have been previously shown to cause an increased GBP density. Particles precipitated at the grain boundaries contribute to a potential difference between the GBP and the surrounding matrix promoting intergranular SCC from the anodic dissolution mechanism reported for aluminum alloys in chloride environments [66,71]. Resulting corrosion attacks on samples of AA 2060 in stressed conditions are compiled in Figure 8-3. Figure 8-3 a) and d) contain images taken in the cross-sectional view, showing grain-boundary or near-grain-boundary dissolution leading to net-like attack propagation in the HAZ a) and in the SZ d). Figure 8-3 b) and e) confirm the intergranular nature observed on the fracture surface

after exposure and Figure 8-3 c) and f) show the GBP seen by STEM imaging. The two regions show similar mechanisms. Because the propagation path for the intergranular corrosion is strictly grain-morphology dependent, its appearance different from the others.

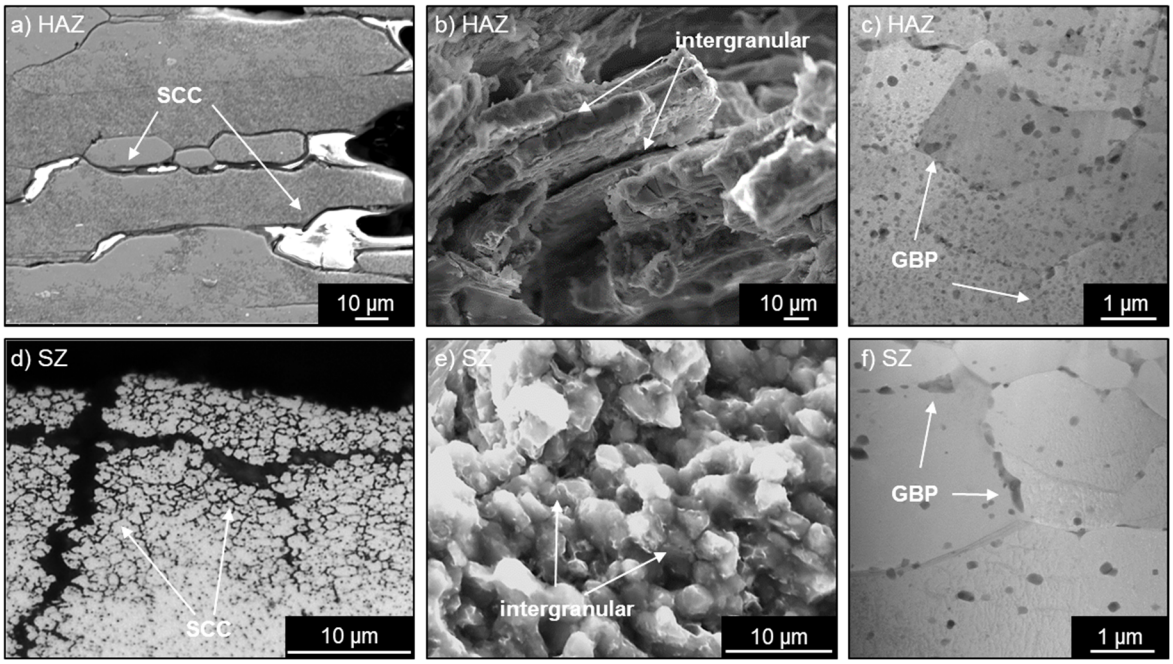

Figure 8-3 Details after SCC testing for AA 2060 in HAZ a)-c) and SZ d)-f). a) and d) show microstructures images of the SCC affected areas, b) and e) confirm the intergranular attack on the fracture surface, d) and f) show GBP in the modified microstructure after welding in STEM images.

While the SZ is characterized by small, equiaxed grains, the HAZ remains in the rolled grain structure, as described in Chapter 6.2. Nonetheless, both regions experience an attack at grain boundaries and further propagation along the grain boundary structure. Therefore, the intergranular corrosion accelerated by stress is SCC. Figure 8-3 b) emphasizes the grain boundary dissolution resulting in intergranular fracture. During the final fracture, the pancake structure in the HAZ tends to inhibit the crack propagation, thus leading to a partly transgranular fracture.

IGC in the SZ in the unstressed condition

In Figure 7-19, the stress dependency of the modified microstructure is shown. While the HAZ indicated a clear acceleration of the corrosion under stress, the SZ maintained similar IGC fissures opening up to large cracks. Stress is commonly seen as a corrosion promoter because the energy is increased and above the Peierls stress dislocation motion, it can lead to rupture of the lattice, exposing bare metal to the

corrosive environment. However, the grain morphology is important and very different in the SZ and the HAZ. Several factors lead to a lower SCC resistance in recrystallized microstructures found in the SZ region. Recrystallization involves the nucleation and growth of nearly defect-free grains by the motion of high-angle grain boundaries [149]. The increased fraction of high-angle grain boundaries in the SZ is unfavorable with respect to the SCC resistance [150,151]. Additionally, recrystallized microstructure was found, in general, to be prone to SCC. Kannan and Raja [66,152] investigated the influence of recrystallized grains on the SCC behavior in AA 7010 and found these grains to be more susceptible to SCC in chloride solutions. Further, SCC propagation is highly dependent on the orientation of the applied stress. Textured metals such as rolled or extruded aluminum show the highest susceptibility when the stress is applied in the transverse short (T_S) direction. Here, more grain boundaries are aligned fairly planar and normal to the stress axis offering the preferred crack path. When stress is applied in the transverse long (T_L) or longitudinal (L) direction, the grain morphology hinders facile crack propagation. In the case of the HAZ, the stress was applied parallel to the transverse long direction, making it almost impossible to propagate intergranular cracks without additional energy as for example externally applied loading. In Figure 8-4 this situation is illustrated. The crack in Figure 8-4 c), the HAZ, propagates along high and low stressed GB while the crack in Figure 8-4 d), the SZ, mostly propagates along high stressed GB. Therefore, more activation energy is needed to propagate an intergranular crack in the HAZ than in the SZ.

Summarizing, the recrystallized, small-grain microstructure in the SZ presents a generally more susceptible grain morphology from an increased grain boundary density as well as an isotropic orientation. The smallest contributions of residual stress resulting from the thermomechanical impact might be enough to promote IGC to propagate into the grain boundary network. Consequently, even in unstressed testing conditions, SCC-like phenomena are present in the SZ while these appear only under applied stress in the HAZ.

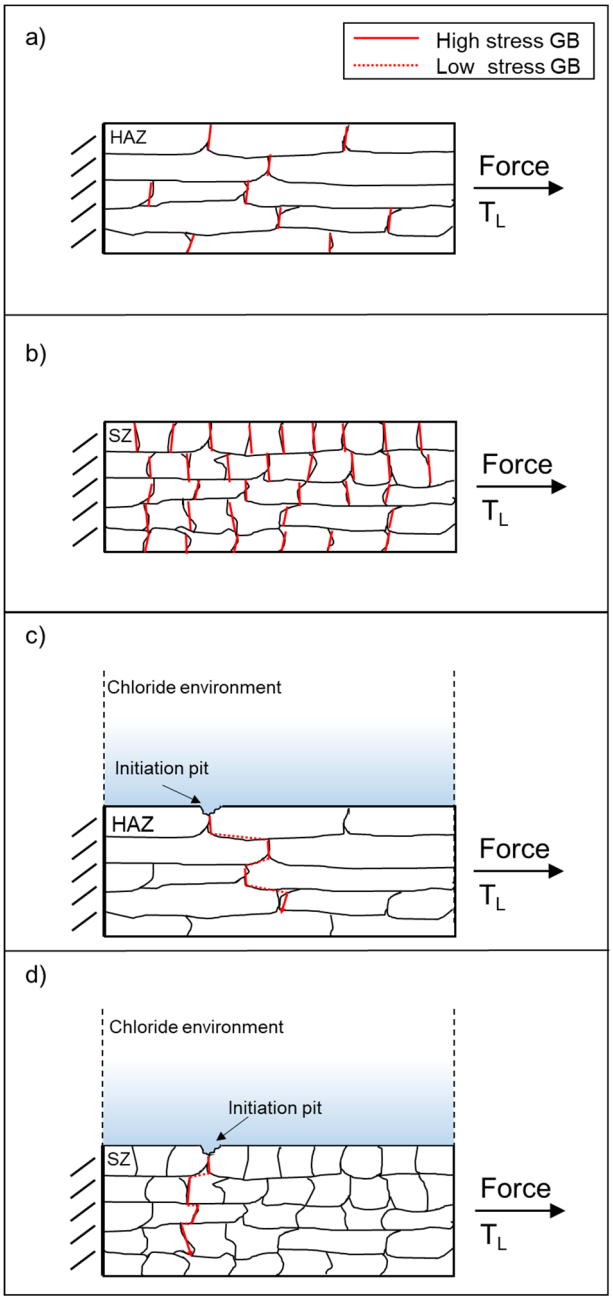

Figure 8-4 Phenomenological model illustrating energy levels on GB before SCC attack (a and b) and the possible crack paths during SCC attack (c and d).

9 Conclusions

Employing SSuBT-FSW, a process methodology to weld modern Al-Cu-Li alloys was developed. The consequences with respect to the mechanical properties as well as the corrosion and stress corrosion behavior have been explored in detail. As a cross-link, a fundamental microstructure analysis could reveal unpublished details on the microstructure evolution during FSW processes. The rarely treated link to an extensive stress corrosion analysis could show the origins of the intergranular phenomena that have not been previously reported. This work helps to decode the highly complex microstructure system of modern Al-Cu-Li alloys, which have been researched for many decades. In accordance to the objectives, the following conclusions can be drawn:

- Process development of SSuBT-FSW led to the successful production of defect-free welds at identical process parameters for AA 2060 T8 and AA 2196 T8.
- Temperature cycle analysis exhibited maximum temperatures of 478 °C within the SZ for AA 2060. Slightly higher temperatures are generated in alloy 2196, although the total torque was smaller, which is attributed to the materials behavior under high temperatures.
- Higher strain rates on the AS lead to increasing grain size from AS to RS in the SZ during the process for both alloys. A high Cu/Li ratio in AA 2060 leads to the formation of smaller grains.
- The different Cu/Li ratios caused a different precipitation sequence in the base material. A low Cu/Li ratio favors the precipitation of δ' and retards the nucleation of T1, while a high Cu/Li ratio is strengthened by clustering and by early-formed, fine T1 precipitation.
- The precipitation sequence of Al-Cu-Li has been revised and is proposed as follows:

$$\alpha\ (SSSS) \rightarrow GP\ zones + \delta' \rightarrow T_1 + \delta + \theta' \rightarrow T_B + T_2 + \theta$$

- Temperatures of up to 480 °C during welding led to large-scale dissolution of the T1 precipitate and the consequent softening of both materials. Reprecipitation of the T1 phase during the cooling phase is assumed by the later presence in the SZ area.
- Equilibrium phases such as T_2 and T_B have evolved from previous phases during the welding process and are still present after welding. These phases are preferably located at grain boundaries and were found in the SZ and HAZ.
- The microstructure leading to the highest degradation of mechanical properties was found in the HAZ at 6-7 mm from the weld center, and experiences peak temperatures of approximately 400 °C. A low Cu/Li ratio for AA 2196 softened 9 % more than AA 2060 from a higher dissolution of T1 phases. The high-Cu/Li alloy AA 2060 shows a higher thermal stability and exhibits a more robust microstructure represented by a lower loss of functionality of the strengthening precipitate T1

during the welding process. The thermal impact of the welding process led to coarsening and dissolution reactions in the HAZ in both alloys.

- The general corrosion behavior was determined and indicated localized corrosion. The initial corrosion sites are the noble-element enriched particles acting as a cathode with respect to the Al matrix. Later, the localized corrosion attack evolves to pitting, forming corrosion rings and propagating preferentially on crystallographic defects.
- When samples are exposed to a corrosive environment under stress, enhanced IGC is observed in the HAZ and SZ.
- Anodic dissolution is provoked by high-copper equilibrium phases at the adjacent region in the HAZ and the SZ. The growth propagation along the GB leads to intergranular appearance and cracking.
- SCC initiation was found developing from pits in the HAZ. Due to the local mechanical property distribution, no sample failed during the 30-day exposure.

This work emphasizes the importance of interdisciplinary analysis when changes are applied to materials and processes. The application of Al-Cu-Li in spacecraft propellant tanks using SSuBT-FSW leads to degradation in mechanical and corrosion properties. Applying fundamental knowledge of the microstructural state caused by transient thermal impacts, the resulting properties can be balanced to fulfill service needs.

References

[1] NASA Orbital Debris Program, Orbital Debris Program Office, Houston, USA, 2011.

[2] D. Alwes, U. Wirt, Weltraummüll, DLR-Nachrichten. 111 (2005) 28–33.

[3] W.M.B. Peter, Spacecraft Design-for-Demise Strategy , Analysis and Impact on Low Earth Orbit Space Missions, M.Sc. Thesis, Massachusetts Institute of Technology, 2009. http://hdl.handle.net/1721.1/46797.

[4] U.S. Government, Mitigation Standard Practices, in: Orbital Debris Mitig. Stand. Pract., 1997.

[5] R.L. Kelley, N.L. Johnson, Evaluating and Addressing Potential Hazards of Fuel Tanks Surviving Atmospheric Reentry, in: Proc. 5th IAASS Conf. A Safer Sp. Safer World, Versailles; France, 2011. http://hdl.handle.net/2060/20110008637.

[6] C. Giummarra, B. Thomas, R. Rioja, New Aluminum alloys for aerospace applications, in: Proc. 3rd Light Met. Technol. Conf., Québec, Canada, 2007.

[7] R. Bellarosa, G. Milbourn, D. Catherall, A. Norman, D. Andrews, K. Nor, A. Robelou, A. Defence, G.W. Road, Replacing titanium for the manufacturing of demiseable propellant tanks. Investigation of Al-Lithium and its welding optimization, in: Sp. Propuls., Rome, Italy, 2016.

[8] Webpage, Hydrazine Propellant Tanks for Satellites and Spacecraft. http://www.space-propulsion.com (accessed September 27, 2018).

[9] R.S. Mishra, Z.Y. Ma, Friction stir welding and processing, Mater. Sci. Eng. R Reports. 50 (2005) 1–78. doi:10.1016/j.mser.2005.07.001.

[10] R.S. Mishra, H. Sidhar, Friction stir welding of 2xxx aluminum alloys including Al-Li alloys, Butterworth-Heinemann, 2017. doi:10.1016/C2015-0-04519-1.

[11] R.J.H. Wanhill, R.T. Byrnes, C.L. Smith, Stress corrosion cracking in aerospace vehicles, NLR-TP-2010-538, 2010.

[12] D. Lohwasser, Z. Chen, Introduction, in: Frict. Stir Weld., Woodhead Publishing, 2009: pp. 1–12. doi:10.1533/9781845697716.1.

[13] J. Hilgert, Knowledge Based Process Development of Bobbin Tool Friction Stir Welding, Ph.D. thesis, TU Hamburg Harburg, 2012. doi:10.15480/882.1069.

[14] P. Scupin, Semi-Stationary Shoulder Bobbin Tool (S3BT): A New Approach in High Speed Friction Stir Welding, Ph.D. thesis, TU Hamburg Harburg, 2015. doi:10.15480/882.1325.

[15] M. Skinner, R.L. Edwards, Improvements to the FSW Process Using the Self-Reacting Technology, Mater. Sci. Forum. 426–432 (2003) 2849–2854.

[16] J.A. Schneider, A.C. Nunes, M.S. Brendel, The Influence of Friction Stir Weld Tool Form and Welding Parameters on Weld Structure and Properties: Nugget Bulge in Self-Reacting Friction Stir Welds, in: 8th Int. Symp. Frict. Stir Weld., Timmendorfer Strand, Germany, 2010.

[17] F.F. Wang, W.Y. Li, J. Shen, S.Y. Hu, J.F. dos Santos, Effect of tool rotational speed on the microstructure and mechanical properties of bobbin tool friction stir welding of Al–Li alloy, Mater. Des. 86 (2015) 933–940. doi:10.1016/j.matdes.2015.07.096.

[18] J. Shen, F. Wang, U.F.H. Suhuddin, S. Hu, W. Li, J.F. dos Santos, Crystallographic Texture in Bobbin Tool Friction-Stir-Welded Aluminum, Metall. Mater. Trans. A. 46 (2015) 2809–2813. doi:10.1007/s11661-015-2948-7.

[19] J. Goebel, M. Reimann, A. Norman, J.F. dos Santos, Semi-stationary shoulder bobbin tool friction stir welding of AA2198-T851, J. Mater. Process. Technol. 245 (2017) 37–45. doi:10.1016/j.jmatprotec.2017.02.011.

[20] M. Dhondt, I. Aubert, N. Saintier, J.M. Olive, Effects of microstructure and local mechanical fields on intergranular stress corrosion cracking of a friction stir welded aluminum-copper-lithium 2050 nugget, Corros. Sci. 86 (2014) 123–130. doi:10.1016/j.corsci.2014.05.001.

[21] E. Bousquet, A. Poulon-Quintin, M. Puiggali, O. Devos, M. Touzet, Relationship between microstructure, microhardness and corrosion sensitivity of an AA 2024-T3 friction stir welded joint, Corros. Sci. 53 (2011) 3026–3034. doi:10.1016/J.CORSCI.2011.05.049.

[22] B. Cai, Z.Q. Zheng, D.Q. He, S.C. Li, H.P. Li, Friction stir weld of 2060 Al–Cu–Li alloy: Microstructure and mechanical properties, J. Alloys Compd. 649 (2015) 19–27. doi:10.1016/j.jallcom.2015.02.124.

[23] Y. Mao, L. Ke, F. Liu, C. Huang, C. Y., L. Q., Effect of welding parameters on microstructure and mechanical properties of friction stir welded joints of 2060 aluminum lithium alloy, Int. J. Adv. Manuf. Technol. 81 (2015) 1419–1431. doi:10.1007/s00170-015-7191-2.

[24] B. Decreus, A. Deschamps, F. De Geuser, P. Donnadieu, C. Sigli, M. Weyland, The influence of Cu/Li ratio on precipitation in Al–Cu–Li–x alloys, Acta Mater. 61 (2013) 2207–2218. doi:10.1016/j.actamat.2012.12.041.

[25] N. Birbilis, T.H. Muster, R.G. Buchheit, Corrosion of Aluminum Alloys, in: Corros. Mech. Theory Pract., CRC Press, 2011: pp. 705–736.

[26] I.M. LeBaron, Aluminum alloy, U.S. Patent No. 2.381.219, 1945.

[27] J.M. Silcock, T.J. Heal, H.K. Hardy, Structural ageing characteristics of binary aluminium-copper alloys, J. Inst. Met. 82 (1954) 239–248.

[28] R.J.H. Wanhill, G.H. Bray, Aerostructural Design and Its Application to Aluminum-Lithium Alloys, in: Aluminum-Lithium Alloy., Elsevier Inc., 2014: pp. 27–58. doi:10.1016/B978-0-12-401698-9.00002-1.

[29] R.J. Rioja, J. Liu, The evolution of Al-Li base products for aerospace and space applications, Metall. Mater. Trans. A Phys. Metall. Mater. Sci. 43 (2012) 3325–3337. doi:10.1007/s11661-012-1155-z.

[30] E. a Starke, Historical Development and Present Status of Aluminium-Lithium Alloys, in: Alum. Alloy., Elsevier Inc., 2014: pp. 3–26. doi:10.1016/B978-0-12-401698-9.00001-X.

[31] NASA, Super Lightweight External Tank, NASA Facts. (2005).

[32] R.J.H. Wanhill, Aerospace Applications of Aluminum-Lithium Alloys, in: Aluminum-Lithium Alloy., Elsevier Inc., 2014: pp. 503–535. doi:10.1016/B978-0-12-401698-9.00015-X.

[33] M. Niedzinski, C. Thompson, Airware 2198 Backbone of the Falcon Family of SpaceX Launchers, Light Met. Age. 68 (2010) 6–7.

[34] H. Sidhar, R.S. Mishra, Aging kinetics of friction stir welded Al-Cu-Li-Mg-Ag and Al-Cu-Li-Mg alloys, Mater. Des. 110 (2016) 60–71. doi:10.1016/j.matdes.2016.07.126.

[35] J. Entringer, M. Reimann, A. Norman, J.F. dos Santos, Influence of Cu/Li ratio on the microstructure evolution of bobbin-tool friction stir welded Al-Cu-Li alloys, J. Mater. Res. Technol. (2019) in press.

[36] K.S. Kumar, S.A. Brown, J.R. Pickens, Microstructural evolution during aging of an Al-Cu-Li-Ag-Mg-Zr alloy, Acta Mater. 44 (1996) 1899–1915. doi:10.1016/1359-6454(95)00319-3.

[37] S.C. Wang, M.J. Starink, Precipitates and intermetallic phases in precipitation hardening Al–Cu–Mg–(Li) based alloys, Int. Mater. Rev. 50 (2005) 193–215. doi:10.1179/174328005X14357.

[38] H.-H. Jo, K. Hirano, Precipitation processes in Al-Cu-Li alloy studied by DSC, Mater. Sci. Forum. 13–14 (1987) 377–382. doi:10.4028/www.scientific.net/MSF.13-14.377.

[39] J. A. Schneider, A. C. Nunes Jr., P. S. Chen, G. Steele, TEM study of the FSW nugget in AA2195-T81, J. Mater. Sci. 40 (2005) 4341–4345. doi:10.1007/s10853-005-2808-8.

[40] I.J. Polmear, R.J. Chester, Abnormal age hardening in an Al-Cu-Mg alloy containing silver and lithium, Scr. Metall. 23 (1989) 1213–1217. doi:10.1016/0036-9748(89)90329-3.

[41] W.M. Thomas, E.D. Nicholas, J.C. Needham, M.G. Murch, P. Templesmith, C.J. Dawes, Friction Stir welding, GB Patent 9125978.8, 1991.

[42] R. Nandan, T. DebRoy, H.K.D.H. Bhadeshia, Recent advances in friction-stir welding – Process, weldment structure and properties, Prog. Mater. Sci. 53 (2008) 980–1023. doi:10.1016/j.pmatsci.2008.05.001.

[43] J.-Q. Su, T.. Nelson, R. Mishra, M. Mahoney, Microstructural investigation of friction stir welded 7050-T651 aluminium, Acta Mater. 51 (2003) 713–729. doi:10.1016/S1359-6454(02)00449-4.

[44] W.M. Thomas, K.I. Johnson, C.S. Wiesner, Friction Stir Welding - Recent development in Tool and Process Technologies, Adv. Eng. Mater. 5 (2003) 485–490. doi:10.1002/adem.200300355.

[45] P.L. Threadgill, A.J. Leonard, H.R. Shercliff, P.J. Withers, Friction stir welding of aluminium alloys, Int. Mater. Rev. 54 (2009) 49–93. doi:10.1179/174328009X411136.

[46] G. Çam, S. Mistikoglu, Recent developments in friction stir welding of Al-Alloys, J. Mater. Eng. Perform. 23 (2014) 1936–1953. doi:10.1007/s11665-014-0968-x.

[47] M.J. Russell, C. Blignault, N.L. Horrex, C.S. Wiesner, Recent Developments in the Friction Stir Welding of Titanium Alloys, Weld. World. 52 (2013) 12–15. doi:10.1007/BF03266662.

[48] J.-Q. Su, T.. Nelson, R. Mishra, M. Mahoney, Microstructural investigation of friction stir welded 7050-T651 aluminium, Acta Mater. 51 (2003) 713–729. doi:10.1016/S1359-6454(02)00449-4.

[49] S. Sheikhi, R. Zettler, J.F. dos Santos, Fortschritte beim Rührreibschweißen von Aluminium, Magnesium und Stahl, Materwiss. Werksttech. 37 (2006) 762–767. doi:10.1002/mawe.200600060.

[50] R.J. Ding, P.A. Oelgoetz, Auto Adjustable Pin Tool for Friction Stir Welding, U.S Patent 6.173.880, 1999.

[51] R.L. Edwards, Recent Advances in Welding of Aluminum Alloys Using a Self Reacting Pin Tool (SRPT) Approach with Application Examples, in: Proc. 7th Int. Conf. Trends Weld. Res., Pine Mountain, Georgia, USA, 2005: p. 9.

[52] E.N.C. Dalder, J.W. Pastrnak, J. Engel, R.S. Forrest, E. Kokko, K. Mc Ternan, D. Waldron, E. Dalder, Bobbin-Tool Friction-Stir Welding of Thick-Walled Aluminum Alloy Pressure Vessels, Weld. J. 87 (2008) 40–44.

[53] T.P. Neumann, Friction stir welding of Al 2024-T351 using a self-reacting bobbin tool, Ph.D. thesis, Technische Universität Ilmenau, 2009.

[54] P.L. Threadgill, M.M.Z. Ahmed, J.P. Martin, J.G. Perrett, B.P. Wynne, The Use of Bobbin Tools for Friction Stir Welding of Aluminium Alloys, Mater. Sci. Forum. 638–642 (2010) 1179–1184. doi:10.4028/www.scientific.net/MSF.638-642.1179.

[55] W.Y. Li, T. Fu, L. Hütsch, J. Hilgert, F.F. Wang, J.F. dos Santos, N. Huber, Effects of tool rotational and welding speed on microstructure and mechanical properties of bobbin-tool friction-stir welded Mg AZ31, Mater. Des. 64 (2014) 714–720. doi:10.1016/j.matdes.2014.07.023.

[56] L. Zhou, G.H. Li, G.D. Zha, F.Y. Shu, H.J. Liu, J.C. Feng, Effect of rotation speed on microstructure and mechanical properties of bobbin tool friction stir welded AZ61 magnesium alloy, Sci. Technol. Weld. Join. 23 (2018) 596–605. doi:10.1080/13621718.2018.1432098.

[57] W.M. Thomas, C.S. Wiesner, D.J. Marks, D.G. Staines, Conventional and bobbin friction stir welding of 12% chromium alloy steel using composite refractory tool materials, Sci. Technol. Weld. Join. 14 (2009) 247–253. doi:10.1179/136217109X415893.

[58] W.F. Xu, Y.X. Luo, M.W. Fu, Microstructure evolution in the conventional single side and bobbin tool friction stir welding of thick rolled 7085-T7452 aluminum alloy, Mater. Charact. 138 (2018) 48–55. doi:10.1016/J.MATCHAR.2018.01.051.

[59] W. Xu, Y. Luo, W. Zhang, M. Fu, Comparative study on local and global mechanical properties of bobbin tool and conventional friction stir welded 7085-T7452 aluminum thick plate, J. Mater. Sci. Technol. 34 (2018) 173–184. doi:10.1016/J.JMST.2017.05.015.

[60] W.M. Thomas, E.D. Nicholas, E.R. Watts, D.G. Staines, Friction based welding technology for aluminium, Mater. Sci. Forum. 1 (2002) 1543–1548. doi:10.4028/www.scientific.net/MSF.396-402.1543.

[61] K. Okamoto, A. Sato, S.H. Park, S. Hirano, Microstructure and Mechanical Properties of FSWed Aluminum Extrusion with Bobbin Tools, Mater. Sci. Forum. 706–709 (2012) 990–995. doi:10.4028/www.scientific.net/MSF.706-709.990.

[62] C.A. Widener, J.E. Talia, B.M. Tweedy, D.A. Burford, High-Rotational Speed Friction Stir Welding With A Fixed Shoulder, in: 6th Int. Frict. Stir Weld. Symp., Saint Sauveur, Canada, 2006.

[63] J.F. dos Santos, J. Hilgert, Vorrichtung zum Reibrührschweißen, Patent DE102011015831B3, 2012.

[64] J. Goebel, M. Reimann, J.F. dos Santos, Influence of Cu/Li Ratio on the Welding Forces and Mechanical Properties of Two Bobbin Tool Friction Stir Welded Al-Cu-Li Alloys, J. Mater. Eng. Perform. 27 (2018) 5212–5219. doi:10.1007/s11665-018-3551-z.

[65] Z. Ahmad, Principles of corrosion engineering and corrosion control, Butterworth-Heinemann, 2006. ISBN: 9780750659246.

[66] M.B. Kannan, P.B. Srinivasan, V.S. Raja, Stress corrosion cracking (SCC) of aluminium alloys, in: Stress Corros. Crack., Woodhead Publishing Series in Metals and Surface Engineering, 2011: pp. 307–340. doi:10.1533/9780857093769.3.307.

[67] M.B. Kannan, V.S. Raja, R. Raman, A.K. Mukhopadhyay, Influence of Multistep Aging on the Stress Corrosion Cracking Behavior of Aluminum Alloy 7010, Corrosion. 59 (2003) 881–889. doi:10.5006/1.3287709.

[68] M.O. Speidel, Stress corrosion cracking of aluminum alloys, Metall. Trans. A. 6 (1975) 631–651. doi:10.1007/BF02672284.

[69] D.A. Hardwick, A.W. Thompson, I.M. Bernstein, The effect of copper content and heat treatment on the hydrogen embrittlement of 7050-type alloys, Corros. Sci. 28 (1988) 1127–1137. doi:10.1016/0010-938X(88)90123-0.

[70] D. Wang, D.R. Ni, Z.Y. Ma, Effect of pre-strain and two-step aging on microstructure and stress corrosion cracking of 7050 alloy, Mater. Sci. Eng. A. 494 (2008) 360–366. doi:10.1016/j.msea.2008.04.023.

[71] T.D. Burleigh, The Postulated Mechanisms for Stress Corrosion Cracking of Aluminum Alloys: A Review of the Literature 1980-1989, Corrosion. 47 (1991) 89–98. doi:10.5006/1.3585235.

[72] N.J.H. Holroyd, G.M. Scamans, R.C. Newman, A.K. Vasudevan, Corrosion and Stress Corrosion of Aluminum - Lithium Alloys, in: Aluminum-Lithium Alloy., Elsevier Inc., 2014: pp. 457–500. doi:10.1016/B978-0-12-401698-9.00014-8.

[73] B.J. Connolly, J.R. Scully, Transition from Localized Corrosion to Stress Corrosion Cracking in an Al-Li-Cu-Ag Alloy, Corrosion. 61 (2005) 1145–1166. doi:10.5006/1.3278151.

[74] F.D. Wall, G.E. Stoner, The evaluation of the critical electrochemical potentials influencing environmentally assisted cracking of Al-Li-Cu alloys in selected environments, Corros. Sci. 39 (1997) 835–853. doi:10.1016/S0010-938X(97)81154-7.

[75] W. Hu, E.I. Meletis, Corrosion and Environment-Assisted Cracking Behavior of Friction Stir Welded Al 2195 and Al 2219 Alloys, Mater. Sci. Forum. 331–337 (2000) 1683–1688. doi:10.4028/www.scientific.net/MSF.331-337.1683.

[76] W.C. Moshier, B.A. Shaw, W.T. Tack, B. Phull, Stress Corrosion Cracking Behavior of Two High-Strength Al-xCu-Li-Ag-Mg-Zr Alloys, Corrosion. 48 (1992) 306–308. doi:10.5006/1.3315936.

[77] X. Wang, J. Wang, X. Yue, Y. Gao, Effect of aging treatment on the exfoliation corrosion and stress corrosion cracking behaviors of 2195 Al–Li alloy, Mater. Des. 67 (2015) 596–605. doi:10.1016/j.matdes.2014.11.007.

[78] L. Jin-feng, C. Wen-jingP, Z. Xu-shan, R. Wen-dal, Z. Zi-qiao, Corrosion behavior of 2195 and 1420 A1-Li alloys in neutral 3.5% NaCl solution under tensile stress, Trans. Nonferrous Met. SOC. China. 16 (2006) 1171–1177. doi:10.1016/S1003-6326(06)60396-8.

[79] L.S. Kramer, T.P. Blair, S.D. Blough, J.J. Fisher, J.R. Pickens, Stress-Corrosion Cracking Susceptibility of Various Product Forms of Aluminum Alloy 2519, J. Mater. Eng. Perform. 11 (2002) 645–650. doi:10.1361/105994902770343647.

[80] P.B. Srinivasan, K.S. Arora, W. Dietzel, S. Pandey, M.K. Schaper, Characterisation of microstructure, mechanical properties and corrosion behaviour of an AA2219 friction stir weldment, J. Alloys Compd. 492 (2009) 631–637. doi:10.1016/j.jallcom.2009.11.198.

[81] C.S. Paglia, R.G. Buchheit, Microstructure, microchemistry and environmental cracking susceptibility of friction stir welded 2219-T87, Mater. Sci. Eng. A. 429 (2006) 107–114. doi:10.1016/j.msea.2006.05.036.

[82] O. Hatamleh, P.M. Singh, H. Garmestani, Stress Corrosion Cracking Behavior of Peened Friction Stir Welded 2195 Aluminum Alloy Joints, J. Mater. Eng. Perform. 18 (2009) 406–413. doi:10.1007/s11665-008-9303-8.

[83] T. Lips, B. Fritsche, R. Kanzler, T. Schleutker, A. Gülhan, B. Bonvoisin, T. Soares, G. Sinnema, About the demisability of propellant tanks during atmospheric re-entry from LEO, J. Sp. Saf. Eng. 4 (2017) 99–104. doi:10.1016/j.jsse.2017.07.004.

[84] T. Masuda, I. Masuoka, K. Kajiwara, K. Yamada, Demise Characteristics Evaluation for Melting Promotion-Type Tank, J. Propuls. Power. 31 (2015) 981–985. doi:10.2514/1.B35398.

[85] NASA Technical Standard, NASA-STD-5001A, 2008.

[86] M. Perry, Design and Development of the Eurostar Propellant Tank, in: Second Eur. Spacecr. Propuls. Conf., ESA, Noordwijk, The Netherlands, 1997.

[87] David L., SLWT - Risk management case study, NASA Database. (2009).

[88] ESA Standard, ECSS-E-HB-32-20 Part 5A, Sp. Prod. Assur. Qual. Assur. (2011).

[89] Constellium, Constellium to Present New Aerospace Innovations at Paris Air Show, www.constellium.com.

[90] NASA, ORION - America's next generation spacecraft, 2010. www.nasa.gov.

[91] J. Merino, A. Patzelt, A. Steinacher, M. Windisch, G. Heinrich, R. Forster, C. Bauer, ARIANE 6 - Tanks and Structures for the New European Launcher, in: Dtsch. Luft- Und Raumfahrtkongress, Munich, Germany, 2017.

[92] ASTM E8 / E8M-16a, ASTM International, West Conshohocken, PA, 2016. doi:10.1520/E0008_E0008M-16A.

[93] J. Osten, B. Milkereit, C. Schick, O. Kessler, Dissolution and Precipitation Behaviour during Continuous Heating of Al–Mg–Si Alloys in a Wide Range of Heating Rates, Materials (Basel). 8 (2015) 2830–2848. doi:10.3390/ma8052830.

[94] ASTM G44-99, ASTM International, West Conshohocken, PA, 2005.

[95] T. Le Jolu, T.F. Morgeneyer, A. Denquin, M. Sennour, A. Laurent, J. Besson, A.-F. Gourgues-Lorenzon, Microstructural Characterization of Internal Welding Defects and Their Effect on the Tensile Behavior of FSW Joints of AA2198 Al-Cu-Li Alloy, Metall. Mater. Trans. A. 45 (2014) 5531–5544. doi:10.1007/s11661-014-2537-1.

[96] D. Trimble, J. Monaghan, G.E. O 'Donnell, J. Jedrzejewski, Force generation during friction stir welding of AA2024-T3, Manuf. Technol. 61 (2012) 9–12. doi:10.1016/j.cirp.2012.03.024.

[97] K.V. Jata, S.L. Semiatin, Continuous dynamic recrystallization during friction stir welding of high strength aluminum alloys, Scr. Mater. 43 (2000) 743–749. doi:10.1016/S1359-6462(00)00480-2.

[98] A. Gerlich, A. Avramovi-Cingara, T.H. North, Stir Zone Microstructure and Strain Rate during Al 7075-T6 Friction Stir Spot Welding, Metall. Mater. Trans. A. 37 (2006) 2006–2773. doi:10.1007/BF02586110.

[99] J. Qian, J. Li, F. Sun, J. Xiong, F. Zhang, X. Lin, An analytical model to optimize rotation speed and travel speed of friction stir welding for defect-free joints, Scr. Mater. 68 (2013) 175–178. doi:10.1016/j.scriptamat.2012.10.008.

[100] Rosenthal, D., The Theory of Moving Sources of Heat and Its Application of Metal Treatments, Trans. ASME. 68 (1946) 849–866.

[101] C. Gao, Z. Zhu, J. Han, H. Li, Correlation of microstructure and mechanical properties in friction stir welded 2198-T8 Al–Li alloy, Mater. Sci. Eng. A. 639 (2015) 489–499. doi:10.1016/j.msea.2015.05.038.

[102] N.E. Prasad, T.R. Ramachandran, Phase Diagrams and Phase Reactions in Al-Li Alloys, in: Aluminum-Lithium Alloy., Elsevier Inc., 2014: pp. 61–97. doi:10.1016/B978-0-12-401698-9.00003-3.

[103] H. Ovri, Micromechanisms governing plastic instability in Al–Li based alloys, Ph.D. thesis, TU Hamburg Harburg, 2015. doi:10.15480/882.1267.

[104] H. Qin, H. Zhang, H. Wu, The evolution of precipitation and microstructure in friction stir welded 2195-T8 Al–Li alloy, Mater. Sci. Eng. A. 626 (2015) 322–329. doi:10.1016/j.msea.2014.12.026.

[105] R.W. Fonda, J.F. Bingert, Precipitation and grain refinement in a 2195 Al friction stir weld, Metall. Mater. Trans. A. 37 (2006) 3593–3604. doi:10.1007/s11661-006-1054-2.

[106] I. Polmear, D. StJohn, J.-F. Nie, M. Qian, Light alloys, Butterworth-Heinemann, 2017. ISBN: 9780080994307.

[107] J.M. Papazian, C. Sigli, J.M. Sanchez, New evidence for GP zones in binary Al-Li alloys, Scr. Metall. 20 (1986) 201–206. doi:10.1016/0036-9748(86)90126-2.

[108] R.A. Herring, F.W. Gayle, J.R. Pickens, High-resolution electron microscopy study of a high-copper variant of weldalite 049 and a high-strength AI-Cu-Ag-Mg-Zr alloy, J. Mater. Sci. 28 (1993) 69–73. doi:10.1007/BF00349035.

[109] W.A. Cassada, G.J. Shiflet, E.A. Starke, The effect of plastic deformation on Al2CuLi (T1) precipitation, Metall. Trans. A. 22 (1991) 299–306. doi:10.1007/BF02656799.

[110] K.S. Ghosh, K. Das, U.K. Chatterjee, Kinetics of Solid-State Reactions in Al-Li-Cu-Mg-Zr Alloys from Calorimetric Studies, Metall. Mater. Trans. A. 38 (2007) 1965–1975. doi:10.1007/s11661-007-9250-2.

[111] M. Reimann, J. Goebel, J.F. dos Santos, Microstructure Evolution and Mechanical Properties of Keyhole Repair Welds in AA 2219-T851 Using Refill Friction Stir Spot Welding, J. Mater. Eng. Perform. 27 (2018) 5220–5226. doi:10.1007/s11665-018-3519-z.

[112] A. Steuwer, M. Dumont, J. Altenkirch, S. Birosca, A. Deschamps, P.B. Prangnell, P.J. Withers, A combined approach to microstructure mapping of an Al–Li AA2199 friction stir weld, Acta Mater. 59 (2011) 3002–3011. doi:10.1016/j.actamat.2011.01.040.

[113] K.S. Prasad, N.E. Prasad, A.A. Gokhale, Microstructure and Precipitate Characteristics of Aluminum - Lithium Alloys, in: Aluminum-Lithium Alloy., Elsevier Inc., 2014: pp. 99–137. doi:10.1016/B978-0-12-401698-9.00004-5.

[114] L. Ou, Z. Zheng, Y. Nie, H. Jian, Hot deformation behavior of 2060 alloy, J. Alloys Compd. 648 (2015) 681–689. doi:10.1016/j.jallcom.2015.07.027.

[115] A.K. Shukla, W.A. Baeslack, Study of microstructural evolution in friction-stir welded thin-sheet Al–Cu–Li alloy using transmission-electron microscopy, Scr. Mater. 56 (2007) 513–516. doi:10.1016/j.scriptamat.2006.11.028.

[116] A.K. Shukla, W.A. Baeslack, Study of process/structure/property relationships in friction stir welded thin sheet Al–Cu–Li alloy, Sci. Technol. Weld. Join. 14 (2009) 376–387. doi:10.1179/136217109X412409.

[117] K. Colligan, Material Flow Behavior during Friction Stir Welding of Aluminum, Weld. J. 78 (1999) 229–237.

[118] M. Cabibbo, H.J. McQueen, E. Evangelista, S. Spigarelli, M. Di Paola, A. Falchero, Microstructure and mechanical property studies of AA6056 friction stir welded plate, Mater. Sci. Eng. A. 460 (2007) 86–94. doi:10.1016/j.msea.2007.01.022.

[119] M. Esmaily, N. Mortazavi, W. Osikowicz, H. Hindsefelt, J.E. Svensson, M. Halvarsson, J. Martin, L.G. Johansson, Bobbin and conventional friction stir welding of thick extruded AA6005-T6 profiles, Mater. Des. 108 (2016) 114–125. doi:10.1016/j.matdes.2016.06.089.

[120] H.J. Mcqueen, S. Spigarelli, M.E. Kassner, E. Evangelista, Hot Deformation and Processing of Aluminum Alloys, CRC Press, 2011. ISBN: 9781138071636.

[121] H. Li, Y. Tang, Z. Zeng, Z. Zheng, F. Zheng, Effect of ageing time on strength and microstructures of an Al–Cu–Li–Zn–Mg–Mn–Zr alloy, Mater. Sci. Eng. A. 498 (2008) 314–320. doi:10.1016/j.msea.2008.08.001.

[122] B. Malard, F. De Geuser, A. Deschamps, Microstructure distribution in an AA2050 T34 friction stir weld and its evolution during post-welding heat treatment, Acta Mater. 101 (2015) 90–100. doi:10.1016/j.actamat.2015.08.068.

[123] P.S. Chen, B.N. Bhat, Time-Temperature-Precipitation Behavior in AI-Li Alloy 2195, Tech. Rep. NASA (2002).

[124] F.D. Geuser, B. Malard, A. Deschamps, Microstructure mapping of a friction stir welded AA2050 Al – Li – Cu in the T8 state, Philos. Mag. 94 (2014) 37–41. doi:10.1080/14786435.2014.887862.

[125] H. Zhang, M. Wang, X. Zhang, G. Yang, Microstructural characteristics and mechanical properties of bobbin tool friction stir welded 2A14-T6 aluminum alloy, Mater. Des. 65 (2014) 559–566. doi:10.1016/j.matdes.2014.09.068.

[126] A.M. Glenn, T.H. Muster, C. Luo, X. Zhou, G.E. Thompson, A. Boag, A.E. Hughes, Corrosion of AA2024-T3 Part III: Propagation, Corros. Sci. 53 (2011) 40–50. doi:10.1016/J.CORSCI.2010.09.035.

[127] J. Victor De Sousa Araujo, U. Donatus, F. Martins Queiroz, M. Terada, M.X. Milagre, M. Cavalieri De Alencar, I. Costa, On the severe localized corrosion susceptibility of the AA2198-T851 alloy, Corros. Sci. 133 (2018) 132–140. doi:10.1016/j.corsci.2018.01.028.

[128] Y. Ma, X. Zhou, W. Huang, Y. Liao, X. Chen, X. Zhang, G.E. Thompson, Crystallographic defects induced localised corrosion in AA2099-T8 aluminium alloy, Corros. Eng. Sci. Technol. 50 (2015) 420–424. doi:10.1179/1743278214Y.0000000237.

[129] M. Guérin, J. Alexis, E. Andrieu, L. Laffont, W. Lefebvre, G. Odemer, C. Blanc, Identification of the metallurgical parameters explaining the corrosion susceptibility in a 2050 aluminium alloy, Corros. Sci. 102 (2016) 291–300. doi:10.1016/j.corsci.2015.10.020.

[130] Y. Ma, X. Zhou, Y. Liao, Y. Yi, H. Wu, Z. Wang, W. Huang, Localised corrosion in AA 2099-T83 aluminium-lithium alloy: The role of grain orientation, Corros. Sci. 107 (2016) 41–48. doi:10.1016/j.corsci.2016.02.018.

[131] U. Donatus, M. Terada, C.R. Ospina, F.M. Queiroz, A. Fatima Santos Bugarin, I. Costa, On the AA2198-T851 alloy microstructure and its correlation with localized corrosion behaviour, Corros. Sci. 131 (2018) 300–309. doi:10.1016/j.corsci.2017.12.001.

[132] R. Grilli, M.A. Baker, J.E. Castle, B. Dunn, J.F. Watts, Localized corrosion of a 2219 aluminium alloy exposed to a 3.5% NaCl solution, Corros. Sci. 52 (2010) 2855–2866. doi:10.1016/J.CORSCI.2010.04.035.

[133] Y. Ma, X. Zhou, G.E. Thompson, T. Hashimoto, P. Thomson, M. Fowles, Distribution of intermetallics in an AA 2099-T8 aluminium alloy extrusion, 126 (2011) 46–53. doi:10.1016/j.matchemphys.2010.12.014.

[134] V. Proton, J. Alexis, E. Andrieu, J. Delfosse, A. Deschamps, F. de Geuser, M.-C. Lafont, C. Blanc, The influence of artificial ageing on the corrosion behaviour of a 2050 aluminium-copper-lithium alloy, Corros. Sci. 80 (2014) 494–502. doi:10.1016/j.corsci.2013.11.060.

[135] C. Luo, S.P. Albu, X. Zhou, Z. Sun, X. Zhang, Z. Tang, G.E. Thompson, Continuous and discontinuous localized corrosion of a 2xxx aluminium–copper–lithium alloy in sodium chloride solution, J. Alloys Compd. 658 (2016) 61–70. doi:10.1016/j.jallcom.2015.10.185.

[136] J.F. Li, C.X. Li, Z.W. Peng, W.J. Chen, Z.Q. Zheng, Corrosion mechanism associated with T1 and T2 precipitates of Al-Cu-Li alloys in NaCl solution, J. Alloys Compd. 460 (2008) 688–693. doi:10.1016/j.jallcom.2007.06.072.

[137] X. Zhang, X. Zhou, T. Hashimoto, J. Lindsay, O. Ciuca, C. Luo, Z. Sun, Z. Tang, The influence of grain structure on the corrosion behaviour of 2A97-T3 Al-Cu-Li alloy, Corros. Sci. 116 (2017) 14–21. doi:10.1016/j.corsci.2016.12.005.

[138] F. Mansfeld, S. Lin, S. Kim, H. Shih, Pitting and Passivation of Al Alloys and Al-Based Metal Matrix Composites, Corrosion. 45 (1989) 615–630. doi:10.1149/1.2086442.

[139] J. Warner-locke, J. Moran, B. Hull, L. Reilly, The Effect of Corrosion Pit Morphology on SCC and Fatigue of 2x99 Alloys Compared to 7xxx Alloys, in: Corros. 2013 NACE Int., Orlando, USA, 2013.

[140] ESA Standard, ECSS-Q-ST-70-37C, Sp. Prod. Assur. Qual. Assur. (2013).

[141] J.B. Lumsden, A.T. Allen, The Stress Corrosion Cracking Behavior of AlLi Alloy 8090, Corrosion. 44 (1988) 527–532. doi:10.5006/1.3583971.

[142] Y. Ma, X. Zhou, W. Huang, G.E. Thompson, X. Zhang, C. Luo, Z. Sun, Localized corrosion in AA2099-T83 aluminum-lithium alloy: The role of intermetallic particles, Mater. Chem. Phys. 161 (2015) 201–210. doi:10.1016/j.matchemphys.2015.05.037.

[143] S. Gourdet, F. Montheillet, A model of continuous dynamic recrystallization, Acta Mater. 51 (2003) 2685–2699. doi:10.1016/S1359-6454(03)00078-8.

[144] Y. Lin, Z. Zheng, Microstructural evolution of 2099 Al-Li alloy during friction stir welding process, Mater. Charact. 123 (2017) 307–314. doi:10.1016/j.matchar.2016.11.045.

[145] C. Bartges, M.H. Tosten, P.R. Howell, E.R. Ryba, A combined single crystal X-ray diffraction and electron diffraction study of the T2 phase in Al-Li-Cu alloys, J. Mater. Sci. 22 (1987) 1663–1669. doi:10.1007/BF01132389.

[146] J.C. Rao, E.J. Payton, C. Somsen, K. Neuking, G. Eggeler, A. Kostka, J.F. Dos Santos, Where Does the Lithium Go? - A Study of the Precipitates in the Stir Zone of a Friction Stir Weld in a Li-containing 2xxx Series Al Alloy, Adv. Eng. Mater. 12 (2010) 298–303. doi:10.1002/adem.200900284.

[147] H. Li, D. Huang, W. Kang, J. Liu, Y. Ou, D. Li, Effect of Different Aging Processes on the Microstructure and Mechanical Properties of a Novel Al-Cu-Li Alloy, J. Mater. Sci. Technol. 32 (2016) 1049–1053. doi:10.1016/j.jmst.2016.01.018.

[148] Y.S. Lee, Microstructures in over-aged Al-Cu-Li-Mg-Ag alloys, J. Mater. Sci. Lett. 17 (1998) 1161–1164.

[149] G. Gottstein, Physikalische Grundlagen der Materialkunde, Springer, Berlin, Heidelberg, 2007. doi:10.1007/978-3-540-71105-6.

[150] S.P. Lynch, Mechanistic and fractographic aspects of stress-corrosion cracking (SCC), Stress Corros. Crack. (2011) 3–89. doi:10.1533/9780857093769.1.3.

[151] S.. Kim, U. Erb, K.. Aust, G. Palumbo, Grain boundary character distribution and intergranular corrosion behavior in high purity aluminum, Scr. Mater. 44 (2001) 835–839. doi:10.1016/S1359-6462(00)00682-5.

[152] T. Shoji, Z. Lu, Q. Peng, Factors affecting stress corrosion cracking and fundamental mechanistic understanding of stainless steels, in: Stress Corros. Crack., Woodhead Publishing Series in Metals and Surface Engineering, 2011: pp. 245–272. doi:10.1533/9780857093769.3.245.

[153] N. Kashaev, M. Horstmann, V. Ventzke, S. Riekehr, N. Huber, Comparative study of mechanical properties using standard and micro-specimens of base materials Inconel 625, Inconel 718 and Ti-6Al-4 v, J. Mater. Res. Technol. 2 (2013) 43–47. doi:10.1016/j.jmrt.2013.03.003.

Appendix A: Microtensile testing of welding zones in AA 2060

Microtensile testing was performed to evaluate to local tensile properties in three different locations which are BM, HAZ and SZ. Three samples of each position were tested in RT at a testing velocity of 0.2 mm/minute whereby the displacement was measured by a laser extensometer. The samples were machined using EDM following the approach proposed in [153]. Surface roughness was measured and related cross-section reduction was considered for the final results.

Table A-1 Microtensile testing in various welding locations

Welding zone	Yield strength	Ultimate tensile strength	Elongation
SZ	301±19 MPa	415±7 MPa	20.1±2.4 %
HAZ	405±4 MPa	466±2 MPa	8.7±0.9 %
BM	480±11 MPa	526±11 MPa	10.4±1.1 %

Results of the testing are given in Figure A-1 and Table A-1. These results were used to load the stress corrosion samples of the individual zones which are discussed in Chapter 7.3. It was observed that the SZ samples performed the weakest which is not consistent to the results of the local hardness measurement presented in Chapter 6.4 where the weakest zone is located within the HAZ. This can be explained by the extraction procedure during the manufacturing of the samples.

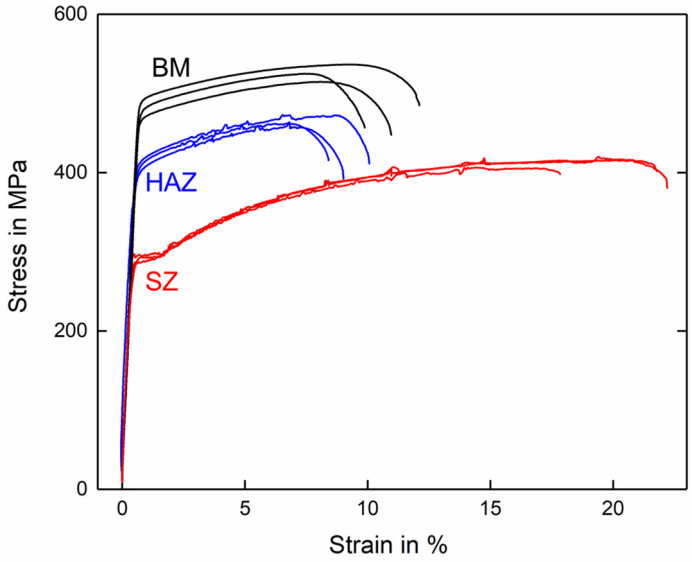

Figure A-1 Stress – strain diagram of the welding zones.

The microtensile sample was positioned at the center line of the corrosion sample and therefore around 10 mm from the center of the weld. According to the findings in presented in Chapter 6.4, this area is stronger than the SZ which can also be observed in Figure A-1. Interestingly, the SZ shows a much higher ductility confirmed by the high elongation at break. Different levels of ductility between the zones will increase local stress concentrations at the transition between the zones which can attribute to a preferred failure location or crack path propagation.

Appendix B: Microtensile testing under elevated temperatures

Microtensile testing was conducted to analyze the BM performance under elevated temperatures. The specimen were EDM machined according to Figure B-1 following the design introduced in [153]. The sample was heated rapidly by induction and the temperature was measured by K-type thermocouples on the samples. Once the target temperature was achieved and constant for 30 seconds, the test was started at a constant testing speed of 0.2 mm/min, the displacement was measured using a laser extensometer. For each temperature level, at least two samples were tested. Prior to testing the surface roughness was measured and subtracted from the resulting cross-section.

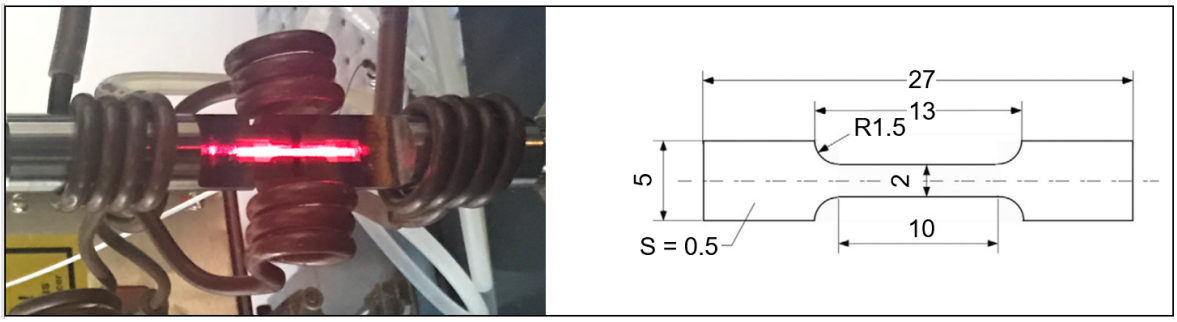

Figure B-1 Tensile testing at elevated temperatures a), sample dimensions b).

Tensile tests under elevated temperatures of both alloys were conducted and are presented in Figure B-2. The results encourage the controversy behavior that was observed in the force measurements during the welding. While AA 2196 is stronger at room temperatures, it also loses its strength much faster with rising temperatures up to about 350 °C where the most significant difference was observed at 200 °C. Note, that irregularities in the testing procedure were detected for samples at 250 °C thus these results should be neglected. Tests were conducted until 450 °C. At higher temperatures, both alloys show a similar strength behavior.

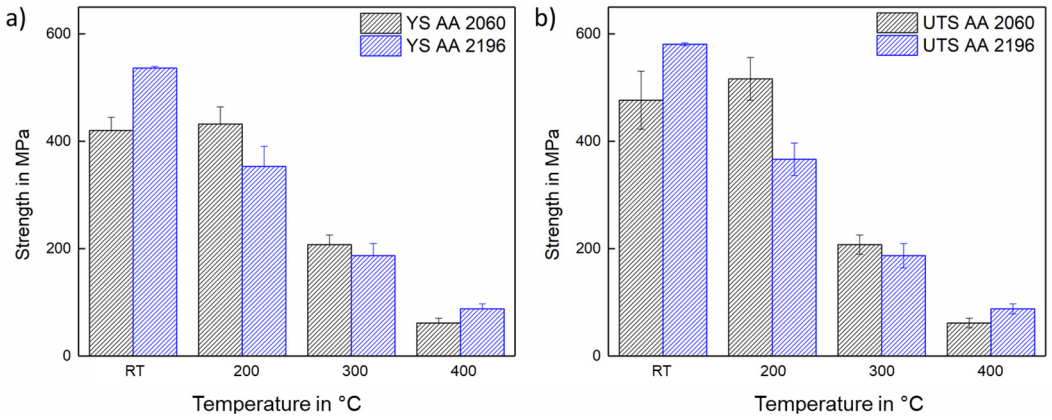

Figure B-2 Tensile testing results under elevated temperatures.

Appendix C: EDS analysis of welding zones

EDS analysis for AA 2060 T8 were conducted as described in Chapter 4.3.5 on samples used for TEM characterization. Samples subjected to EDS analysis were taken from SZ and HAZ material. Coarse grain boundary particles were found and indexed as high copper containing phases with occasionally Mn contribution, compare Figure C-1.

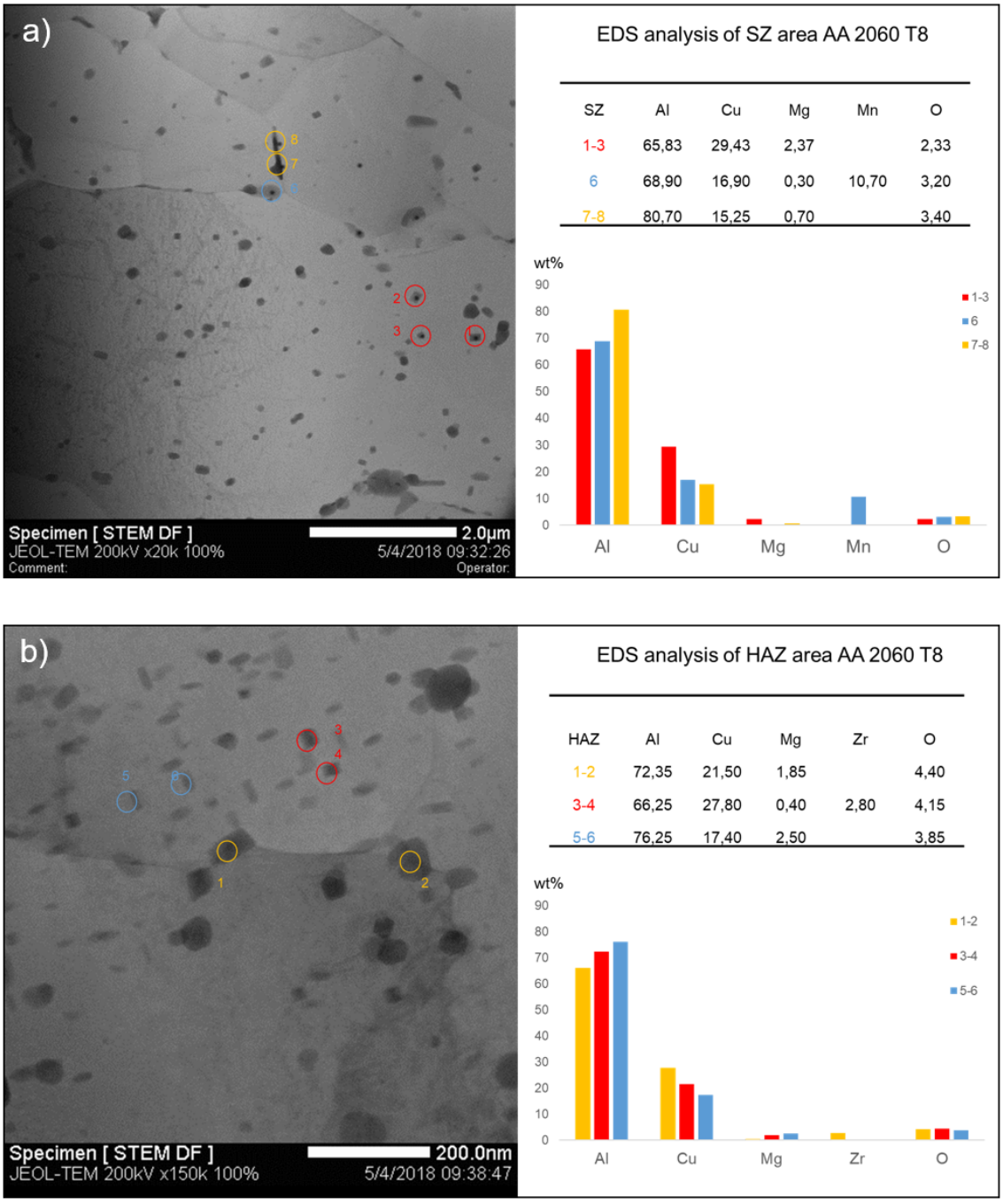

Figure C-1 a) STEM and EDS data SZ AA 2060 T8, b) STEM and EDS data HAZ AA 2060 T8.

Analogue, EDS analysis for AA 2196 T8 were conducted as described in Chapter 4.3.5 on samples used for TEM characterization. Samples subjected to EDS analysis were taken from SZ and HAZ material. Coarse grain boundary particles were found and indexed as high copper containing phases with occasionally Mn contribution, compare Figure C-2.

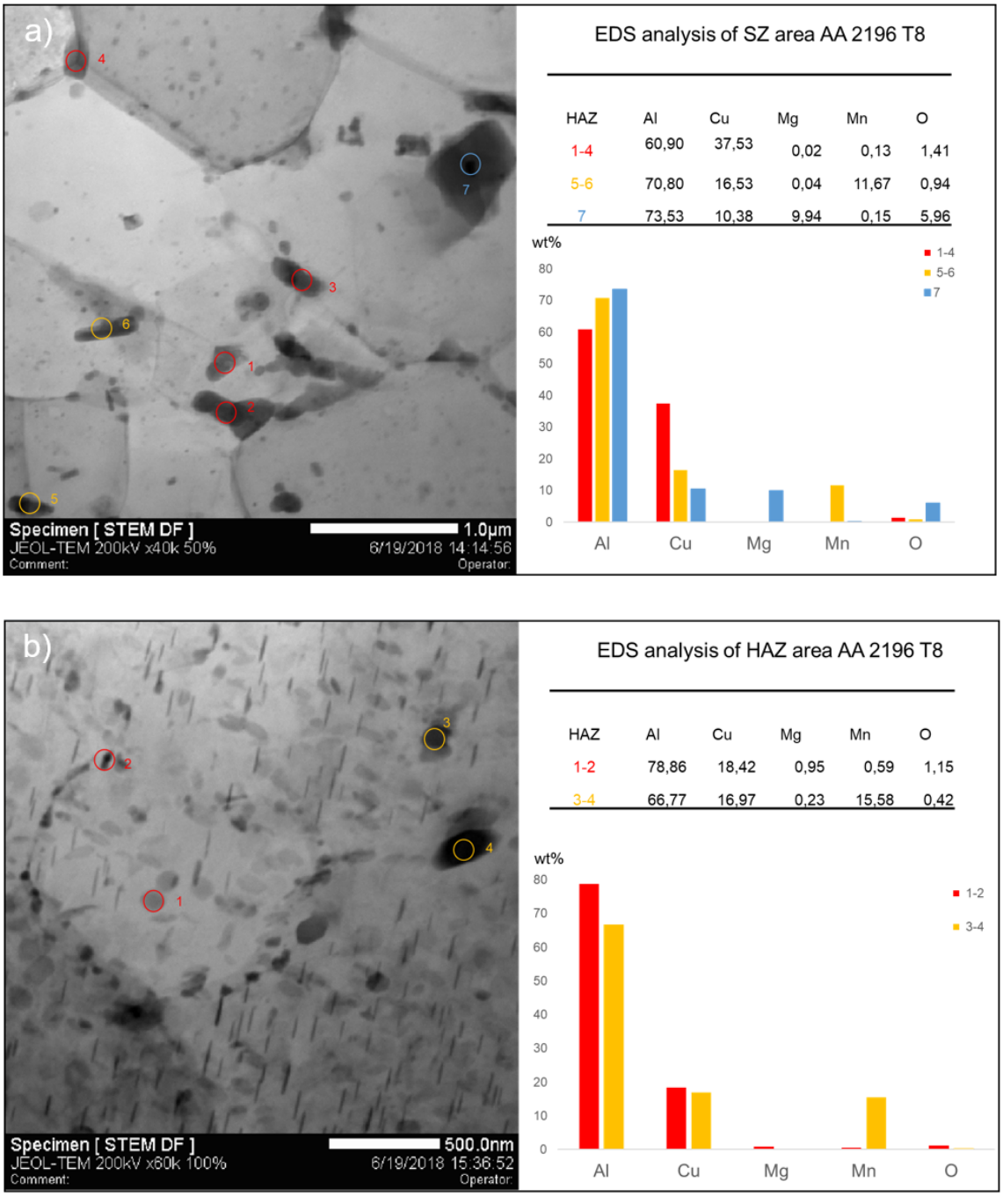

Figure C-2 a) STEM and EDS data SZ AA 2196 T8, b) STEM and EDS data HAZ AA 2196 T8.

Appendix D: Tensile testing results

BM	=	as-received material (T8) samples.
BM SCC	=	as-received material samples, SCC tested.
SSuBT	=	SSuBT welded samples.
SSuBT SCC	=	SSuBT welded samples, SCC tested.
SSuBT SCC unstr.	=	SSuBT welded samples, unloaded exposed to corrosion cycle.

Table D-1 Mechanical properties of tested and untested corrosion samples

ID	Sample count	YS MPa	Ω YS MPa	UTS MPa	Ω UTS MPa	El %	Ω El %
2060 BM	10+	454.35	2.67	512.43	0.65	10.50	0.87
2196 BM	10+	518.20	5.47	562.84	9.15	6.76	NA
2060 BM SCC	2	449.40	2.87	507.90	1.06	7.73	0.23
2196 BM SCC	2	508.14	12.86	546.17	8.88	2.88	0.60
2060 SSuBT	7	282.51	6.48	399.72	12.59	3.81	0.84
2196 SSuBT	3	288.30	11.20	385.30	14.87	2.62	0.40
2060 SSuBT SCC	3	266.45	2.57	328.26	23.60	1.18	0.45
2196 SSuBT SCC	3	267.24	10.67	298.57	19.88	0.72	0.23
2060 SSuBT SCC unstr	3	261.92	1.55	366.58	7.59	3.19	0.33
2196 SSuBT SCC unstr	5	276.25	4.12	343.65	5.36	1.53	0.2

List of Figures

List of Tables